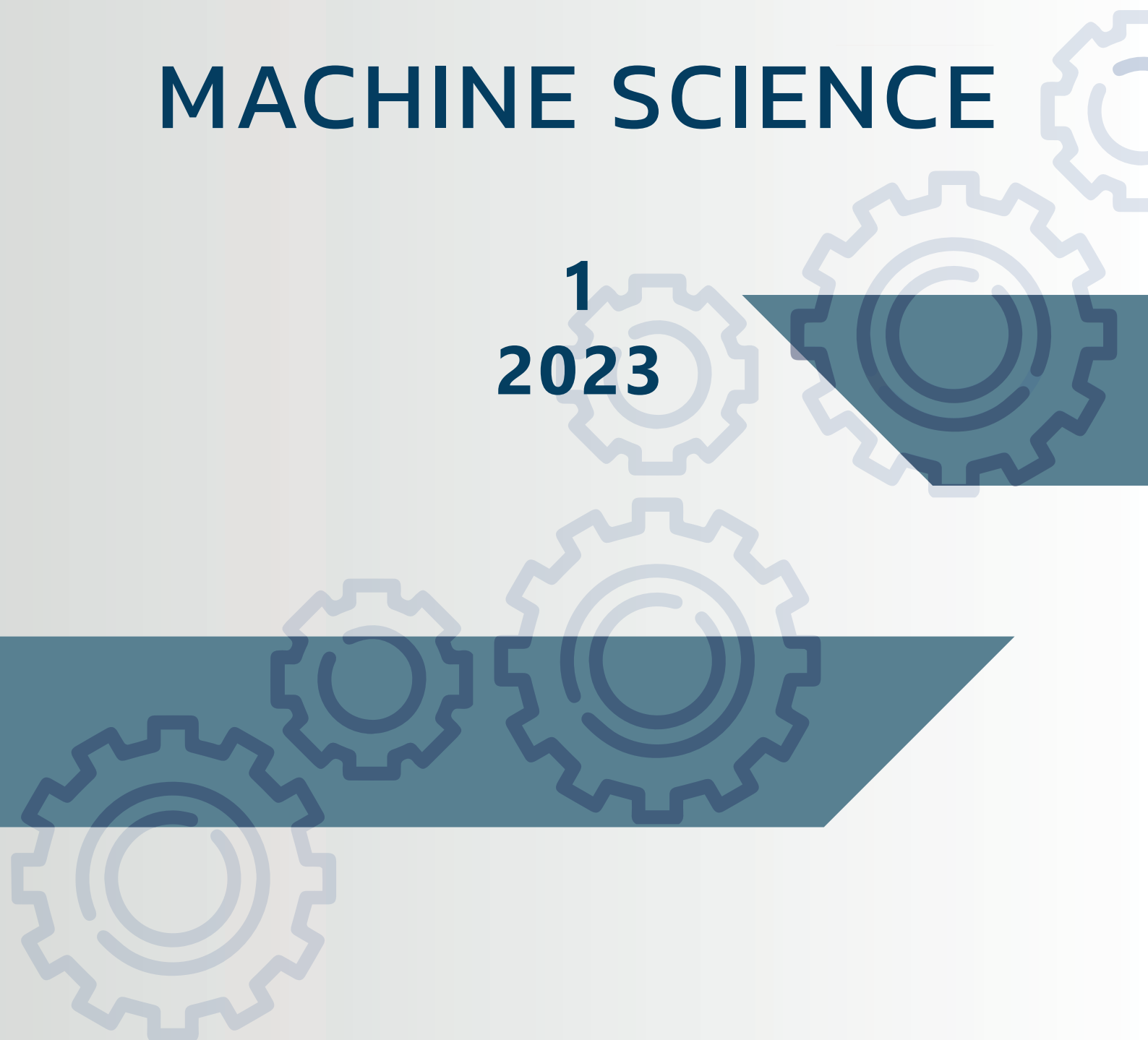


ISSN: 2227-6912
E-ISSN: 2790-0479

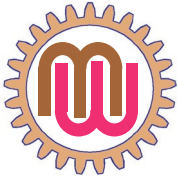
Azerbaijan Technical University

MACHINE SCIENCE



1
2023

International scientific-technical journal



MACHINE SCIENCE

MAŞINŞÜNASLIQ

МАШИНОВЕДЕНИЕ

International scientific-technical journal
Beynəlxalq elmi-texniki jurnal
Международный научно-технический журнал

Number 1 2023

Founder: The Ministry of Education of Azerbaijan Republic
Təsisçi: Azərbaycan Respublikası Təhsil Nazirliyi
Учредитель: Министерство образования Азербайджанской Республики

The journal is included into the list confirmed by Higher Attestation Commission of the Azerbaijan Republic of editions for the publication of works of competitors for scientific degrees

Jurnal Azərbaycan Respublikası Ali Atestasiya Komissiyasının təsdiq etdiyi elmi dərəcə iddiaçılarının əsərlərinin çap edildiyi dövrü elmi nəşrlərin siyahısına daxil edilmişdir.

Журнал входит в перечень, утвержденных ВАК Азербайджанской Республики, изданий для публикации трудов соискателей ученых степеней

Journal was founded according the order No1861 Ministry of Education of Azerbaijan Republic on the date 25.11.2011. Registration No 3521. Journal is published at least twice a year.

Jurnal Azərbaycan Respublikası Təhsil Nazirliyinin 25.11.2011-ci il tarixli 1861 sayılı əmri əsasında təsis edilmişdir. Qeydiyyat № 3521. İldə ən azı iki nömrə nəşr edilir.

Учреждено приказом за №1861 от 25.11.2011 года Министерства образования Азербайджанской Республики. Регистрация № 3521. Ежегодно публикуется два номера.

It has been published since 2001. Published in 2001 - 2011 with a name "Mechanics-machine building" 2001-ci ildən nəşr edilir. 2001 – 2011-ci illərdə "Mexanika-maşınqayırma" adı ilə çap edilmişdir. Издаётся с 2001 года. В 2001 – 2011 годах издано под названием «Механика-машиностроение»

The journal has been included in international citation and indexation system INSPEC since 2011.
Jurnal 2011-ci ildən INSPEC beynəlxalq xülasələndirmə və indeksləndirmə sisteminə daxil edilmişdir.
Журнал включен в международную систему цитируемости и индексации INSPEC с 2011 года

The "MACHINE SCIENCE" journal is supported by Azerbaijan Technical University, which means there are no publication fees for authors.

"MAŞINŞÜNASLIQ" jurnalı Azərbaycan Texniki universiteti tərəfindən dəstəklənir və məqalələrin nəşri üçün müəlliflərdən hər hansı ödəniş tələb olunmur.

Журнал «МАШИНОВЕДЕНИЕ» поддерживается Азербайджанским Техническим Университетом, что означает, что с авторов не взимается плата за публикацию статей.

Editorial address:	Baku, AZ1073, H.Javid ave., 25. AzTU	© Machine Science, 2023 ISSN: 2227-6912 E-ISSN: 2790-0479
Redaksiyanın ünvanı:	Tel: (+994 12) 539 12 25	
Адрес редакции:	E-mail: msj@aztu.edu.az	

EDITORIAL COMMITTEE

Honorary Editor:

Schnack, Eckart (Karlsruhe, Germany)

Editors- in-Chief

Khalilov, Isa (Baku, Azerbaijan)

Editorial Board

Albers, Albert (Karlsruhe, Germany)
Alifov, Alishir (Moscow, Russia)
Alizade, Rasim (Baku, Azerbaijan)
Ardashev, Dmitrii (Chelyabinsk, Russia)
AVEY (Sofiyev), Abdullah (Isparta, Turkey)
Duc, Nguyen Dinh (Hanoi, Vietnam)
Dyakonov, Alexander (Almetyevsk, Russia)
Glazunov, Viktor (Moscow, Russia)
Keller, Andrey (Moscow, Russia)
Larin, Vladimir (Kiev, Ukraine)
Movlazadeh, Vagif (Baku, Azerbaijan)
Omurtag, Mehmet Hakkı (Istanbul, Turkey)
Roth, Bernard (Stanford, USA)
Shariyat, Mohammad (Tehran, Iran)
Shen, Hui-Shen (Shanghai, China)
Stahl, Karsten (Munich, Germany)
Yusubov, Nizami (Baku, Azerbaijan)

Executive Editor:

Ahmedov, Beyali (Baku, Azerbaijan)

Editorial Assistants:

Hajiyev, Anar (Baku, Azerbaijan)
Rahimova, Ilaha (Baku, Azerbaijan)

Contents	3
Burak AKYOL, Mustafa GÜDEN, Alper TAŞDEMİRCİ, Subhan NAMAZOV. Experimental investigation of the effect of strain rate on the crushing strength of a cellular concrete	4-21
Nizami YUSUBOV, Heyran ABBASOVA. Model of machining process control on multi-tool single-carriage adjustments	22-27
Subhan NAMAZOV, Taleh TAGHIYEV, Shahin MASHAYEV. Investigation of wear-resistant materials working under shock-abrasive wear conditions and test conditions	28-35
Viktor GUZEEV, Igor DERYABIN, Dmitrii ARDASHEV. Mathematical models of cutting forces in turning operations	36-45
Victor ARTEMYEV, Sergey MOKRUSHIN, Sergey SAVOSTIN, Vitaly PANKOV. Processing of time signals in a discrete time domain	46-54
Nizami YUSUBOV, Heyran ABBASOVA, Ramil DADASHOV. Theoretical basis for the development of an algorithmic unified complex of mathematical models of cutting forces	55-60
Ahmad IMANOV. Kinematic calculation of variable curvature fist mechanism with convex profile	61-67
Victor ARTEMYEV, Vitaly PANKOV, Victor YAROSHEVICH. Investigation of optimal control of variable systems in the dynamic spectrum	68-75
Allahverdi ALAKBAROV. Structural synthesis of serial spherical manipulators	76-80
Husnu KARIMOV. Research of the interaction impact features of the cotton wicks while hitting the grates in the cotton ginning machines	81-86
Ilham HUSEYNOV. Analysis of traction transmission of railway vehicles and their dynamic characteristics	87-98
SUBMISSION GUIDELINES	99



EXPERIMENTAL INVESTIGATION OF THE EFFECT OF STRAIN RATE ON THE CRUSHING STRENGTH OF A CELLULAR CONCRETE

Burak AKYOL¹, Mustafa GÜDEN^{2*}, Alper TAŞDEMİRÇİ³,
Subhan NAMAZOV⁴

^{1,2*,3}Dynamic Testing and Modeling Laboratory and Department of Mechanical Engineering, Izmir Institute of Technology, Izmir, Turkey

⁴Vice-rector for science and innovation of Azerbaijan Technical University, Baku, Azerbaijan

E-mail: burakakyol@iyte.edu.tr¹, mustafaguden@iyte.edu.tr^{2*}, alpertasdemirci@iyte.edu.tr³,
subhan_namazov@daad-alumni.de⁴

Abstract: The strain rate dependent compressive strength of an autoclaved aerated concrete (AAC) having a density of 600 kg m^{-3} was experimentally investigated between quasi-static and high strain rates (2×10^{-3} – 4150 s^{-1}) through quasi-static and dynamic compression, confined compression and indentation tests. High strain rate equilibrium and direct impact non-equilibrium compression tests in conjunction with the high strain rate confined compression and indentation tests were conducted in a compression Split Hopkinson Pressure Bar. The experimental results showed two different regions of the compressive strength-dependency on the strain rate: a low-strain rate-dependent region from quasi-static to $\sim 18 \text{ s}^{-1}$ and a high-strain rate-dependent region from $\sim 18 \text{ s}^{-1}$ to $\sim 1000 \text{ s}^{-1}$. The switch of the failure mode from the single axial cracking at quasi-static strain rates to the extensive axial and circumferential cracking at increasing strain rates was ascribed to both the axial and radial inertia. The dynamic increased factor (DIF=dynamic strength/static strength) showed an abrupt increase after $\sim 18 \text{ s}^{-1}$ as similar with the compressive strength. The mean confined and indentation strength values also increased as the velocity increased, while the mean confined compression strength values were shown to be comparable with the dynamic compressive strength values. The inertia and strain rate contributions to the enhancement of DIF until about 1000 s^{-1} were predicted by taking the quasi-static indentation strength as the full confinement strength.

Keywords: Autoclaved aerated concrete; Split Hopkinson Pressure Bar; direct impact; compressive strength; indentation; confinement; inertia

Introduction. Autoclaved aerated concrete (AAC) is a light-weight cellular material with relatively high compressive strength, low thermal conductivity, high sound absorptivity, non-flammability and high durability [1]. AAC is processed by foaming a ceramic slurry of sand, lime, cement and water in the presence of a foaming agent i.e. aluminum powder and has become one of the most widely used building materials [2]. It is applied mainly as the heat and sound insulation material and also as the structural element. Most of the previous studies on the determination of the mechanical properties of AAC have been so far at quasi-static strain rates; examples can be found in [1, 3-8]. However, the dynamic loading of the AAC-based structures is quite possible under extreme loading conditions such as earthquakes, explosions and projectile impacts. But, there have been few experimental and numerical studies, based on the authors' knowledge, on the dynamic loading behavior of AAC in the literature as will be shortly reviewed here. The shock stress response of an AAC (500 kg m^{-3}) was previously investigated [9]. Radial and spalling cracks were detected and the source-distance was shown the main factor affecting the number of cracks formed. The quasi-static and dynamic compression mechanical behavior of an AAC sample (550 kg m^{-3}) were determined until about 104 s^{-1} [10]. In the confined compression tests, the samples were completely densified with a continuous load-displacement behavior. The dynamic compressive strength increased by 45% of the quasi-static strength at 515 s^{-1} and the damage formed earlier in dynamically tested samples. Dry and water-saturated AAC samples were tested between 1.4×10^2 and $1 \times 10^3 \text{ s}^{-1}$ [11]. The failure

strength showed a positive strain rate sensitivity from quasi-static up to a critical strain rate; thereafter, the samples were pulverized near the plane of impact.

The strength enhancement in brittle rock-like materials is generally presented by the dynamic increase factor (DIF=dynamic fracture strength/static fracture strength). The DIF of concrete was reported to vary between 1 and 2.5 from static to dynamic strain rates with a sudden increase after about 100 s^{-1} [12]. The compressive strength of limestone was shown to increase slowly with strain rate up to 10^3 s^{-1} ; thereafter, increased sharply, approaching the shock fracture strength [13]. An “s-type” dependence of the fracture strength of brittle materials on strain rate was proposed as schematically shown in Figure 1 [14].

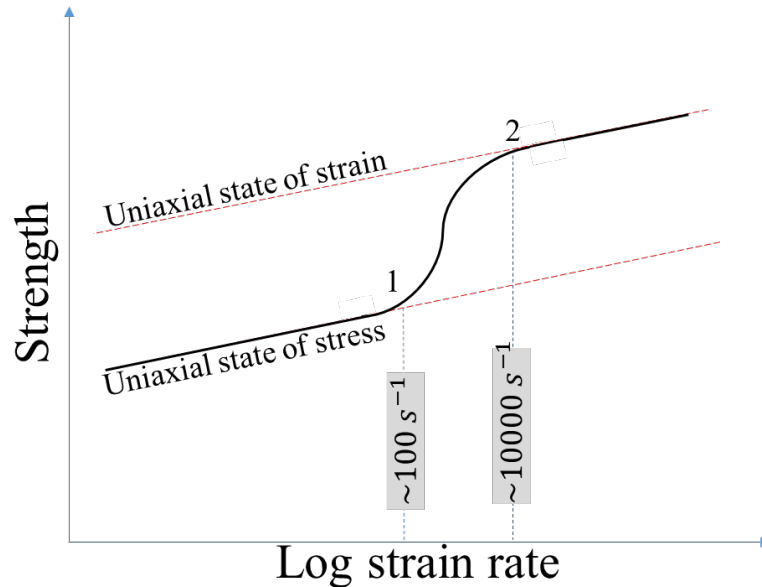


Figure 1. The schematic of the variation of the strength of brittle materials with strain rate, adapted from reference [14]

On this “s-type” curve, there are two turning points: (1) from a low-strain rate-dependent strength to a high-strain rate-dependent strength region and (2) from a high-strain rate-dependent strength to again a low-strain rate-dependent strength region. The first and second turning points were broadly proposed as 10^2 and 10^4 s^{-1} for concrete, respectively [15]. The low-strain rate-dependent strength region was ascribed to the strain-rate dependent growth of tensile micro cracks (thermally activated mechanism) and viscous behavior of bulk material between cracks (Stefan effect) [16-18]. Since the energy needed for crack opening is much higher than the energy needed for crack growth at quasi-static strain rates, few cracks grow under static loading through the weakest path along axial direction. There is however less time for both crack opening and growth at increasing strain rates, causing an increase in the dynamic strength and number of micro cracks formed. [17-19]. The water content increased the strain rate sensitivity of concrete under tension [20] and compression [21] and altered the compression failure mode [21]. The increased strain rate sensitivity of wet concrete was ascribed to viscous mechanism in several references [21-23]. At increasing strain rates, an elastically deforming structure cannot expand in the transverse direction (Poisson’s expansion) due to the radial inertia restraint. The radial inertia imposes a confinement stress on the deforming structure, transforming the deformation from a uniaxial state of stress to a uniaxial state of strain. The increase in the strength of concrete after a critical velocity was ascribed to the development of a uniaxial state of strain [13, 24-27]. Modelling SHPB tests on concrete using a pressure dependent strength model showed that the stress triaxiality was near 1D state of stress at 47 s^{-1} , while it reached 1D state of strain at $\sim 795 \text{ s}^{-1}$ [28]. Above this critical strain rate, the sample deformation was completely 1D state of strain. The explained pseudo strain rate effect occurs when the compressive strength of the tested sample is hydrostatic pressure sensitive and lateral confinement is developed

on the sample. A current concrete model has adapted a cut-off value of 2.94 to cap DIF above 300s^{-1} [28]. But, it is not clear whether or not this capping occurs in or after the high-strain rate-dependent strength region. The inertia corrected stress of a cylindrical sample under compression was given by Davies and Hunter in 1963 [29]

$$\sigma_c = \sigma_A + \left[\left(\frac{h^2}{3} \right) + \nu^2 \left(\frac{d^2}{8} \right) \right] \rho \ddot{\epsilon}(t) \quad (1)$$

where σ_A is the average stress, h and d are sequentially the height and diameter of a cylindrical sample and ρ and ν are the density and Poisson's ratio of the test material, respectively. The second and third terms in Eqn. 1 are the axial and radial inertia stress term, respectively. As noted in the above equation, confining the sample during deformation eliminates the stress rise due to radial inertia.

The main motivation for the present study is the lack of a comprehensive experimental study on the strain rate dependent compressive strength of AAC as stated earlier. Therefore, the strain rate sensitive compressive strength of an AAC was investigated experimentally in order to determine the effect of strain rate on the crushing behavior. Various test methods including quasi-static and dynamic compression, drop-weight compression and direct impact tests were applied. The quasi-static compression tests were performed at the velocities between 5×10^{-5} to 5×10^{-3} m s^{-1} , corresponding to the strain rates of 2×10^{-3} and 2×10^{-1} s^{-1} . The low-velocity impact tests were performed in a drop-weight set-up at a velocity of ~ 1 m s^{-1} , corresponding to ~ 35 s^{-1} . The dynamic compression tests were performed in a compression type Split Hopkinson Pressure Bar (SHPB) at the velocity of 8 m s^{-1} , corresponding to ~ 185 s^{-1} and the direct impact tests between 10 and 108 m s^{-1} , corresponding to ~ 385 and ~ 4150 s^{-1} . The direct impact tests were non-equilibrium tests and analyzed differently from the compression SHPB tests.

Materials and testing

Sample preparation

AAC blocks and plates (600 kg m^{-3}) were provided by one of the biggest AAC producers in Turkey, AKG Gaz Beton. The quasi-static and dynamic compression test samples, ~ 19.4 mm in diameter and 26 mm in length, were cored-drilled from 26 mm-thick AAC plates using a core-drilling machine. Figures 2(a-c) show the pictures of a 26 mm-thick core-drilled AAC plate, fracture surface of an AAC sample and the core-drilled compression test samples, respectively. As seen in Figure 2(b), the tested AAC had a typical cellular structure, composing of cells and cell walls and edges. The cell sizes were measured using an image analyzer on the pictures of the fracture surfaces of few samples. At least 120 cells were counted and the results were averaged. The average cell size was determined 0.5 mm using above method. No coolant was used in the core-drilling and the surfaces of cylindrical compression test samples were cleaned after drilling by applying pressurized air. The indentation tests were directly performed on the flat surfaces of AAC blocks. Before testing, the core-drilled compression test samples and the blocks for the indentation tests were kept in an oven at 70°C for 24 h (standard procedure).

The same sample sizes were used in the quasi-static, SHPB and direct impact compression tests. The maximum diameter of test samples was limited by the diameter of the bars of the used SHPB (19.45 mm). The sample size can affect the critical strain rate for the inertia dominated deformation. It may also alter the strength since the strength of brittle materials is volume dependent (the probability of the presence of larger microstructural defects). Larger samples exhibit lower strength. On the other hand, smaller samples may not represent the homogeneous mechanical properties, which requires at least 8-10 cells in one dimension [30, 31]. The tested samples in the present study contained much more cells (0.5 mm cell size) than the critical number cells.

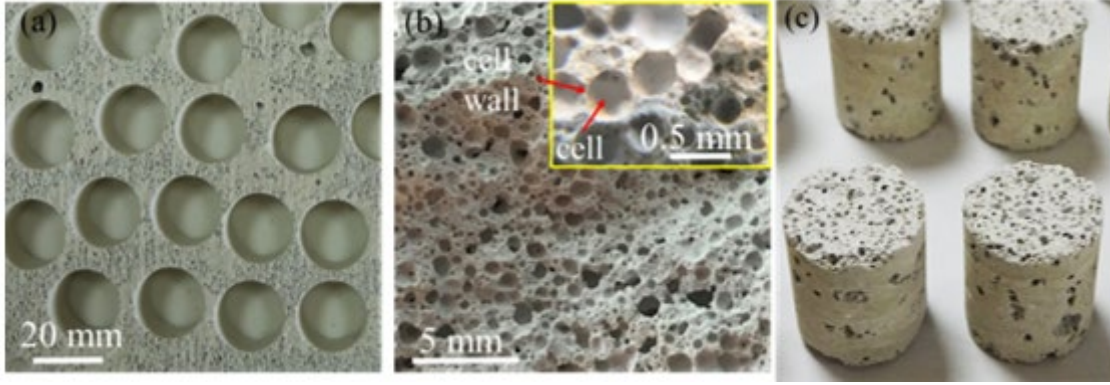


Figure 2. The pictures of (a) a core-drilled 26 mm-thick plate, (b) the fracture surface of a AAC sample (showing the typical foam cellular structure) and (c) the compression test samples after core-drilling

Unconfined quasi-static and high strain rate compression tests

Quasi-static compression tests were performed in a Shimadzu AG-X Universal Test machine in accord with ASTM C39/C 39M-03 “Standard Test Method for Compressive Strength of Cylindrical Concrete Specimens” [32]. Three different cross-head speeds were used in the quasi-static compression tests; 5×10^{-5} , 5×10^{-4} , and 5×10^{-3} m s⁻¹, corresponding to the strain rates of $\sim 2 \times 10^{-3}$, $\sim 2 \times 10^{-2}$ and $\sim 2 \times 10^{-1}$ s⁻¹, respectively. The strain was calculated as the nominal strain (elongation divided by initial length) and determined both from the machine stroke and the video extensometer synchronized to the test machine. In all compression tests, an axis-aligned pin-ball upper compression test platen was used and the sample deformation was recorded by using a video camera.

The low velocity compression tests were performed in a FRACTOVIS drop-weight tester using a 90 kN-90 mm-diameter flat-end striker. A photocell-circuit was used to measure the striker velocity at 1000 kHz. The initial striker velocity was varied between 1.05 and 1.1 m s⁻¹, corresponding to a strain rate between 34 and 38 s⁻¹. The striker velocity decreased only ~ 0.1 m s⁻¹ until the fracture. The energy absorbed by the AAC samples was calculated ~ 0.4 J by taking the fracture strength 7.34 MPa and the fracture strain 0.015. The striker energy was therefore far greater than the energy absorbed by the sample by taking into account an applied weight of 6.42 kg and the mass of the striker itself. The deformation was further recorded by a Fastcam Photron high speed camera at 20000 fps.

The SHPB apparatus used in the high strain rate tests consisted of 19.45 mm diameter Inconel 718 incident (3110 mm), transmitter (2050 mm) and striker (500 mm) bar. The elastic modulus and density of bars were 204 GPa and 8394 kg m⁻³, respectively. The schematic of the used SHPB test system is shown in Figure 3(a). The strains on the bars were measured by a full Wheatstone-bridge configuration of 350 Ω foil strain gauges. The velocity of the striker bar was measured using laser-velocity gates mounted at the exit of the gas barrel and also from the Fastcam Photron high speed camera records of the striker bar. Based on the stress equilibrium, the strain (ϵ_s), stress (σ_s) and strain rate ($\dot{\epsilon}_s$) of the sample are [33]

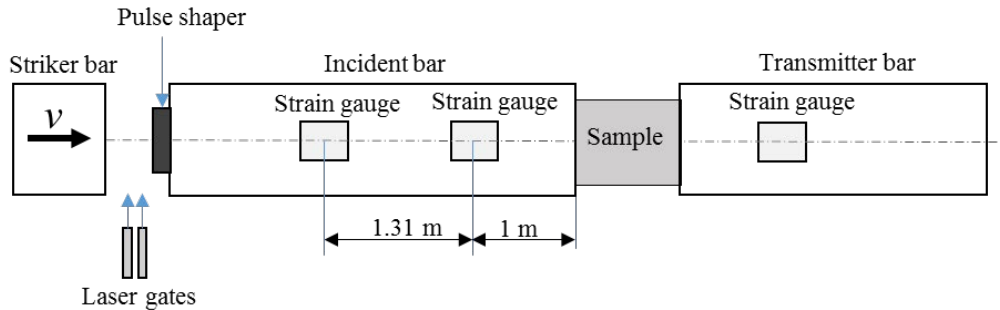
$$\epsilon_s(t) = -\frac{2c_b}{L_s} \int_0^t \epsilon_R(t) dt \quad (3)$$

$$\sigma_s(t) = \frac{A_b}{A_s} E_b \epsilon_T(t) \quad (4)$$

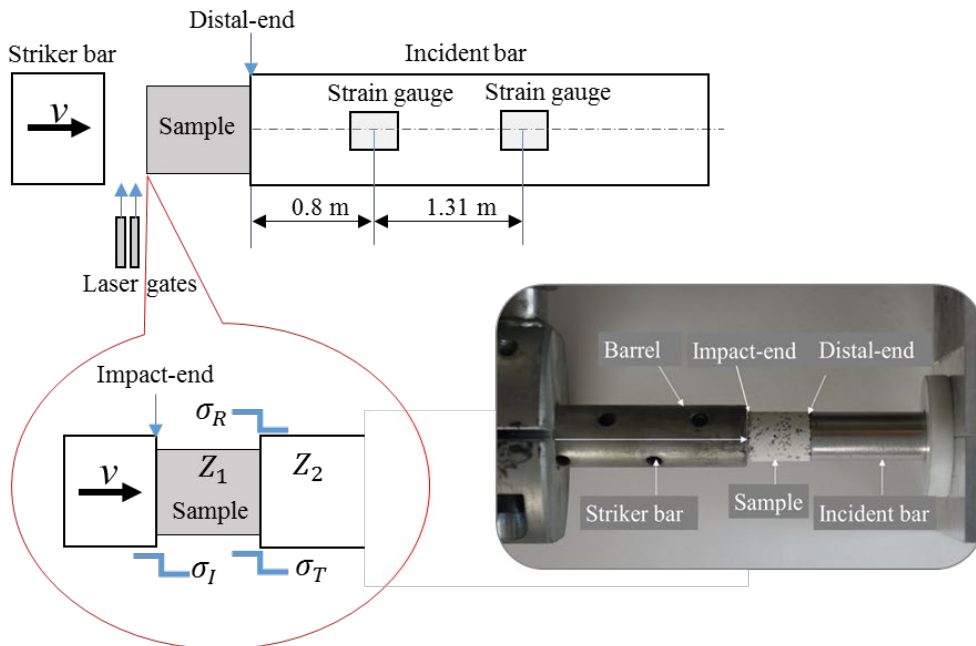
$$\dot{\epsilon}_s(t) = -\frac{2c_b}{L_s} \dot{\epsilon}_R(t) \quad (5)$$

where L_s , A_b , A_s , E_b , c_b and t are the length of sample, the cross-sectional area of bar and sample, elastic modulus and wave velocity of bar, and time, respectively. ϵ_R and ϵ_T are sequentially the reflected and transmitted strains.

Eqns. 3 through 5 are valid when the stress at the sample/incident bar interface is equal to the stress at the sample/transmitter bar interface [29, 33]. It was analytically shown by Davies and Hunter [29] that the stress equilibrium in SHPB is established when $T \geq \pi t_s$; where T is the duration of loading, t_s is the sample transit time (L_s / c_s) and c_s is the wave velocity of sample [29]. In other words, the incipient stress wave should reverberate at least 3-4 times in the sample before the equilibrium is established [34]. In the SHPB testing of brittle materials, test sample may fracture within the initially steeply-rising part of incident stress wave at a time earlier than the time needed to establish the stress equilibrium (time to fracture $> \pi t_s$). In order to induce a gradually-rising incident wave, pulse shaping method is widely used [12]. In this method, a thin layer of a ductile metal is placed at the front of the incident bar so that the deformation of the thin-metal layer in between the striker and incident bar induces a gradually-rising stress wave on the incident bar. In the present study, an aluminum sheet in 10x10x2 mm size was used as a pulse shaper and placed at the front of the incident bar by applying a thin layer of lubricant. The tests satisfying the stress equilibrium in the SHPB are called “equilibrium tests” in the present study.



(a)



(b)

Figure 3. The schematic of (a) the SHPB compression test and (b) direct impact test together with the picture of the direct impact test

In the direct impact tests, the striker bar directly impinged on the test sample placed at the front of the incident bar with an initial velocity (v) as shown in Figure 3(b). The direct impact tests were performed at 10 m s^{-1} using a 500 mm-long Inconel striker bar and at 30 and 108 m s^{-1} using a 200 mm-long 1100 Al alloy striker bar. Higher velocities were attained using the lighter Al striker bar. In these tests, the distal-end stress (σ_D) shown in Figure 3(b) was calculated using the following relation

$$\sigma_D(t) = \frac{A_b E_b \varepsilon_i}{A_s} \quad (6)$$

where ε_i is the strain measured on the incident bar. Unlike the classical compression SHPB test, the distal-end stress is not equal to the impact-end stress in the direct impact test. Therefore, these are “non-equilibrium” tests. The calculation of the upper velocity for the stress equilibrium in the classical compression SHPB test is as follows. The strain in a long elastic bar is $\frac{v}{c}$; where v is the particle velocity and c is the elastic wave velocity. The quasi-static fracture strain (ε_f) of the tested AAC samples were determined around 0.02 and the elastic modulus $\sim 0.3 \text{ GPa}$.

By taking the density of ACC sample 600 kg m^{-3} , a particle velocity of $\sim 15 \text{ m s}^{-1}$ ($v = \varepsilon_f c$) was calculated at the fracture strain. Division this number by π gives an upper limit for the SHPB equilibrium test, $\sim 5 \text{ m s}^{-1}$. Above calculations should be taken as a rough estimate of the upper velocity limit as the fracture strain and elastic modulus of the tested sample may change with strain rate and the use of pulse shaper reduces the particle velocity of incident bar below that of striker bar. The lowest velocity used in the direct impact tests (10 m s^{-1}) is hence two times the calculated velocity for the stress equilibrium; therefore, the direct impact tests are considered as “non-equilibrium tests”. Note also that the impact-end stress could not be measured in the direct impact tests, while the strain was calculated indirectly by assuming a constant deformation velocity. For a constant deformation velocity, the sample should absorb only small portion of the kinetic energy of striker. The energy absorption of an AAC sample until fracture strain (~ 0.02) was calculated $\sim 0.9 \text{ J}$, while the energy of striker bar at 10, 30 and 108 m s^{-1} were ~ 61.6 , ~ 71.79 and $\sim 930 \text{ J}$, respectively. These calculations indicated that the maximum sample energy absorption was $\sim 1.5\%$ of that of the striker bar (10 m s^{-1}), confirming the constant deformation velocity assumption. The strain rates of non-equilibrium tests were calculated, based on the constant striker bar velocity, sequentially as ~ 385 , ~ 1150 and $\sim 4150 \text{ s}^{-1}$ for the tests at 10, 30 and 108 m s^{-1} .

In both classical SHPB compression and direct impact tests, the bar strains were measured some distance away from the sample/bar interfaces and were implemented in Eqns. 3 through 5 by assuming no wave-dispersion on the bars. In the used SHPB test apparatus, the strain gauges were 0.8 and 1 m away from the sample/bar interfaces for the direct impact and classical SHPB tests, respectively (Figures 3(a) and (b)). In order to account wave dispersion, two strain gauges (1.31 m apart) were mounted on the incident bar as seen in Figures 3(a) and (b). The strain readings from these two gauges were then used to check the wave-dispersion on the bars.

The impact of striker bar creates a compressive incident wave (σ_I) at the impact-end of the AAC sample as shown in Figure 3(b). This wave is reflected (σ_R) and transmitted (σ_T) at the distal end of the sample due to the mechanical impedance ($A\rho c$, where A is the cross-sectional area and ρ is the density) difference between AAC sample and incident bar (Figure 3(b)). The ratio of the impedances of ACC sample/bar was calculated 90.2. The magnitudes of the reflected and transmitted waves from the distal-end are sequentially as

$$\sigma_R = \left(\frac{Z_2 - Z_1}{Z_1 + Z_2} \right) \sigma_1 \approx 0.02 \sigma_1 \quad (7)$$

$$\sigma_T = \left(\frac{2Z_2}{Z_1 + Z_2} \right) \left(\frac{A_1}{A_2} \right) \sigma_1 \approx 0.98\sigma_1 \quad (8)$$

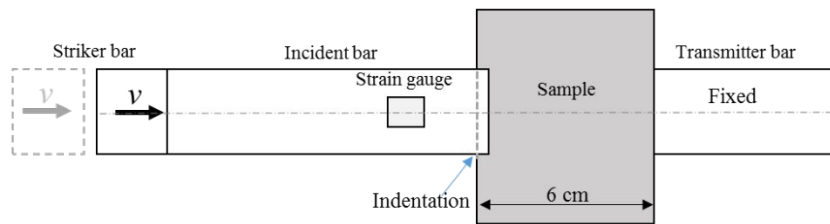
where Z_1 and Z_2 are the mechanical impedance of AAC sample and bar and A_1 and A_2 are the areas of AAC sample and bar, respectively. In the direct impact tests ($\geq 10 \text{ m s}^{-1}$), the wave created on AAC sample upon the impact of striker bar was transmitted to the incident bar by 98%. The wave was therefore assumed to be transmitted to the incident bar completely and the strain-gauge measured stresses on the incident bar nearly corresponded to the distal-end stress of ACC sample.

Quasi-static and high strain rate indentation and confined compression tests

The quasi-static indentation tests were conducted on 40x40x20 cm blocks using flat-ended 5, 10, 15, 20, 25 and 30 mm-diameter 304 steel indenters (Figure 4(a)) until about 25 mm depth of indentation at three different velocities, 5×10^{-5} , 5×10^{-4} , and $5 \times 10^{-3} \text{ m s}^{-1}$. The indenters were screwed to the Shimadzu Universal Testing Machine at the treated end, while 20 mm indenter was directly compressed on the blocks by the upper compression platen. The tested blocks were then cut into half at the mid-section of the indentation in order to observe the powder accumulation in the front of the indenter. The high strain rate indentation tests (10 m s^{-1}) were performed using a modified SHPB test. In these tests, AAC sample (6x6x6 cm) was inserted between the incident and transmitter bar (Figure 4(b)). The transmitter bar was tightened on its supports in such a way that during a test it did not move and the incident bar (19.4 mm in diameter) indented the sample. The difference between incident and reflected stresses gave the indentation dynamic strength of the tested sample.



(a)



(b)

Figure 4. The pictures of 5, 10, 15, 20, 25 and 30 mm indenters from left to right (a) and the schematic of dynamic indentation test (b)

A steel tube with an inner diameter of 19.35 mm, slightly smaller in diameter than the compression test sample, was used to perform the confined compression tests at quasi-static and high strain rates. The quasi-static tests were performed at $5 \times 10^{-4} \text{ m s}^{-1}$ and the dynamic tests at 8 m s^{-1} without using a pulse shaper. Before testing, the samples were inserted inside the steel tube with a wall thickness of 2 mm by applying a pressure. The schematics of the static and dynamic confined

compression tests are shown in Figures 5(a) and (b), respectively. In the quasi-static tests, the sample was compressed by a 100 mm-long Inconel bar which was just located under the loading plate. In dynamic tests, AAC sample was placed between the flat-ends of the incident and transmitted bar inside the confinement steel tube. Since the strength of the steel tube was much higher than that of AAC, the steel tube was assumed rigid.

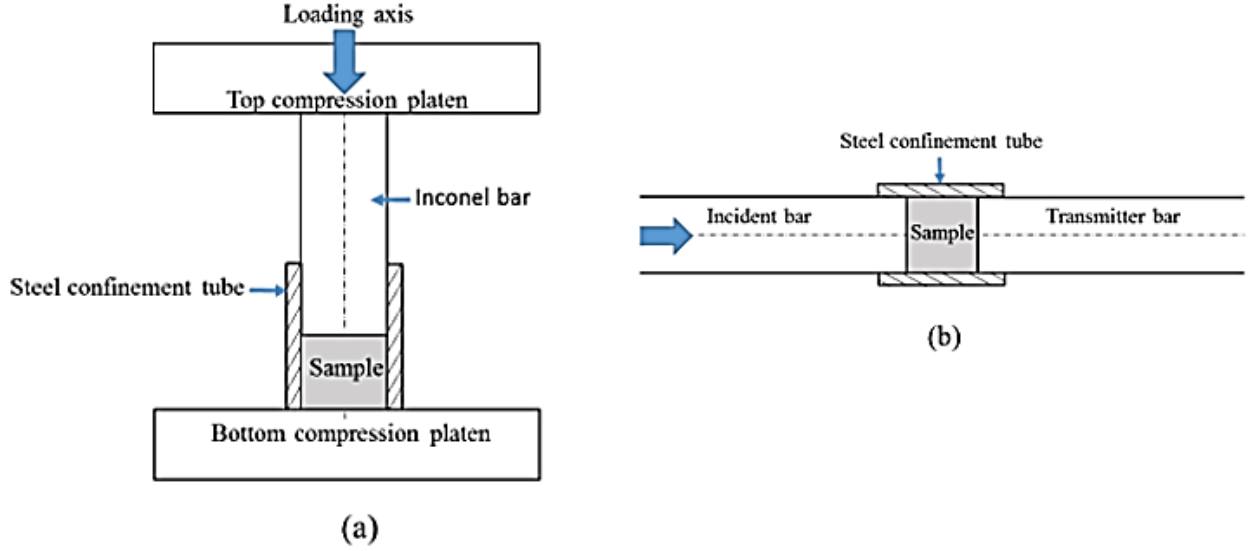


Figure 5. The schematics of confined compression tests (a) quasi-static and (b) high strain rate SHPB test

Results

Quasi-static and high strain rate compression tests

Typical incident and transmitter bar strain readings of the SHPB tests with and without pulse shaper at 8 m s^{-1} are shown in Figure 6(a). The time difference between the starting points of the reflected and transmitted waves is $\sim 25 \mu\text{s}$ (marked in Figure 6(a)) for both with and without pulse shaper tests and it is due to the wave transit time of the tested AAC sample. The use of pulse shaper as seen in the same figure increases the sample failure time from $45.5 \mu\text{s}$ to $100 \mu\text{s}$. An average elastic modulus of $\sim 0.75 \text{ GPa}$ was determined from the stress-strain curves at the same velocity. This corresponds to an elastic wave velocity of 1118 m s^{-1} and a transit time of $23 \mu\text{s}$ which is in accord with the measured transit time. The ratio of fracture time to transit time $\left(\frac{t_f}{t_t}\right)$ was calculated 1.82

and 4 for the tests with and without pulse shaper in Figure 6(a). Since the stress equilibrium was established only by using pulse shaper ($t_f \geq \pi t_t$), the SHPB compression tests were continued with the use of pulse shaper at 8 m s^{-1} (note that the velocity is lower on the incident bar). It is noted in Figure 6(a) that the front and back strain gauges mounted on the incident bar read almost the same strain, showing a negligible wave dispersion on the used Inconel 718 bars. Figure 6(b) shows the variation of stress and strain rate with strain in a typical SHPB test with a pulse shaper. As noted in the same figure, the strain rate varies with time until the fracture. The strain rate was then determined as the strain rate corresponding to the maximum stress. For the particular test shown in Figure 6(b); therefore, the strain rate at fracture is 185 s^{-1} . Note that after the failure, the strain rate increases as the sample becomes more compliant due to fracture. A common way of showing the stress equilibrium in the SHPB tests is to shift the waves to the sample/bar interface by a distance corresponding to the distance between sample and strain gauges and then calculate the equilibrium R value $\left(R = \frac{\sigma_1 + \sigma_R}{\sigma_T}\right)$. When this value reaches 1, the stress equilibrium is established in the sample.

As seen in Figure 6(b), the R value reaches 1 when the strain is ~ 0.007 . Figure 6(c) shows typical

strain gauge readings of the direct impact tests performed at 10 and 30 m s⁻¹. In these tests, front and back strain gauges were used to record the incoming wave after the impact of striker bar. The front and back gauge readings at 10 m s⁻¹ (using 50 mm-long Inconel bar) are almost the same, proving again an insignificant wave dispersion on the used Inconel bars. Also noted in the same figure that the time to fracture is 49 μs at 10 m s⁻¹, while it decreases to 34 μs at 30 m s⁻¹. These are non-equilibrium tests and prone to axial and radial inertia. The strain rates of non-equilibrium tests at 10, 30 and 108 m s⁻¹ striker bar velocities are sequentially ~385, ~1150 and ~4150 s⁻¹.

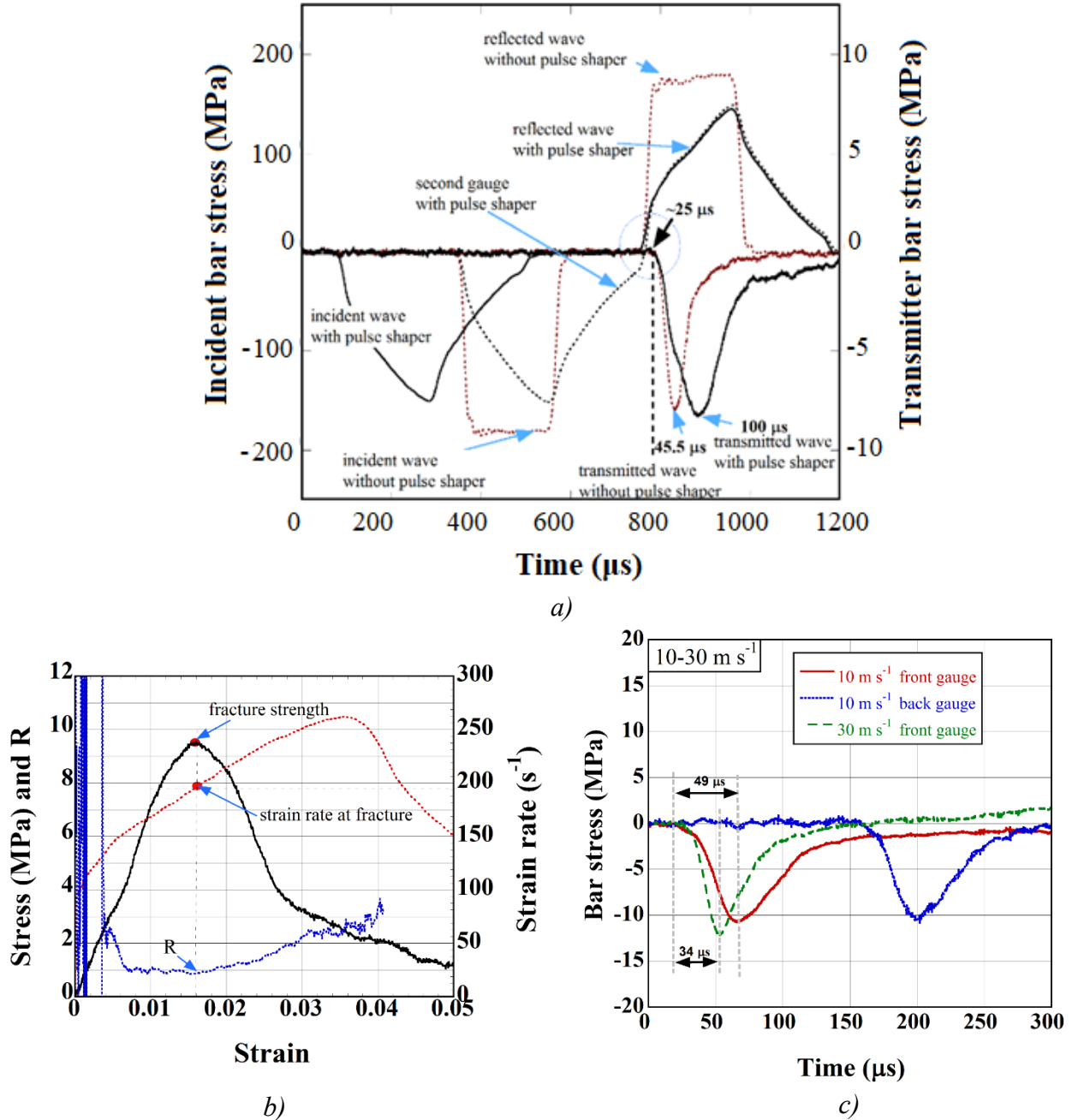


Figure 6. Typical SHPB incident and transmitter strain readings of the tests with and without pulse shaper (a) and typical stress-strain and strain rate-strain curve of SHPB test with pulse shaper (b) and direct impact test strain readings from front and back strain gauges at 10 and 30 m s⁻¹ (c)

The stress-strain curves of the quasi-static compression tests at 5x10⁻⁵ and the SHPB tests at 8 m s⁻¹ (using a pulse shaper, equilibrium test) are shown in Figures 7(a-b), respectively. The distal-end stress-time curves of the direct impact tests at 10, 30 and 108 m s⁻¹ are further shown in Figure

7(c). The maximum stress following the initial linear elastic region in these stress-strain curves is taken as the compressive strength (Figure 7(a)). As seen in Figures 7(a-c), the compressive strength increases as the velocity increases from quasi-static to 30 m s^{-1} , while the compressive strength slightly decreases when the direct impact velocity increases from 30 m s^{-1} to 108 m s^{-1} . The representative compression stress-strain curves of the tested AAC from $2 \times 10^{-3} \text{ s}^{-1}$ to 185 s^{-1} (8 m s^{-1} with pulse shaper) are shown in Figure 7(d). As noted in the same figure, the compression moduli at 35 and 185 s^{-1} are higher than those at the quasi-static strain rates, while the critical strains corresponding to the compressive strength are similar at different strain rates, $\sim 0.015\text{-}0.017$. At the highest strain rates, 1158 s^{-1} (30 ms^{-1}) and 4158 s^{-1} (108 ms^{-1}), the slopes of the initial linear region were however significantly reduced as compared with those of lower strain rates. The stress on the sample in the direct impact tests was measured only from the distal-end by the strain gauges mounted on the incident bar. Therefore, the stress measurement did not show the average stress of the sample at 1150 and 4150 s^{-1} as the axial and radial inertial effects were predominant at these strain rates. The mean compressive strengths of the tested AAC sample are listed in Table 1 together with test velocity, strain rate and the test type.

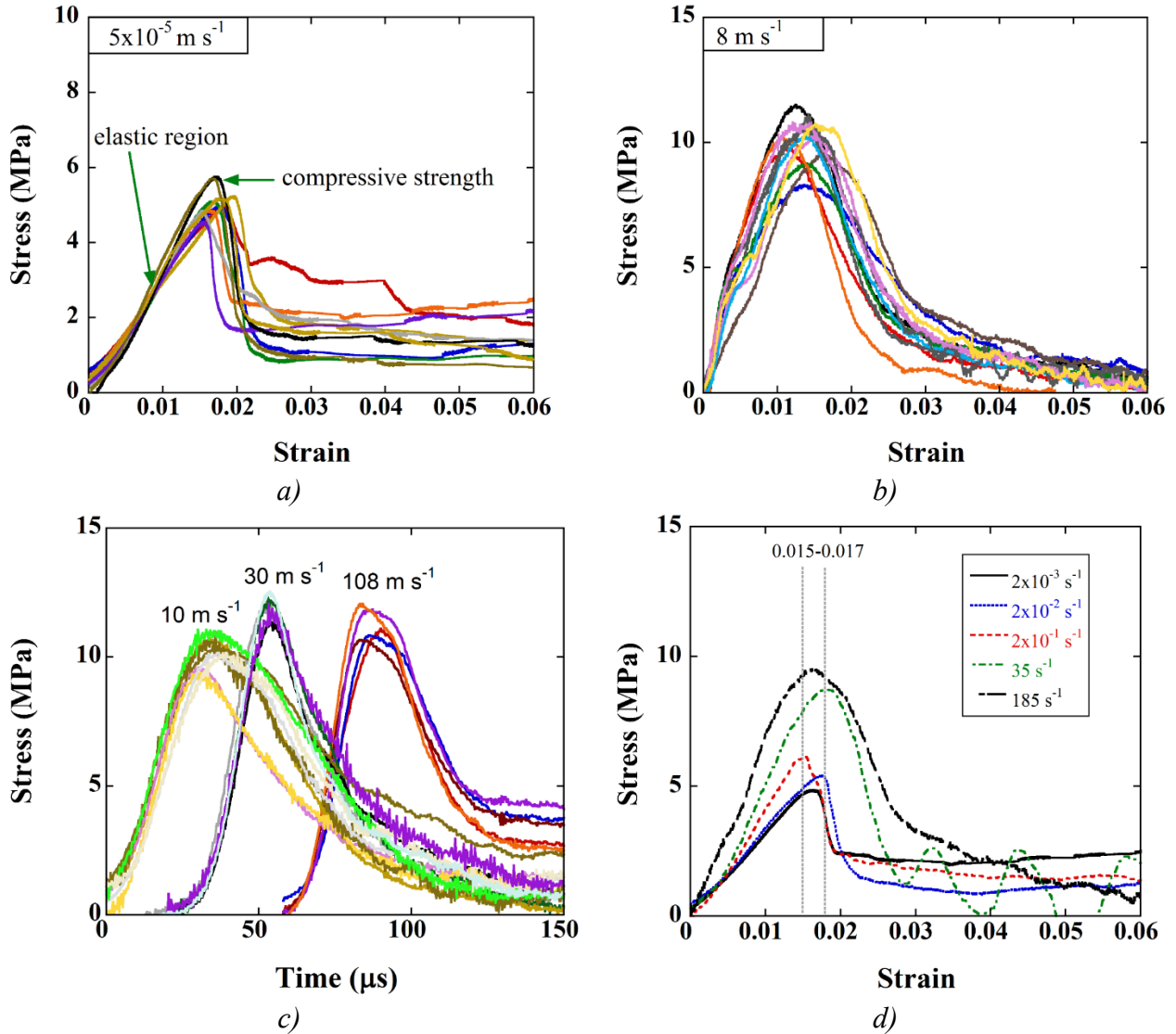


Figure 7. The compression stress-strain curves at (a) 5×10^{-5} and (b) 8 m s^{-1} (equilibrium test) and (c) the compression stress-time curves at 10 , 30 and 108 m s^{-1} and (d) the equilibrium test stress-strain curves at different strain rates

The failure at quasi-static velocities occurs by the initiation of a single axial crack at the bottom compression test platen as shown by arrows in Figures 8(a-b). Additional axial cracks, as seen in the same figures, then form as the upper compression test platen continuously compresses the sample. As opposite to quasi-static compression tests, the failure at increasing velocities from 1 to 108 m s⁻¹ starts from the impact-end (Figures 8(c-g)).

Table 1 The mean compression strengths of the quasi-static, drop-weight, SHPB and direct impact compression tests together with test velocity and strain rate and the type of test

Velocity (m s ⁻¹)	Approximate strain rate (s ⁻¹)	Test	σ_m (MPa)
5×10^{-5}	2×10^{-3}	Quasi-static compression	5.11
5×10^{-4}	2×10^{-2}	Quasi-static compression	5.37
5×10^{-3}	2×10^{-1}	Quasi-static compression	5.89
1	35	Drop-weight	7.34
8	185	SHPB	9.9
10	385	Direct impact	10.2
30	1150	Direct impact	11.70
108	4150	Direct impact	11.60

The failure at quasi-static velocities occurs by the initiation of a single axial crack at the bottom compression test platen as shown by arrows in Figures 8(a-b). Additional axial cracks, as seen in the same figures, then form as the upper compression test platen continuously compresses the sample. As opposite to quasi-static compression tests, the failure at increasing velocities from 1 to 108 m s⁻¹ starts from the impact-end (Figures 8(c-g)).

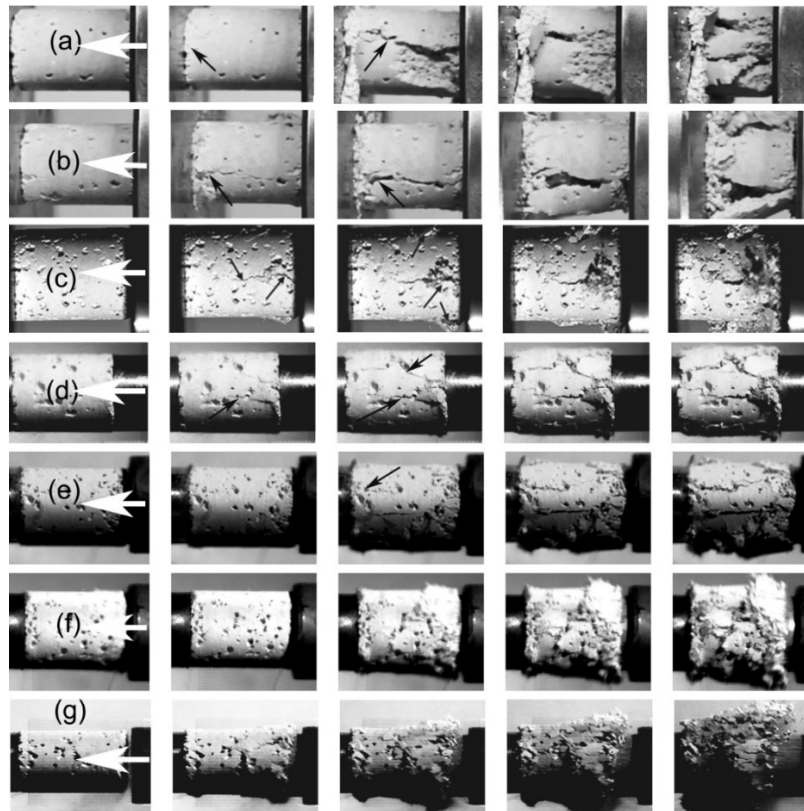


Figure 8. The deformation pictures of the samples tested at (a) 5×10^{-5} , (b) 5×10^{-3} (c) 1 (drop tower), (d) 8 (SHPB), (e) 10 (f) 30 and (g) 108 m s⁻¹ at different displacements before and after the failure (the white arrows show the upper compression test platen in quasi-static tests and the impact-end in dynamic tests and the black ones show the cracks)

The failure in drop-weight test and at 8 and 10 m s⁻¹ also occurs dominantly by axial cracking, while circumferential cracks at the impact-end are also noted (Figures 8(c-e)). However, the extensive cracking composing of both axial and circumferential cracks is seen at the impact-end of the samples tested at 30 and 108 m s⁻¹ (Figures 8(f) and (g)). The number of cracks also increase significantly at these velocities, clearly indicating the effect of velocity on the fracture behavior of the tested AAC.

Quasi-static and dynamic indentation and confined compression tests

Figure 9(a) shows the indentation force-displacement curves of 5 and 10 mm indenters at 5×10^{-5} m s⁻¹. A mean force of 5 tests for each indenter was calculated as seen in the same figure. The indentation force initially increases linearly with increasing displacement until about a critical force at which the indenter starts to penetrate the sample. Following the indenter penetration, the force increases less gradually with increasing displacement. As seen in Figure 9(b), the average indentation stress (mean force/indenter area) decreases as the indenter size increases, while the indentation stress saturates at and above 25 mm indenter sizes. The increase of indentation stress with increasing displacement is partly due to the powder accumulation in the front of indenter as depicted in the inset of Figure 9(b) for 30 mm indenter. Figure 9(c) shows the indentation stress-displacement curves of 20 mm indenter at 5×10^{-5} , 5×10^{-4} and 5×10^{-3} m s⁻¹.

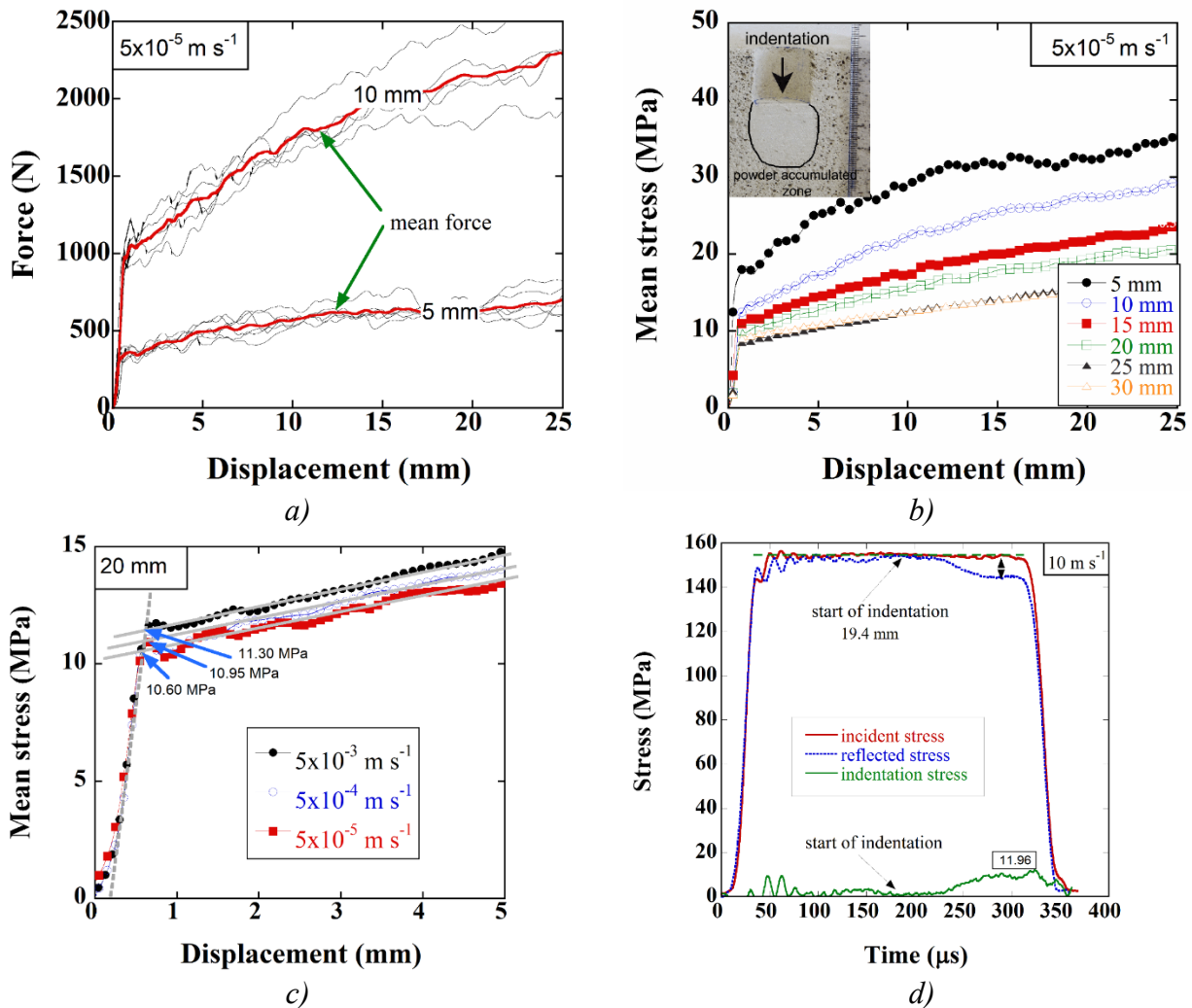


Figure 9. the indentation force-displacement and mean force-displacement curves of 5 and 10 mm indenters at 5×10^{-5} m s⁻¹ (a), mean stress-displacement curves at different indenter sizes at 5×10^{-5} m s⁻¹ (b), indentation stress-displacement curves using 20 indenter at different velocities and determination of indentation strength (c) and the stress-time curve of a dynamic indentation test using 19.4 mm incident bar (d)

As shown in the same figure, the intercept of a linear line drawn in the elastic region and a linear line drawn in the indenter penetration region is taken as the average indentation strength which corresponds to the stress at which the indenter starts to penetrate the sample. In the calculations of the indentation strength, the shear and frictional forces were not taken into account. However, the saturation of the indentation strength after 25 mm indenter size implies that the compression force is significantly higher than the shear and frictional forces and therefore can be used to calculate the indentation strength. Figure 9(d) shows the incident and reflected (shifted) stresses of a SHPB indentation test together with the calculated indentation stress at 10 m s^{-1} . The indentation stress was calculated as the stress difference between incident and shifted-reflected stresses. As noted in the same figure, the indentation of the incident bar to the sample starts after about a time which is reflected as the reduced reflected stress in Figure 9(d). The indentation stresses were calculated 11.96, 11.54 and 12.10 MPa with an average of 11.87 MPa at 10 m s^{-1} .

No pulse shaper was used in the confined compression tests since the samples in these tests deformed without fracture until about large strains. Typical SHPB test incident, reflected and transmitted waves of the confined compression test at 8 m s^{-1} are shown in Figure 10(a). The strain rate in these tests was almost constant and approximately 330 s^{-1} . As noted in the same figure, the time difference between starting points of the reflected and transmitted waves is again $\sim 25 \mu\text{s}$ and the confinement tube is not relaxed quickly, imposing a residual stress on the transmitter bar at the end of the transmitter bar strain reading (Figure 10(a)). Figure 10(b) shows the stress-strain curves of the confined compression tests at $5 \times 10^{-4} \text{ m s}^{-1}$ and 8 m s^{-1} . The confined tests at quasi-static strain rate continued until about large strains (0.4) and the sample was compressed (densified) without fracture as depicted in the inset of Figure 10(b). The initial linear elastic region of the confined tests in Figure 10(b) is followed by a non-linear increase of the stress after about a strain of 0.02. The corresponding stress at 0.02 strain is taken as the confinement strength and it varies between 4.83 and 8.51 MPa ($\sigma_m = 7.73 \text{ MPa}$). These values are higher than the fracture strengths of the unconfined tests at the same velocity ($\sigma_m = 5.89 \text{ MPa}$). The samples tested at 8 m s^{-1} are again densified as the strain increases and show almost no fracture as depicted in the inset of Figure 10(b). The final strain attained in these tests is about 6%.

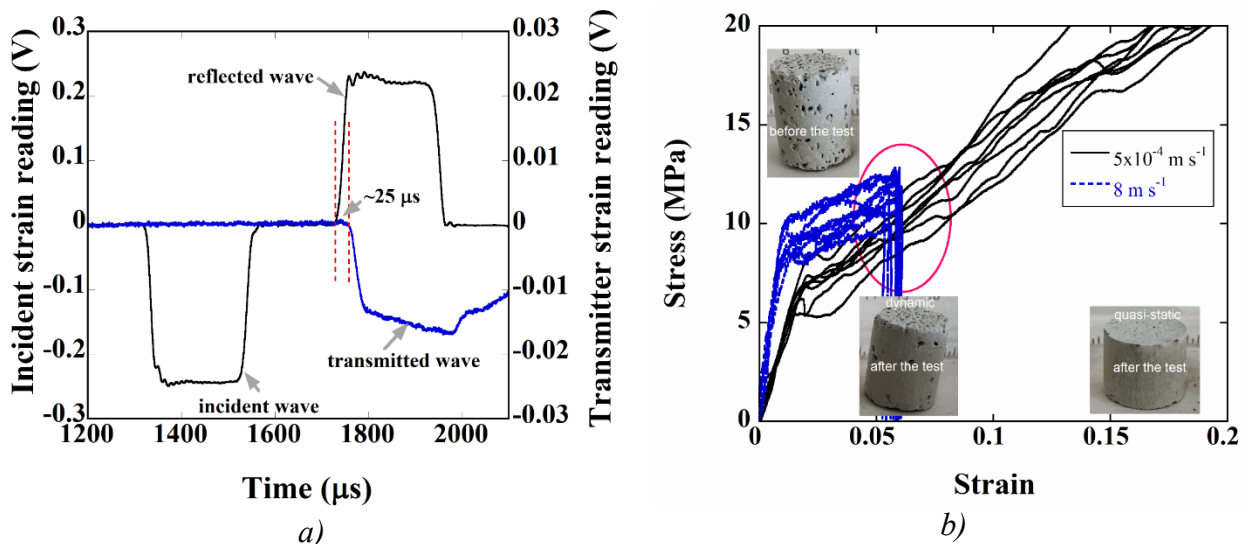


Figure 10 (a) the incident and transmitter strain readings of a confined compression test in SHPB at 8 m s^{-1} and (b) the dynamic and static confined compression stress-strain curves and the pictures of deformed and recovered test samples

The compressive strengths of confined SHPB tests are however slightly lower than those of unconfined SHPB tests, varying between 7.96 and 10.42 MPa with a mean stress of 9.11 MPa at $\sim 330 \text{ s}^{-1}$ (the mean strength of unconfined compression tests is 9.85 MPa at 185 s^{-1}). The confined

compression strengths of SHPB tests are however higher than of those of quasi-static tests as shown in Figure 10(b). Although the dynamic confined compression tests show higher initial stresses, the stresses of both tests approach to each other at increasing strains as seen in Figure 10(b).

Discussion

The variations of the compression (Table 1) and confined compression and compression and mean indentation (20 and 30 mm) strengths are shown in Figures 11(a) and (b), respectively. Note that as the stresses on the sample was measured only from the distal-end by the strain gauges mounted on the incident bar in the direct impact tests, the stress measurement did not show the average stress of the samples tested at 320, 1150 and 4150 s⁻¹. The compressive strength variation in Figure 11(a) may be considered in two sequential regions: a lower velocity-dependent strength region (Region 1-solid line) at quasi-static velocities and a higher velocity-dependent strength region (Region 2-dashed line) at high velocities, showing the first turning point of the s-type curve.

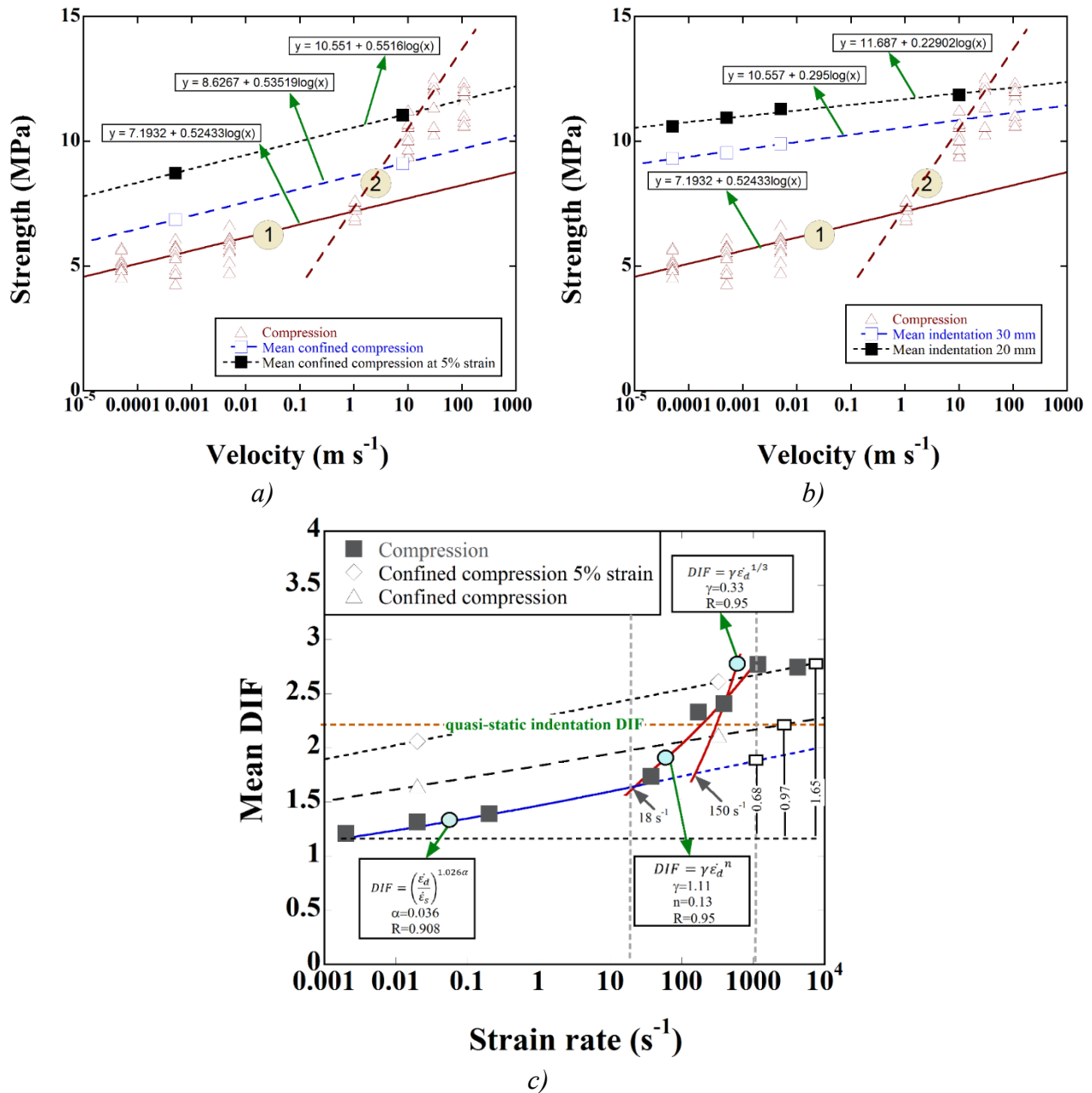


Figure 11. The variations of strength with velocity in (a) compression and confined compression tests and (b) compression and indentation tests, and (c) the mean DIF values as function of strain rate

The confined compression stresses at 5% strain are also shown in the same figure for comparison. One of the problems in the dynamic and quasi-static confined compression tests is the establishment of a full-confinement state since the material near the confinement-circular-steel-tube-wall fractures easily, resulting in reduced pressure on the sample and hence invalidating a full-confinement state. The second problem is the prevention of the friction forces between sample and confinement-tube wall. Third, increasing strain also increases confinement stress. Nevertheless, the mean confined and indentation strength values in the same figure increase as the velocity increases. The mean indentation strength values, showing presumably the full-confined state, are slightly higher than the mean confined compression strength values (Figure 11(b)). The dynamic indentation tests using the incident bar (19.4 mm) also result in similar mean strength values with the dynamic compression tests. The results of linear fits to the compression, mean indentation and confined compression strength values are also shown in Figures 11(a) and (b). The fitting results show comparable slopes between the confined compression and compressive strength, while the slope of the indentation strength is lower than that of the compressive strength in Region 1.

The failure of brittle materials proceeds with crack opening and growth. At quasi-static strain rates, the energy needed for crack opening is much higher than the energy needed for crack growth. Therefore, few cracks grow under static loading through the weakest path along in the axial direction. At increasing strain rates, there is however less time for both crack opening and growth. This causes an increase in the strength and number of micro cracks formed at increasing strain rates. The fracture mechanism considered here is thermally activated and both increasing strain rate and decreasing temperature increase the fracture strength of concrete [17-19]. A similar effect was also found in the present study. Until about 8 m s^{-1} , the main failure mechanism was the axial crack formation and propagation, while circumferential cracks developed at and after 30 m s^{-1} . The specimen pulverizations at the impact-end after a critical velocity seen in Figures 8(e) and (d) also agreed with a previous study on AAC sample [11].

Furthermore, the cracks were observed to initiate at the impact-end and then propagated axially normal to the circumferential tensile strain (Poisson's expansion) at low strain rates. At increasing strain rates, the cracks propagated normal to the axial loading direction (circumferential cracks). As the radial inertia became more effective at increasing strain rates, the increased constraint effect induced a complex deformation pattern accompanied with the stress wave reflections from the already formed-crack surfaces, the cell walls and edges and also from the surfaces of the sample. The crack bifurcation presumably resulted in fragmentation at the impact-end. The International Federation for Structural Concrete (CEB) recommended two empirical equations to define the DIF of concrete strength as [35]

$$DIF = \frac{\sigma_d}{\sigma_s} = \left(\frac{\dot{\epsilon}_d}{\dot{\epsilon}_s} \right)^{1.026\alpha} \quad \dot{\epsilon}_d \leq 30s^{-1} \quad (9)$$

$$DIF = \frac{\sigma_d}{\sigma_s} = \gamma \dot{\epsilon}_d^{1/3} \quad \dot{\epsilon}_d > 30s^{-1} \quad (10)$$

where, $\dot{\epsilon}_d$ and $\dot{\epsilon}_s$ are the dynamic and static strain rates. The value of $\dot{\epsilon}_s$ is $3 \times 10^{-5} \text{ s}^{-1}$, $\gamma = 10^{6.156-2}$ and $\alpha = \frac{1}{\left(5 + \frac{\sigma_s}{10}\right)}$. Figure 11(c) shows the mean DIF values of the compressive strength as function

of strain rate and the fitting parameters of Eqn. 9 and Eqn. 10. The value of α in Eqn.9 and γ in Eqn. 10 is ~ 0.036 and ~ 0.33 , respectively. The critical strain rate for the increased compressive strength

is predicted 150 s^{-1} in Figure 11(c). The dynamic compressive strength values are also fitted with $\frac{\sigma_d}{\sigma_s} = \gamma \dot{\epsilon}_d^n$, where $n=0.13$ and $\gamma=1.11$, which results in a critical strain rate of $\sim 18 \text{ s}^{-1}$ as shown in

Figure 11(c). This equation shows a better fit to the DIF than Eqn. 10. Since the strain rate in indentation tests cannot be determined, the mean DIF value of the quasi-static indentation tests is shown as a dotted line in Figure 11(c). Assuming a full confinement state in the indentation tests, an increase of 0.97 in the DIF is found between 2×10^{-3} and 1150 s^{-1} (Figure 11(c)). The extrapolation of the Eqn. 9 to 1150 s^{-1} in the same strain rate interval gives an increase of 0.68 in the DIF. The addition of both values (0.97 and 0.68) results in an increase of 1.65 in the DIF between 2×10^{-3} and 1150 s^{-1} , which is the same as the experimentally determined increase in the DIF (1.65) in the same strain rate interval as shown in Figure 11(c). From these results, the inertia and strain rate contributions to the enhancement of DIF until 1150 s^{-1} are determined about 60% and 40%, respectively. Linear fits to mean DIF values of confined compression strengths also give the similar slopes with that of the compressive strength in Region 1 as shown in Figure 11(c).

The critical strain rate for the passage to the 1D state of strain was shown to depend on the diameters of test samples; larger diameters showed larger inertial effects; hence, lower critical strain rates for the passage to the 1D state of strain [28]. The strength values measured in the present study correspond to non-equilibrium tests at and above 10 m s^{-1} . Therefore, the strength values above this velocity corresponded to the distal-end stress in the SHPB, while the impact-end stress might be larger and can only be determined through the finite element simulations or measured by placing impedance-matched quartz crystals at the impact-end of tested sample. This is left for future studies. Also, the calculated contributions of strain rate and inertia to the strength should be carefully approached as these ratios are both geometry and material dependent, hence cannot be generalized.

When modelling such brittle cellular materials against impact loading, the inertial effects should be excluded from constitutive equation. In many occasions, the stress rise due to inertia is considered as the material's intrinsic response to increasing strain rates, an effect which is also seen in testing ceramic materials. The results of this study emphasize this fact, besides following a scientific curiosity on the strain rate sensitivity of brittle cellular structures.

Conclusions

The strain rate dependent compressive strength of an autoclaved aerated concrete with a density of 600 kg m^{-3} was experimentally investigated between quasi-static ($2 \times 10^{-3} \text{ s}^{-1}$) and dynamic ($\sim 4150 \text{ s}^{-1}$) strain rates. High strain rate equilibrium and direct impact non-equilibrium compression tests were conducted in a compression Split Hopkinson Pressure Bar. Quasi-static and high strain rate indentation and confinement compression tests were also implemented in order to clarify the effect of confinement on the fracture strength. The experimental results showed two different regions of compressive strength-dependency on the strain rate: a low-strain rate-dependent region from quasi-static to $\sim 18 \text{ s}^{-1}$ and a high-strain-rate dependent region from $\sim 18 \text{ s}^{-1}$ to higher strain rates. In parallel with this, the failure at quasi-static velocities occurred by the progression of a single axial crack initiated at the bottom compression test plate. At increasing velocities; however, the extensive cracking of the sample composing of both axial and circumferential cracks was detected, showing the effect of inertia on the fracture behavior of the tested autoclaved aerated concrete. The mean confined and indentation strength values also increased as the velocity increased and the mean confined compression strength values were shown comparable with the dynamic compressive strength values in the low-strain rate-dependent region. The contributions of the inertia and strain rate to the enhancement of dynamic increase factor until about 1000 s^{-1} were predicted about 60% and 40% for the studied test sample and its geometry, respectively.

Acknowledgement

Authors would like to thank AKG Gaz Beton of Turkey for providing AAC blocks for the present study.

The authors declare that they have no conflict of interest.

REFERENCES

- [1] Narayanan, N., Ramamurthy, K. *Structure and properties of aerated concrete: a review*. Cement and Concrete composites, 2000, 22, pp. 321-329.
- [2] Scheffler, M., and Colombo, P. *Cellular ceramics*. Structure, Manufacturing, Properties and Applications, 2005, 670 p.
- [3] Hu W., Neufeld, R.D., Vallejo, L.E., Kelly, C. and Latona, M. *Properties of autoclaved cellular concrete with high volume fly ash*. J Energy Eng-ASCE, 1997, 123, pp 44-54.
- [4] Narayanan, N. and Ramamurthy, K. *Microstructural investigations on aerated concrete*. Cement and Concrete Research, 2000, 30, pp. 457-464.
- [5] Ramamurthy, K. and Narayanan, N. *Influence of composition and curing on drying shrinkage of aerated concrete*. Materials and Structures, 2000, 33, pp. 243-250.
- [6] Bonakdar, A., Babbitt, F. and Mobasher, B. *Physical and mechanical characterization of Fiber-Reinforced Aerated Concrete (FRAC)*. Cem Concr Compos, 2013, 38, pp. 82-91.
- [7] Chen, Y., Peng, M., Zhang, Y. and Liu, Y. *Mechanical Properties of Autoclaved Aerated Concrete with Different Densities*, 2013.
- [8] Fapohunda, C., Ikponmwosa, E. and Falade, F. *Evaluation of strength relations in foamed aerated concrete containing pulverized bone (PB) as a partial replacement of cement*. Engineering Review, 2018, 38, pp. 20-29.
- [9] Yankelevsky, D.Z. and Avnon, I. *Autoclaved aerated concrete behavior under explosive action*. Construction and Building Materials, 1998, 12, 359-364.
- [10] Mespoulet, J., Plassard, F. and Hereil, P.L. *Strain rate sensitivity of autoclaved aerated concrete from quasi-static regime to shock loading*. In: Dymat 2015 - 11th International Conference on the Mechanical and Physical Behaviour of Materials under Dynamic Loading, E. Cadoni (Ed). E D P Sciences, Cedex A.
- [11] Belouettar, R., Klepaczko, J.R. and Edps. *A study of dynamic behavior of the autoclaved aerated concrete*. DYMAT 2009 - 9th International Conference on the Mechanical and Physical Behaviour of Materials under Dynamic Loading, 2009, Vol. 1, pp. 503-509.
- [12] Khosravani, M.R. and Weinberg, K. *A review on split Hopkinson bar experiments on the dynamic characterisation of concrete*. Constr Build Mater, 2018, 190, pp. 1264-1283.
- [13] Brace, W.F. and Jones, A.H. *Comparison of uniaxial deformation in shock and static loading of 3 rocks*. Journal of Geophysical Research, 1971, 76, pp. 4913-4921.
- [14] Grady, D.E. *Shock-wave compression of brittle solids*. Mechanics of Materials, 1998, 29, pp. 181-203.
- [15] Yu, S.S., Lu, Y.B. and Cai, Y. *The strain-rate effect of engineering materials and its unified model*. Lat Am J Solids Struct, 2013, 10, pp. 833-844.
- [16] Bischoff, P.H. and Perry, S.H. *Compressive behavior of concrete at high-strain rates*. Materials and Structures, 1991, 24, pp. 425-450.
- [17] Zhang, Q.B. and Zhao, J. *A Review of Dynamic Experimental Techniques and Mechanical Behaviour of Rock Materials*. Rock Mech Rock Eng, 2014, 47, pp. 1411-1478.
- [18] Lu, D.C., Wang, G.S., Du, X.L. and Wang, Y. *A nonlinear dynamic uniaxial strength criterion that considers the ultimate dynamic strength of concrete*. International Journal of Impact Engineering, 2017, 103, pp. 124-137.
- [19] Lindholm, U.S., Yeakley, L.M. and Nagy, A. *The dynamic strength and fracture properties of dresser basalt*. International Journal of Rock Mechanics and Mining Sciences & Geomechanics Abstracts, 1974, 11, pp. 181-191.
- [20] Reinhardt, H.W., Rossi, P., van Mier. *Joint investigation of concrete at high rates of loading*. Structures, 1990, 23, pp. 213-216.
- [21] Wang, Q.F., Liu, Y.H. and Peng, G. *Effect of water pressure on mechanical behavior of concrete under dynamic compression state*. Construction and Building Materials, 2016, 125, pp. 501-509.

- [22] Rossi, P.J.M. and Structures. *A physical phenomenon which can explain the mechanical behaviour of concrete under high strain rates*. 1991, 24, pp. 422-424.
- [23] Rossi, P., Toutlemonde F.J.M. and Structures. *Effect of loading rate on the tensile behaviour of concrete: description of the physical mechanisms*. 1996, 29, 116 p.
- [24] Zeng, S.J., Ren, X.D. and Li, J. *Triaxial Behavior of Concrete Subjected to Dynamic Compression*. J Struct Eng-ASCE, 2013, 139, pp. 1582-1592.
- [25] Legeron, F. and Paultre, P. *Uniaxial confinement model for normal- and high-strength concrete columns*. J Struct Eng-ASCE, 2003, 129, pp. 241-252.
- [26] Sfer, D., Carol, I., Gettu, R. and Etse, G. *Study of the behavior of concrete under triaxial compression*. J Eng Mech-ASCE, 2002, 128, pp. 156-163.
- [27] Lahlou, K., Lachemi, M. and Aitcin, P.C. *Confined high-strength concrete under dynamic compressive loading*. J Struct Eng-ASCE, 1999, 125, pp. 1100-1108.
- [28] Liu, F. and Li, Q.M. *Strain-rate effect on the compressive strength of brittle materials and its implementation into material strength model*. International Journal of Impact Engineering, 2019, 130, pp. 113-123.
- [29] Davies, E.D.H. and Hunter, S.C. *The dynamic compression testing of solids by the method of the split Hopkinson pressure bar*. Journal of the Mechanics and Physics of Solids, 1963, 11, pp. 155-179.
- [30] Tekoglu, C., Gibson, L.J., Pardoan, T. and Onck, P.R. *Size effects in foams: Experiments and modeling*. Progress in Materials Science, 2011, 56, pp. 109-138.
- [31] Jin, T., Zhou, Z.W., Wang, Z.H., Wu, G.Y. and Shu, X.F. *Experimental study on the effects of specimen in-plane size on the mechanical behavior of aluminum hexagonal honeycombs*. Mater Sci Eng A-Struct Mater Prop Microstruct Process, 2015, 635, pp. 23-35.
- [32] ASTM C. *Standard test method for compressive strength of cylindrical concrete specimens*. In: Book Standard test method for compressive strength of cylindrical concrete specimens, 2019.
- [33] Kolsky, H. *An Investigation of the Mechanical Properties of Materials at Very High Rates of Loading*. Proceedings of the Physical Society Section B, 1949, 62(11), pp. 676-700.
- [34] Ravichandran, G. and Subhash, G. *Critical-appraisal of limiting strain rates for compression testing of ceramics in a split hopkinson pressure bar*. J Am Ceram Soc, 1994, 77, pp. 263-267.
- [35] CEB. *Concrete structures under impact and impulsive loading*. In: Book Concrete structures under impact and impulsive loading. Bulletin d'information, 1998, No 187, CEB Comite' EuroInternational du Be'ton.

Received: 28.01.2023

Accepted: 15.05.2023



MODEL OF MACHINING PROCESS CONTROL ON MULTI-TOOL SINGLE-CARRIAGE ADJUSTMENTS

Nizami YUSUBOV^{1*}, Heyran ABBASOVA²

^{1*,2} Department of Machine Building Technology, Azerbaijan Technical University, Baku, Azerbaijan

E-mail: nizami.yusubov@aztu.edu.az^{1*}, abbasova.heyran@aztu.edu.az²

Abstract: Based on the developed models, the article reveals the degree of influence on the machining accuracy of a complex of technological factors, including the structure of a multi-tool single-carriage adjustment, the deformation properties of the subsystems of the technological system, cutting conditions. A number of ways to control multi-tool single-carriage machining based on the developed accuracy models are shown, including improvements in the structure of multi-tool single-carriage adjustment, calculations of limiting cutting conditions. The developed control models make it possible to predict the accuracy of machining for given conditions, including such technological components as the adjustment structure, properties of the technological system, machining conditions, thereby creating a methodological base for CAD for multi-tool single-carriage machining. They can serve as a basis for developing a digital twin model of the process.

Keywords: control model, multi-tool machining, multi-tool single-carriage adjustment, machining productivity, predetermined dimensional accuracy, scattering fields, matrix model of accuracy.

Introduction. One of the most important factors in improving the productivity of the technological process is the concentration of transitions. The highest efficiency of concentration of transition is ensured by its implementation in multi-tool adjustments [1-6]. Dimensional accuracy is a paramount requirement in the design, debugging and implementation of the technological process. In the works of Koshin and Yusubov, the principles were formulated and the foundations of the theory of dimensional accuracy design of multi-tool machining were laid [1-6].

The basis of the theory of accuracy of multi-tool machining is mathematical models of the accuracy of dimensions performed by multi-tool adjustment tools. Therefore, of particular interest is the current level of mathematical models for the formation of dimensional errors in single-tool and multi-tool adjustments. [1-11].

As in the case of single-tool machining [7], for multi-tool single-carriage adjustments, the inverse problem is more relevant: assign the maximum allowable cutting conditions (and possibly other setup parameters) to ensure the highest productivity with a given dimensional accuracy [1].

Since the feed has the greatest influence on the values of the components of the cutting forces, here it is also advisable to take the feed as the main control parameter, which is the same control factor for all setting tools. To develop a control model, it is enough from the simulation model (3.117), (3.118), (3.119) [2], to highlight the dependence of the feed on the required accuracy and other machining parameters.

Process control model for multi-tool single-carriage machining. For homogeneous adjustments from equation (3.116) [2] we obtain:

$$\Delta g \geq e^{01} \left\{ \omega \cdot \sum_i \overline{p_{ti}} + \sum_i \overline{p_{\Delta ti}} \right\} \quad (1)$$

In formula (1), Δg is the allowable value of the scattering field. It is due to the requirements for

the accuracy of the dimension and is calculated by the formula:

$$\Delta g = \sqrt{TD^2 - \Delta_{adj}^2 - \Delta_{wear}^2 - 3(\Sigma \Delta_m)^2 - 3(\Sigma \Delta_T)^2} \quad (2)$$

where TD is the value of the tolerance field of the dimension being performed; Δ_{adj} - the adjustment error of the machine to the dimension being performed; Δ_{wear} - error due to dimensional wear of the cutting tool; $\Sigma \Delta_m$ - geometric errors of the machine, affecting the performed dimension; $\Sigma \Delta_T$ - error due to thermal deformations of the technological system [12]. e^{01} - combined matrix of compliance of the technological system as a whole; ω - the value of the total scattering of the properties of the technological system. Designation: $\Delta_j + \nu = \omega$ [2], where, ν is the variability of mechanical properties (for example, hardness) of workpieces within a batch, Δ_j - variation in stiffness of different machines of the same model; vector $\sum_i \overline{p_{ti}}$ characterizes the degree of influence of depths of cut t_i , vector $\sum_i \overline{p_{\Delta ti}}$ characterizes the degree of influence of allowance fluctuations Δt_i [1].

The values of fluctuations in the depth of cut Δt , determined by the initial error of the workpiece for each tool, are calculated by the formula:

$$\Delta t = TZ + \Delta_{adj} + \Delta_{wear} + \Delta_m \quad (3)$$

where TZ is the value of the workpiece tolerance field for the dimension being performed.

Thus, the group of dependencies (1), (2), (3) is a model of feed control according to the criterion of accuracy of performed dimensions for multi-tool single-carriage machining.

To find the feed with the other machining parameters given, inequality (1) must be resolved relatively S . However, the right side of the inequality is a piecewise analytic transcendental expression with respect to a variable, which does not allow an analytic representation of the inverse function. Therefore, for the practical use of the control model (1), the "Maple 7" application package is proposed, where a system of nonlinear and transcendental equations can be solved using the "solve" function. For the algorithmic representation of the control model, a computer program has been developed that allows using a computer to calculate the maximum allowable feeds in terms of accuracy for any set of other technological factors.

Performance of the process control model in multi-tool single-carriage machining. The performance of the control models (1), (2), (3) in terms of taking into account the main factors of the formation of scattering fields, using the example of adjustment from turning cutters, is illustrated by the graphs in Figure 1.

Here, to the right of the graphs, changes are indicated relative to the basic version, and inside the field of graphs - changes relative to the base curve, which in this case corresponds to $n=1$, i.e., single-tool machining.

It can be seen that the required accuracy of the dimension being performed has the strongest influence on the feed: reducing the accuracy requirements to ITD 13 allows you to increase the feed by 83-90%, and for ITD 14 - by 260-275%. At the same time, the influence of multi-tooling is preserved: in the basic version (Fig. 1 a) and in the versions for ITD 13 (Fig. 1 b) and ITD 14 (Fig. 1 c), working with a block of two cutters, while maintaining the total depth of cut, reduces the feed by 28 %, for three cutters by 45% and for four by 4-55%.

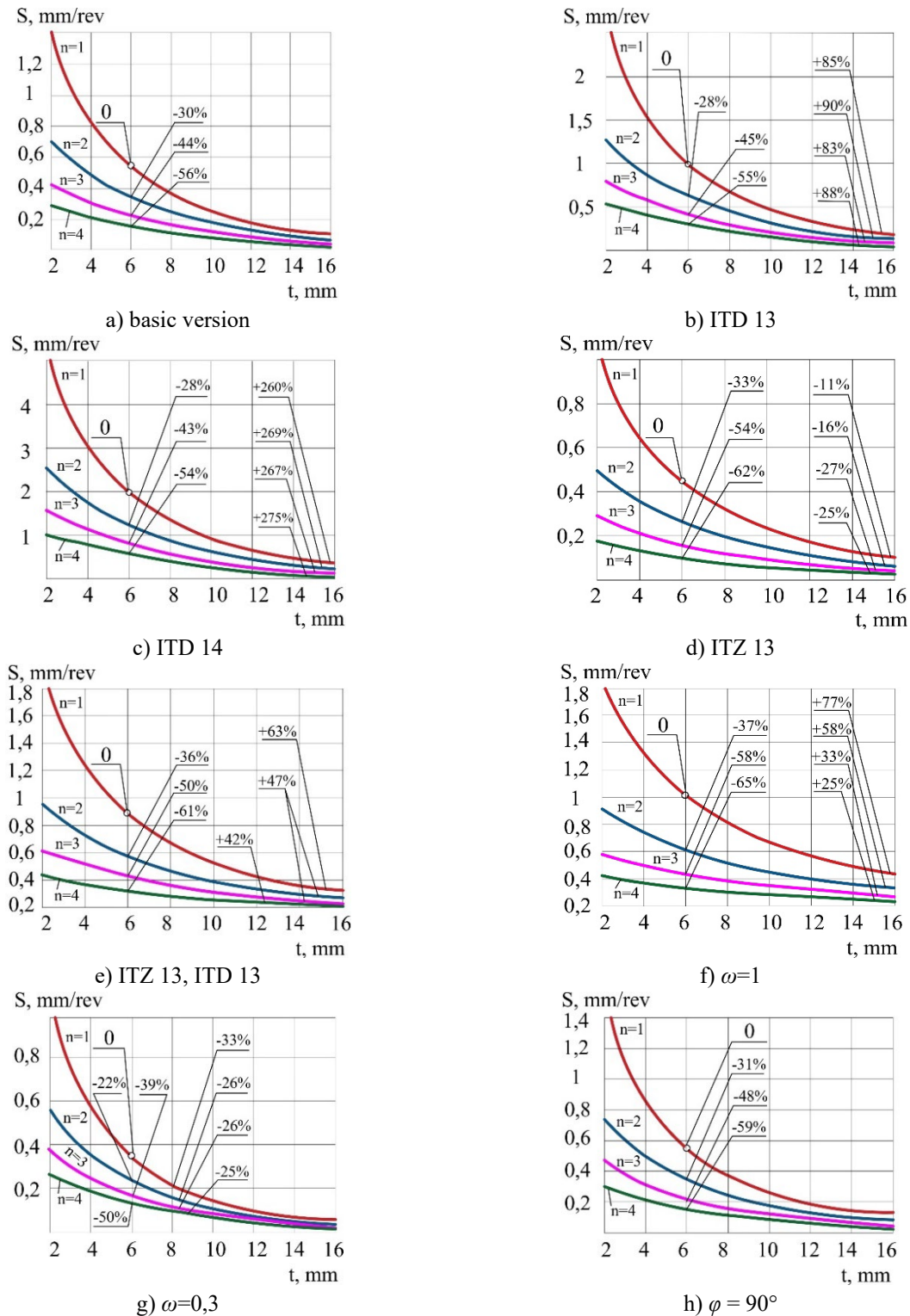


Figure 1. The influence of technological factors on the feed, limit accuracy of diametrical dimensions, in multi-tool single-carriage machining (setup - Fig. 3.7. [2]). Basic version: the workpiece – stamping, precision of every surface ITZ12, Steel 45; tools – turning cutters (n -number) P6M5, $\varphi=60^\circ$, $\gamma=15^\circ$, $r=2\text{mm}$; instability of the technological system $\omega=0,2$; the total depth of cut is evenly distributed over all the cutters of the setup. Changes are indicated for other versions.

As can be seen from fig. 1 (a), in the basic version, we have real feeds (0.4-0.6 mm / rev) for adjustment not exceeding 2 cutters. For roughing (ITD13-14), setups of 3-4 tools are allowed.

Working with coarser workpieces leads to a decrease in feed (Fig. 1 d). The combined influence of the initial error of the workpiece and the accuracy of the performed dimension is shown in fig. 1 (e). Stabilization of the properties of the technological system (Fig. 1 f, g) has a noticeable effect on the limit feed, allowing it to be increased by 25 - 77%. Figure 1 (h) shows the effect of the geometry of the cutters on the limit feed: an increase in the main angle in the lead up to 90 ° allows you to increase the feed by almost 2 times.

Patterns for linear dimensions, when they are formed from a transverse carriage, are shown in fig. 2.

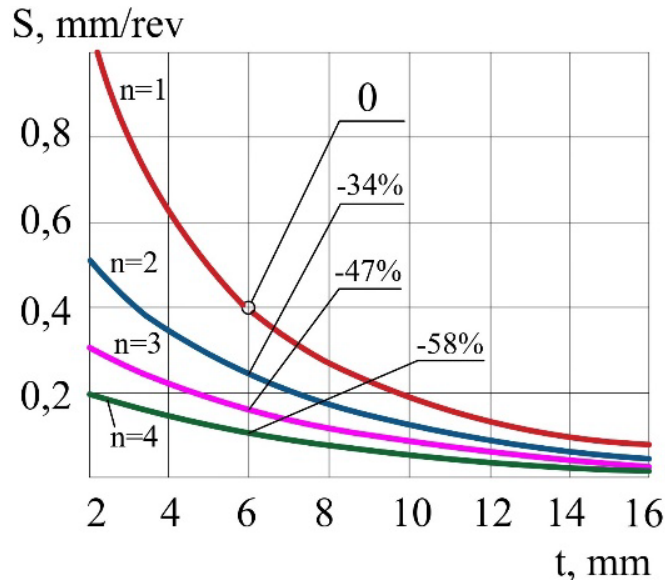


Figure 2. The influence of technological factors on the feed, the limit accuracy of linear dimensions, in multi-tool single-carriage machining with facing cutters (conditions according to Fig. 1)

Figure 3 shows the effect of accuracy requirements on the limit feed for different versions for multi-tool single-carriage adjustments with a total depth of cut $t=6$ mm. From the basic version (Fig. 3 a) it follows that machining according to the 12th grade is possible only for setting up 1-2 cutters, 11th grade can be provided with only one cutter. Machining according to ITD13 and ITD14 is possible with simultaneous operation of up to 4 cutters, however, depending on the number of cutters, the feed changes by almost 2 times. Figures 3 (b, c, d) show feed changes (with different instability of the technological system): for a rougher workpiece (b), when the setup is transferred to machines with increased accuracy (c), with the simultaneous influence of both previous factors (d). On the right of each version, the effectiveness of the influence of these factors is shown. Such roughening of the workpiece to ITZ13 requires a feed reduction of up to 36%, transfer to machines with increased accuracy allows you to increase the feed by 20 - 91%.

Figures 1 - 3 describe the machining of a piece workpiece, when each tool has its own initial surface in the workpiece with its own ITZ grade (in accordance with the scheme of Fig. 3.7 [2]). Such machining is used on semi-automatic lathes. On lathes, the workpiece is a bar, and therefore, a group of turning cutters often works according to a different scheme - the previous cutter forms the initial surface for the next one.

In this case, fluctuations in the depth of cut will appear only in the first tool of the setting, while the remaining factors of the scattering field - stiffness fluctuations Δj and hardness fluctuations v - appear on all tools of the setting. The developed models make it possible to calculate this scheme as well.

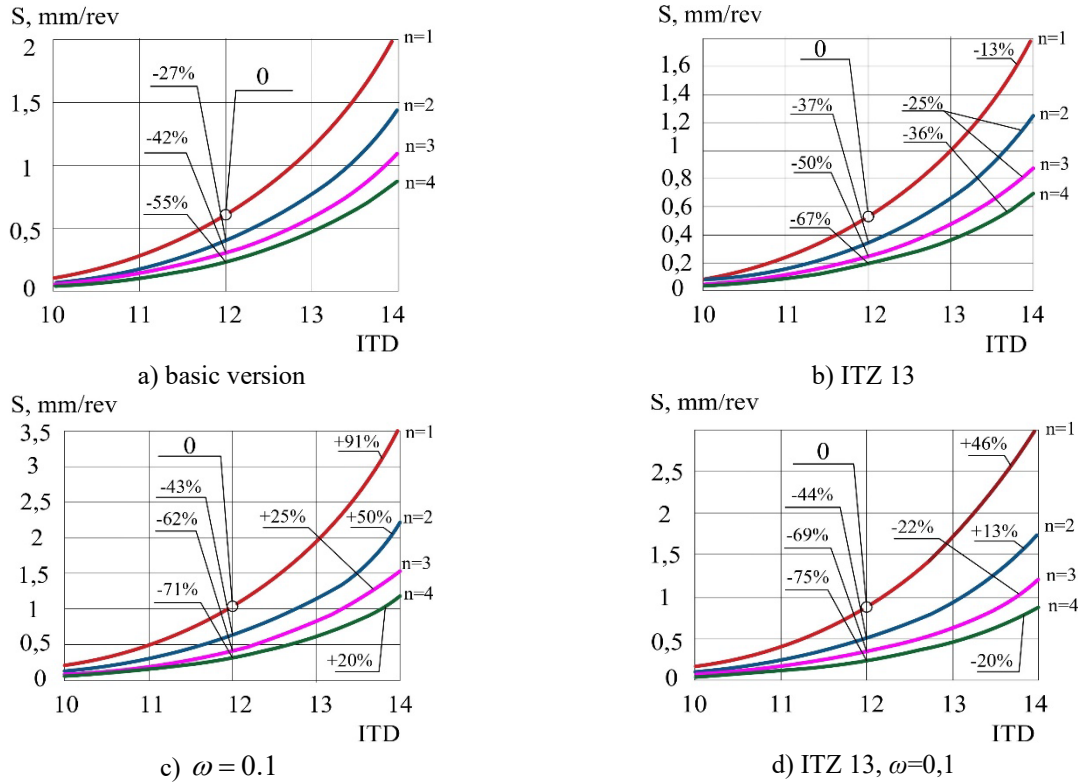


Figure 3. Influence of dimensional accuracy on feed in multi-tool single-carriage machining. Basic version: workpiece – stamping, Steel 45, precision of every surface ITZ12; tools – turning cutters (n -number) P6M5, $\varphi = 60^\circ$, $\gamma = 15^\circ$, $r = 2\text{mm}$; instability of the technological system $\omega = 0.2$; total depth of cut $t = 6\text{ mm}$. Changes are indicated for other versions.

Figure 4 shows a comparison of the limit feeds for the case of machining a piece workpiece according to the scheme shown in Figure 3.7 [2] and for a workpiece from a bar according to the scheme described above.

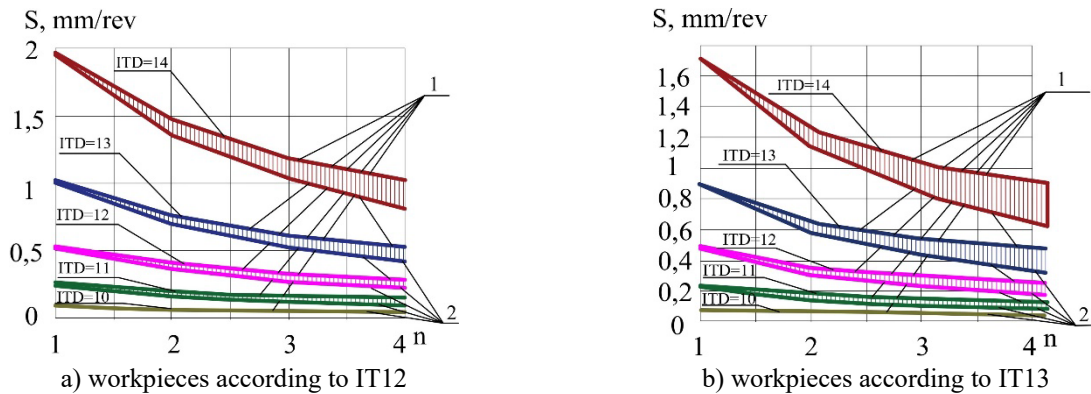


Figure 4. Comparison of feed accuracy limits for multi-tool single-carriage adjustments (4 turning cutters, other conditions according to Fig. 6.13): 1) workpiece - bar, (the first cutter forms the initial surface for the second, and so on.); 2) piece workpiece (adjustment on Fig. 3.7 [2])

As can be seen from fig. 4, machining according to the scheme, when the previous cutter forms the initial surface for the next one, allows us to increase the feed. Moreover, this increase strongly depends on the accuracy of the performed dimension and the error of the workpiece.

Comparison of graphs in fig. 1 - 3 with normative recommendations [13] shows their good convergence (within 15%).

Conclusion. A matrix generalization of feed control models by the criterion of accuracy of the

performed dimension for multi-tool single-carriage machining has been developed. Control models make it possible to calculate the maximum permissible cutting conditions in terms of machining accuracy.

REFERENCES

- [1]. Yusubov, N.D. *Fundamentals of matrix theory of accuracy of multi-tool turning. (Principles and structure of the theory, design and management of multi-tool machining processes)*. AV Akademikerverlag GmbH & Co. KG / LAP LAMBERT Academic Publishing, Saarbrücken, 2013.
- [2]. Yusubov, N.D. *Multi-tool machining on automatic lathes (Matrix theory of multi-tool machining accuracy on modern CNC lathes)*. AV Akademikerverlag GmbH & Co. KG / LAP LAMBERT Academic Publishing, Saarbrücken, 2013.
- [3]. Yusubov, N.D., Abbasova, H.M. *Models for Machining Accuracy in Multi-Tool Adjustment*. International Journal of Automotive and Mechanical Engineering, 2020, vol. 17, no. 3, pp. 8067-8085. <https://doi.org/10.15282/ijame.17.3.2020.01.0605>
- [4]. Koshin, A.A., Yusubov, N.D. *Elements of matrix theory of multitool processing accuracy in three-dimensional setups*. Bulletin of mechanical engineering, 2013, no. 9, pp. 13-17.
- [5]. Yusubov, N.D., Abbasova, H.M. *Full-factor matrix model of accuracy of dimensions performed on multi-purpose CNC machines*. Obrabotka metallov (tekhnologiya, oborudovanie, instrumenty) = Metal Working and Material Science, 2021, vol. 23, no. 4, pp. 6-20.
<https://doi.org/10.17212/1994-6309-2021-23.4-6-20>
- [6]. Yusubov N., Abbasova, H., Khankishiyev, İ. *Entwicklung einer Projektierungstheorie für die Mehr-werkzeugbearbeitung mit den Möglichkeiten der modernen CNC-Werkzeugmaschinen*. Forschung im Ingenieurwesen, 2021, no. 85, pp. 661-678.
<https://doi.org/10.1007/s10010-021-00478-7>
- [7]. Yusubov, N.D. *Matrix models of working accuracy at single-cutter turning*. Tekhnologiya Mashinostroeniya, 2009, no. 1, pp. 41-45.
- [8]. Liu, C, Li, Y, Hua, J, Lu, N, Mou, W. *Real-time cutting tool state recognition approach based on machining features in NC machining process of complex structural part*. International Journal of Advanced Manufacturing Technology, 2018, vol. 97, pp. 229-241.
<https://doi.org/10.1007/s00170-018-1916-y>
- [9]. Kuram, E., Ozcelik, B., Bayramoglu, M., Demirbas, E., Simsek, B.T. *Optimization of cutting fluids and cutting parameters during end milling by using D-optimal design of experiments*. Journal of Cleaner Production, 2013, vol. 42, pp. 159-166.
<https://doi.org/10.1016/j.jclepro.2012.11.003>
- [10]. Chung, C., Wang, P.C., Chinomona, B. *Optimization of turning parameters based on tool wear and machining cost for various parts*. Journal of Advanced Manufacturing Technology, 2022, vol.120, pp. 5163-5174. <https://doi.org/10.1007/s00170-022-09037-y>
- [11]. Azvar, M., Budak, E. *Multi-dimensional chatter stability for enhanced productivity in different parallelturning strategies*. International Journal of Machine Tools and Manufacture, 2017, vol. 123, pp. 116-128. <https://doi.org/10.1016/j.ijmactools.2017.08.005>
- [12]. Dalsky, A., Kosilova, A., Mesheryakova, R., Suslova, A. *Handbook of a mechanical engineering*. in 2 volumes. T.I. Mechanical engineering, Moscow, 2003.
- [13]. Korchak, S.N., Koshin, A.A., Shalamova, I.A. etc. *General machine-building standards for cutting conditions, wear rates and consumption of tools for horizontal bar lathes*. Research Institute of Mechanical Engineering (NIIMash), Moscow, 1983.

Received: 16.02.2023

Accepted: 02.05.2023



INVESTIGATION OF WEAR-RESISTANT MATERIALS WORKING UNDER SHOCK-ABRASIVE WEAR CONDITIONS AND TEST CONDITIONS

Subhan NAMAZOV¹, Taleh TAGHIYEV^{2*}, Shahin MASHAYEV³

¹Vice-rector for science and innovation of Azerbaijan Technical University, Baku, Azerbaijan

^{2,3}Department of metallurgy and materials technology, Azerbaijan Technical University, Baku, Azerbaijan

E-mail: subhan_namazov@daad-alumni.de¹, tagiyev-taleh@mail.ru^{2*}, mashayevshahin@gmail.com³

Abstract: During operation, static and dynamic loads, as well as various types of friction and wear, can simultaneously act on parts of machines and mechanisms. In these cases, as a rule, the problem of ensuring the wear resistance of parts is secondary, since, first of all, it is necessary to give structural elements strength, to exclude destruction and crushing. However, for a more significant increase in the service life of parts, it is necessary to apply comprehensive measures that allow solving these problems together. The mechanism of impact-abrasive wear of materials is primarily determined by their chemical composition and structure. A study of the nature of wear of hardened iron-carbon rolled steels shows that with a change in carbon concentration, the mechanism of impact-abrasive wear also changes. With an increase in the carbon content, the hardness of the metal increases, the depth of the holes from the introduction of the abrasive gradually decreases, however, the wear changes according to a more complex relationship: it decreases with an increase in the carbon concentration to 0.7 + 0.8%, and with a higher content, it increases.

Keywords: *structure, carbon, shock-abrasive, composition, material, sintering, wear resistance.*

Introduction. Wear to eutectoid steels, which have relatively low hardness and sufficient ductility, occurs as a result of repeated introduction of the abrasive into the surface, which causes the accumulation of plastic deformation (hardening of the metal), its hardening, and the separation of local fragments from the surface. With an increase in the carbon content, the plastic properties of steels decrease, and impact-abrasive wear occurs due to brittle chipping of metal particles [1].

The authors of [1] in the study of wear of steels 45, Y7, Y8, Y12 showed that in order to increase wear resistance, the carbon content should be selected taking into account external force conditions of influence: dimensions, hardness and thickness of the layer of abrasive particles, speed and impact energy at the contact, as well as sample shapes.

The relationship between the mechanical properties of compact steels and their impact-abrasive wear resistance was studied in detail in [1]. When studying the influence of the mechanical properties of steel 45 and Д7XBHIII on impact-abrasive wear resistance, it was found that hardness, impact strength, relative elongation and relative narrowing do not have an unambiguous relationship with wear intensity. Various mechanisms of impact-abrasive wear in the ductile and brittle regions (separation of which was carried out according to the orientation of the fracture site of the samples! at central bending) were revealed. It has been established that in the brittle region of fracture with an increase in hardness, a decrease in ductility and impact toughness, the wear resistance of steel increases, and in the ductile region an inverse relationship is observed. Samples with a structure corresponding to the transition from the ductile nature of fracture to fragile.

Similar results were obtained in the study of shock-abrasive wear of the surfacing material of the Fe-C-Cr system. A different nature of the influence of the mechanical properties of steels of pearlitic and austenitic classes on impact-abrasive wear resistance is noted. For austenitic steel 110Г and 13Ж, the change in impact strength, relative narrowing and elongation does not significantly affect wear resistance, and the tensile strength has a direct relationship with wear.

The well-known principle of increasing the wear resistance of steels and alloys when sliding over an abrasive by creating an austenitic-martensitic structure was applied to materials subject to

Subhan NAMAZOV , Taleh TAGHIYEV, Shahin MASHAYEV
Investigation of wear-resistant materials working under shock-abrasive wear
conditions and test conditions

impact-abrasive wear.

When testing powder materials according to the specified method, it is possible to reduce the accuracy of the results due to the residual porosity in the samples. In the process of washing, it is possible to get washing liquids into the open pores, which can remain in them after drying and increase the real mass of the samples. It is also necessary to correct the processing modes, as porous metals can be compacted under by the action of loads.

Taghiyev and Gahramanov found that one of the priority areas for the development of wear-resistant surfacing to the conditions of shock-abrasive wear is the creation of an austenitic-martensitic structure in the Fe-C-Cr-Ni and Fe-C-Cr-Mn systems with the addition of molybdenum, tungsten and vanadium carbides [2]. During tests with high impact energy (more than 25 J), a part of the austenite is transformed into deformation martensite, which has greater hardness and strength, which ensures an increase in wear resistance.

Iron-based alloys containing 1.2-4.8% carbon, 5-45% chromium, 1% nickel, 2% vanadium with a structure of austenite, martensite, vanadium carbide and various modifications of chromium carbides according to grain edges [2].

Product assemblability analysis. When studying the impact-abrasive wear of a surfacing alloy based on Fe-C-Mn, it was found that surfacings that are on the border of ductile and brittle fracture have the best wear resistance: for example, an alloy of eutectoid composition with a content of 6-8% manganese with -martensitic structure [3].

The highest wear resistance was observed in alloys with a carbon content of 0.55-4.19%, chromium 8-42% and boron about 2.5%. With an increase in the chromium content, the wear increased due to the formation of an excess ferrite phase, which reduces the hardness of the deposit to 45-48 HRC. The hardness of the tested alloys was 50-35 HRC. Also in this work it is shown that for the study of impact-abrasive wear, it is necessary to use special test equipment, since the properties of materials do not have sufficient correlation with impact-abrasive wear resistance.

The effect of volumetric reinforcement of compact alloyed steels is considered in detail in [4], where it is substantiated that in unstable austenitic steels with a high carbon content and moderate kinetics of martensitic transformation during shock-abrasive wear, 30-40% of deformation martensite is formed, which strengthens significant volumes of material. The developed steel 70X5Г9ΦTM is recommended for the production of rock cutting tool parts.

In [5], the influence of heat treatment parameters on the impact-abrasive wear of white cast irons containing 19–21% chromium was studied. In the cast state, such materials have low wear resistance. The use of hardening and tempering can significantly reduce weight loss. It is shown that under the action of impact-abrasive wear, phase transformations occur in the cast iron structure, redistribution of alloying elements due to the decay of residual austenite. There is also an increase in the microhardness of the decomposition products and the overall hardness of the test surface of the samples. The best combination of properties had cast iron containing 21% chromium, the austenization of which took place at a temperature of 950°C for 1.5 hours.

The only mention of the impact-abrasive wear resistance of hard alloys is given in [6]. In comparative tests of alloys of the BK3, BK4, BK4-B, BK6, BK6-B and BK8 series, it was found that these materials had wear resistance 2-8 times less than steel 45 with a hardness of 52 HRC

Analyzing the results of the presented works, we can conclude that the issues related to the impact-abrasive wear of powder steels are not covered enough. From the analysis carried out, it was found that the impact-abrasive wear resistance of steels and alloys is determined mainly by the strength properties of the surface layer. Since the residual porosity of powder steels and alloys contributes to a decrease in strength, both on the surface and in the entire volume of the material [7, 8], it is possible that sintered steels will have low wear resistance under shock-abrasive wear. In addition, in porous materials, the effect of caricaturing by abrasive particles is possible, which was revealed when sliding over an abrasive in works [9].

Subhan NAMAZOV, Taleh TAGHIYEV, Shahin MASHAYEV
Investigation of wear-resistant materials working under shock-abrasive wear conditions
and test conditions

Thus, based on a review of the studies performed on the influence of various factors on the impact-abrasive wear resistance of steels and alloys, we can propose the following ways to create powder steels that are resistant to fracture under such conditions.

For the selection of washing liquids and the drying time, the sintered samples made of ПЖБ 3.160.26 powder with a final porosity of 5 and 35% were washed with gasoline brand "Premium-95" according to ГОСТ 51105-97 and technical acetone of the 1st grade (ГОСТ 2768-84) during 30 sec. Then the samples were wiped with a filter-napkin, weighed for 1 min, and then every 5 min.

The remaining fraction of liquid (C_m) in the powder was calculated according to the formula (1) [8]:

$$C_m = \frac{m_2 - m_1}{m_2} \cdot 100\% \quad (1)$$

Where, m_2 - is the mass of the sample after washing, m_1 - sample mass before washing
 Based on the calculated data, the dependence was built (1).

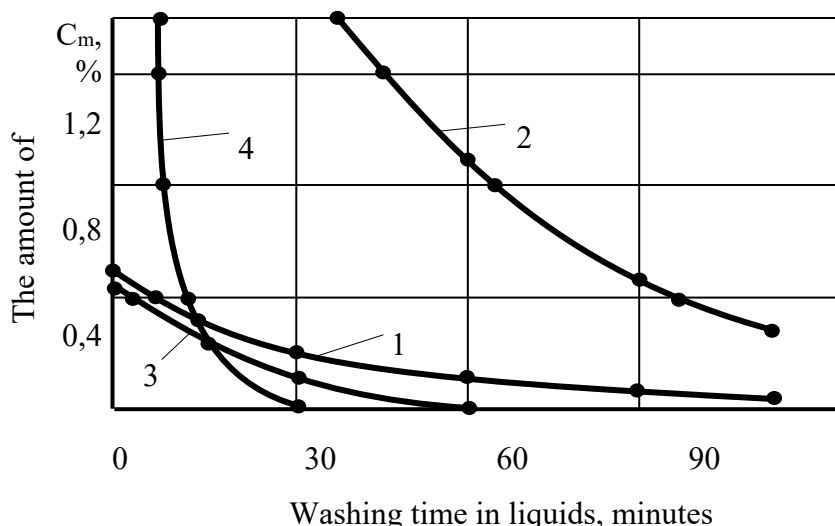


Figure 1. Dependency residual share gasoline (1.2) and acetone (3.4) in samples with residual porosity, %:

As can be seen from fig. 1 the amount of absorbed liquid and the intensity of its evaporation from the surface of the samples is proportional to their residual porosity. For example, after 2 min. After drying, samples with a residual porosity of 35% contained more than 3% C_m , and with a porosity of 5% - about 0.45%. After 120 min. drying samples with a porosity of 5% contained up to 0.1% gasoline, with $P = 35\%$ more than 0.4%) C_m . In all cases, acetone evaporated from the surface of the samples more intensively, complete evaporation took place within 1 hour.

In the works of Xarlamov Y.A. and Sidorov S.A. [1,3] it is noted that the duration of the stage of formation of a characteristic relief from impact-abrasive action is determined by many factors. Since porous powder materials can be compacted under the action of external loads, it is necessary to optimize the running-in conditions when testing for impact-abrasive wear resistance. The effect of the test duration on the wear rate was studied on samples with different hardness from sintered steel ЖГр-1-6,6 with a carbon content of 0.8% and rolled steel 45.

Wear of samples from rolled steel 45 with different hardness systematically decreases in the first 300÷400 strokes and then the wear rate stabilizes (Fig.2). At the initial stage (up to 200 impacts), the powder steel specimens showed an increase in wear, and then a decrease. A constant wear rate of sintered specimens was observed after 600÷900 impacts.

The increase in the intensity of the wear of powder samples at the beginning of the test is

Subhan NAMAZOV , Taleh TAGHIYEV, Shahin MASHAYEV
Investigation of wear-resistant materials working under shock-abrasive wear
conditions and test conditions

connected with the compaction processes. Under the action of shock loads, the flattening of the sample and the chipping of material particles along the perimeter of the wear surface occur (Fig. 3.).

To evaluate the performance of the developed installation, samples were prepared from steel bar 45 and sintered blanks from ПЖР 3.160.26 iron powder with the addition of 1% (wt.) carbon to the charge. Samples made of steel 45 were subjected to heat treatment (quenching at 840°C in water and low tempering at 200°C), and for the production of powder samples, the charge was pressed in a cylindrical press at a pressure of 600 MPa, after which the pressings were sintered in a protective environment at 1150°C in the course of 2 h.

Table 1. Pre-test and post-test hardness of samples

№	Sample material	Type of heat treatment	Hardness before test	Hardness after test
1	Stell 45 (СТ45)	Annealing	160÷165 HRB	230÷240 HRB
2	ЖГр1-6,6 (PA-ZhGrTSs 1-6,6)	After sintering	132÷168 HRB	241÷283 HRB
3	Stell 45 (СТ45)	Quenching and low tempering at 200°C	51÷53 HRC	54÷55 HRC
4	ЖГр1-6,6 (PA-ZhGrTSs 1-6,6)	Quenching and low tempering at 200°C	42÷54 HRC	51÷56 HRC

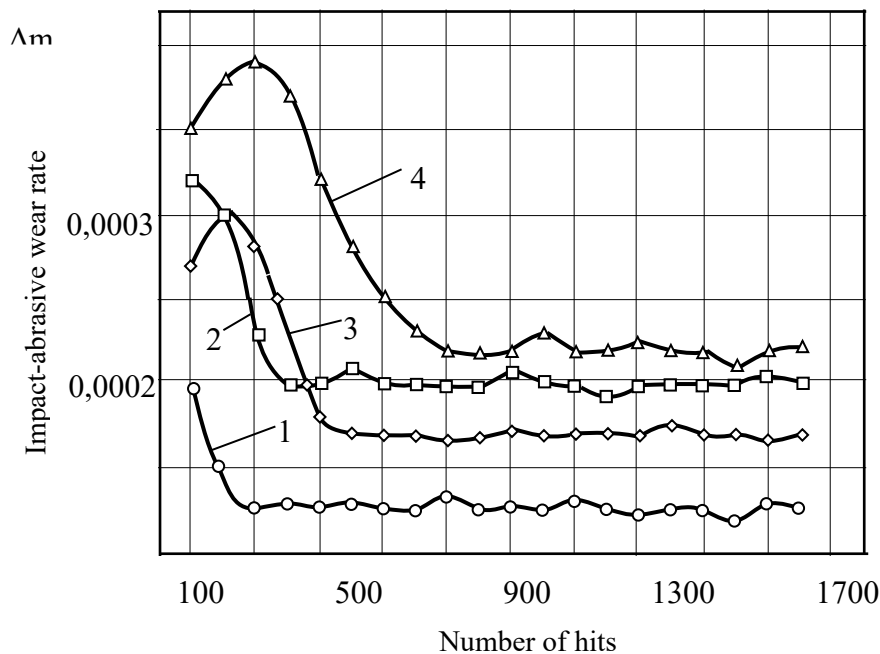


Figure 2. Dependence of the speed of shock-abrasive wear of samples on the duration of the test: 1- steel 45 (hardening + tempering); 2- steel 45 (after annealing); 3-ЖГр1 (forging+release); 4- ЖГр1 after sintering

In addition, an increase in wear with an increase in the content of graphite is apparently associated with the formation of additional pores in places where graphite was located, which actively dissolved in austenite during sintering. The high porosity of the samples intensifies the

Subhan NAMAZOV, Taleh TAGHIYEV, Shahin MASHAYEV
Investigation of wear-resistant materials working under shock-abrasive wear conditions
and test conditions

formation of cracks and the separation of dispersed particles from the wear surface. in which it is shown. That with a high content of graphite during sintering, it is intensively dissolved in iron, which causes the formation of additional pores, a decrease in strength, toughness and wear resistance of powder steel.

The decrease in the size of the holes on the surface of the samples with a high carbon content is associated with a change in the wear mechanism. It is known that with an increase in the carbon content in the steel, the hardness increases and the plastic properties deteriorate; therefore, the wear of the samples occurs mainly due to the brittle chipping of the solid structural components.

On fig. 4 shows the dependence of shock-abrasive wear and absolute deformation of the samples on the impact energy. For testing, springs with a stiffness of 0.8 and 1.65 N/mm were used, and combinations of them made it possible to provide an impact energy from 3 to 27.9 J.

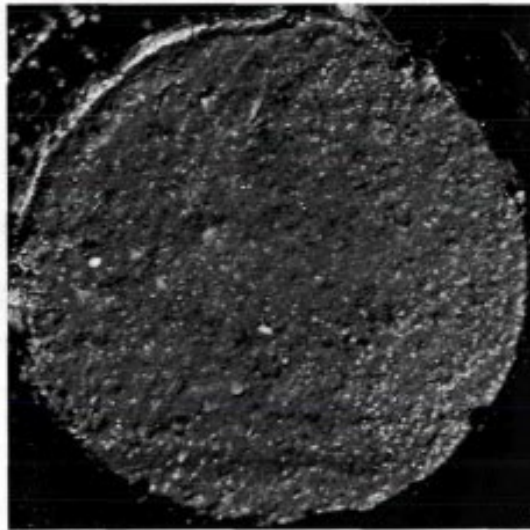


Figure 3. Macrorelief of the surface of the powder steel sample after shock-abrasive wear

Quartz sand with a particle size ranging from 0.1 to 0.63 mm was used as an abrasive. The samples were run-in in 500 strokes and wear in 100C strokes. Wear was defined as the difference between the weight of the samples after running in and testing.

With an increase in impact energy from 3 to 18 ÷ 19 J, the wear of samples made of steel 45 increased to 0.008 g and then changed slightly (Fig. 3.4, curve 1). At an impact energy of more than 24÷25 J, the mass loss again increases due to sample deformation. For powder samples, with an increase in impact energy from 3 to 6 J, wear decreases to 0.02 ÷ 0.022 g (Fig. 4, curve 2) as a result of sample compaction and hardening of the matrix. With a further increase in the impact energy from 6 to 24 J, the mass loss reaches 0.05 g, while the end of the sample is flattened and the edges are destroyed. The absolute deformation of powder samples increases monotonically from 0.07 to 0.6 mm with an increase in impact energy from 3 to 24.6 J. The residual deformation of steel 45 was no more than 0.1–0.13 mm.

The study of impact-hydroabrasive wear (Fig. 5) was carried out at an impact energy of 3 and 6.3 J, for which springs with stiffness of 0.8 and 1.65 N/mm were used. Changing the impact speed was carried out by installing additional loads (4.3; 8.6; 12.9 kg) on the impactor (impactor mass 4.3 kg). Impacts were carried out through a mixture consisting of quartz sand with a particle size of 0.1 to 0.63 mm and water. The mass fraction of sand in the mixture was 70%.

An increase in the impact speed from 0.7 to 1.8 m/s ($E_{ud} = 3$ J) leads to an increase in the wear of the steel 45 sample to 0.05 g, and the powder sample to 0.09 g.

Subhan NAMAZOV , Taleh TAGHIYEV, Shahin MASHAYEV
Investigation of wear-resistant materials working under shock-abrasive wear
conditions and test conditions

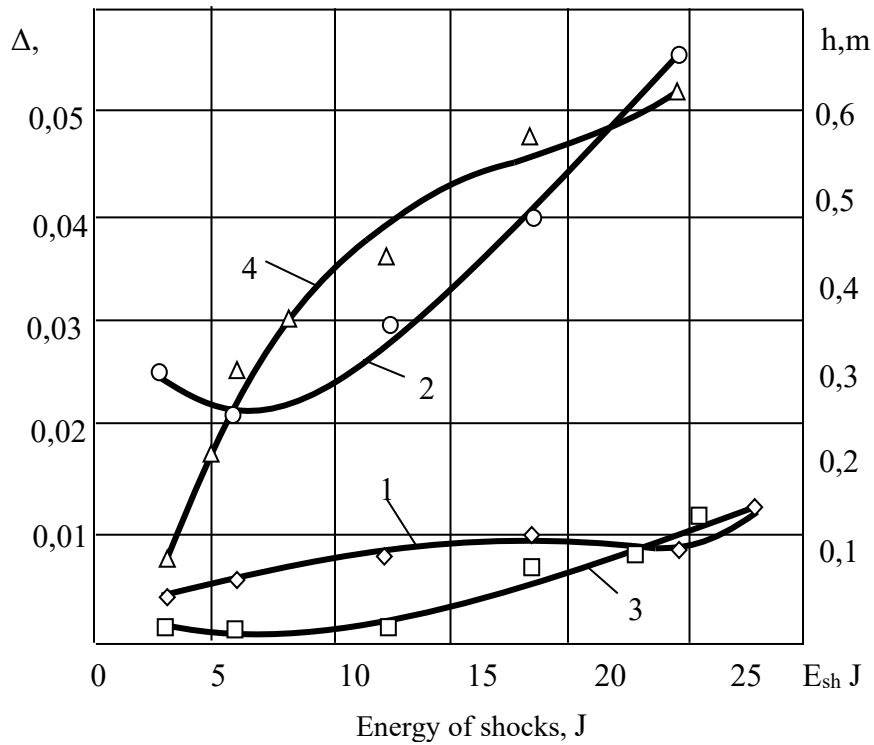


Figure. 4. Dependence of wear (1.2) and absolute deformation of samples (3.4) on impact energy during shock-abrasive wear: 1.3 - steel 45; 2.4 - ПЖГр1

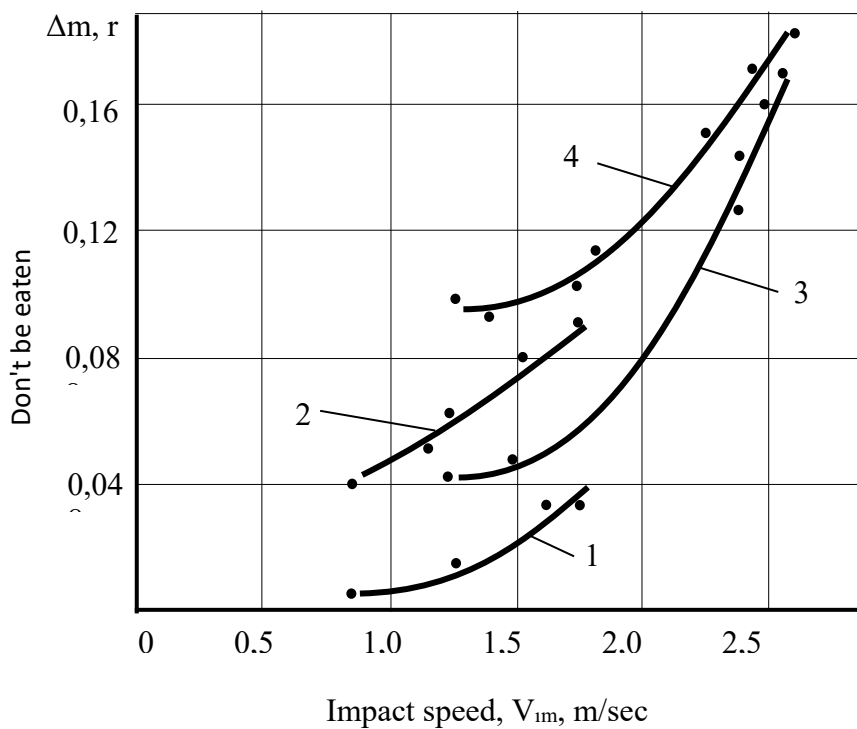


Figure. 5. Dependence of wear of steel 45 (1.3) and powder material ПЖГр1 (2.4) on impact velocity V_{im} at impact energy E_{im} , J: 1.2-3; 3.4-6.3

Subhan NAMAZOV, Taleh TAGHIYEV, Shahin MASHAYEV
Investigation of wear-resistant materials working under shock-abrasive wear conditions
and test conditions

At the impact energy of 6.3 J, the change in speed from 1.3 to 1.9 m/s also slightly increases the wear of materials, for example, steel 45 from 0.046 to 0.06 g, and powder from 0.092 to 0.11 g. The further increase in the impact speed intensifies the loss of mass of the samples, which at 2.6 m/s for steel 45 is 0.17 g and powder-0.19.

It is established that the degree of wear of materials during shock-hydroabrasive wear is higher than during shock-abrasive wear (Fig. 4-5). This is explained by the fact that during shock-hydroabrasive wear, not only direct penetration of abrasive particles into the matrix occurs, as with shock-abrasive, but also their relative movement.

The compressed hydroabrasive mixture is pushed out of the collision zone and causes additional wear by microcutting. Such a wear mechanism agrees with the results of the work [5]. It is also established that when V_{ud} and E_{ud} are constant, the ratio of the amount of wear during shock-abrasive wear to Δm during shock-hydroabrasive wear is constant. Therefore, in the following experiments, only the shock-abrasive wear resistance of powder steels is investigated.

Thus, it is shown that to obtain reliable test results, it is necessary to take into account the physical and mechanical properties of powder steels. According to the results of the conducted research, it was established that for washing samples of porous metals, it is expedient to use acetone as a washing liquid, and at the stage of drying, the samples should be kept for at least 1 hour. The stage of processing samples from sintered steel should consist of no less than 1000 blows.

Conclusion. Increasing the strength, toughness and ductility of the matrix of powdered iron-carbon steels through the use of alloying additives. Ensuring a uniform distribution of alloying additives in steels with a given structure. Increasing the strength of powder steel by reducing residual porosity using various methods of pressure treatment of sintered billets. It has been experimentally established that powder steels containing 0.8÷1.0% carbon, 3.5÷4% chromium and 4÷5% nickel, which are evenly distributed in the matrix, have good wear resistance. When hardening powder steel with chromium carbides, the impact-abrasive wear resistance decreases due to the cracking of hard structural components. In powder steels, during shock-abrasive wear, pores are stress concentrators that contribute to the formation and propagation of cracks. Experiments have shown that the wear of materials decreases with the decrease of the final porosity according to the exponential dependence.

REFERENCES

- [1]. Geng, Z., Puhan, D., Reddyhoff, T. *Using Acoustic Emission to Characterize Friction and Wear in Dry Sliding Steel Contacts*. Tribology International, 2019 vol. 134, pp. 394-407.
- [2]. Taghiyev, T.A., Kahramanov, V.F. *Investigation of the effect of chemical composition on corrosion resistance of parts made of rub steels*. Engineering Mechanics, 2020, N1, pp. 42–48.
- [3]. Golubina, S.A. Sidorov, V.N. *Development of methods for increasing the technical and economic efficiency of the application of hardening technologies for flat working bodies of tillage machines*. International conference on modern trends in manufacturing technologies and equipment, ICMTMTE, 2020, pp. 52-54
- [4]. Samah A. Al-Shelkamy, H. M. Abu Hashish and Amir A. Mahdy. *Structural and Tribological Properties of Heat-Treated Stainless Steels against Abrasive and Lubricant Wear Conditions*. Coatings, 2021, V. 11, No 1473, pp 1-18.
- [5]. Siekaniec, D., Kopycinski, D., Tyrała, E., Guzik E., and Szczesny, A., *Optimisation of Solidification Structure and Properties of Hypoeutectic Chromium Cast Iron*. Materials, 2022, 15, 6243, pp. 2-19.

Subhan NAMAZOV , Taleh TAGHIYEV, Shahin MASHAYEV
Investigation of wear-resistant materials working under shock-abrasive wear
conditions and test conditions

- [6]. Ugur Ulusoy. *Review of Particle Shape Effects on Material Properties for Various Engineering Applications: From Macro to Nanoscale*. Minerals, 2023, Vo 13, No. 91, pp. 1-81
- [7]. Mikhail, A.I., Levinsky, Y.V. and others. *Metal powders. Products from metal powders*. 2021, Moscow, 560 p.
- [8]. J. W. Martin. *Materials for engineering*. 2020, Cambridge, WOODHEAD PUBLISHING LIMITED, 269 p.
- [9]. Emre BEŞTEK. *Powder metallurgy*. Materials and Manufacturing Technologies, Bahcesehir University, 2020, 2 p.

Received: 21.04.2023

Accepted: 29.05.2023



MATHEMATICAL MODELS OF CUTTING FORCES IN TURNING OPERATIONS

Viktor GUZEEV¹, Igor DERYABIN², Dmitrii ARDASHEV^{3*}

^{1,2,3*}South Ural State University, Chelyabinsk, Russia

E-mail: guzeevvi@susu.ru¹, deriabini@susu.ru², ardashevdi@susu.ru^{3*}

Abstract: The paper considers a variant of the predictive determination of the cutting force components for non-free cutting when turning. It is established that both the process of plastic deformation and the process of friction on back surfaces adjacent to main and auxiliary cutting edges of the tool influence the magnitude and direction of a cutting force component. The resulting force is defined as the vector sum of the forces that occur on the main and auxiliary cutting edges. We propose to determine the cutting force direction in non-free cutting as a vector in the direction of chip flow relative to the main cutting edge. The cutting process photography fixes the inclination angle of the chip flow. It is confirmed that in free cutting, the direction of chip flow is perpendicular to the main cutting edge. Contour turning on CNC lathes is accompanied by a change in the direction of feed motion resulting in a change in the main and auxiliary kinematic angles of the cutting tool. An increase in the active length of the main cutting edge in this situation leads to an increase in the contact area of the back surface of the main cutting edge with the workpiece surface, and, consequently, to an increase in the friction component of force, acting on the main cutting edge. Experimental measurement of the cutting force components makes it possible to determine the degree of influence of the force components associated with both the process of plastic deformation of the work material and the process of friction on the back surfaces adjacent to the main and auxiliary cutting edges of the tool. The obtained analytical dependences express the functional relationship between the elements of the cutting modes, the geometric parameters of the cutters, the degree of wear, the shape of the workpiece surface, and physical and mechanical properties of the work material. A large set of parameters included in the formulas for determining the components of the cutting force allows adequate monitoring the nature of the force interaction of the elements in the technological system when processing parts.

Keywords: *cutting forces, contour turning, unstable force load on technological system*

Introduction.

Despite the short terms of technological preparation for multi-product manufacturing, technological solutions must ensure the accuracy of the manufactured parts and the specified productivity. The difficulty of fulfilling these parameters is often associated with such a feature of a technological system as the technological heredity of part errors from workpiece errors. The workpiece refinement factor is mainly determined by the magnitude of the forces acting in the cutting process and the stiffness of the technological system. Under these conditions, the predictive determination of cutting forces becomes a primary task in making technological decisions. When choosing a cutting tool and assigning cutting conditions, it is necessary to evaluate the workability of the workpiece material. Its value is related to cutting forces [1, 2]. When determining the optimal cutting conditions, one of the main limitations is the cutting forces [3, 4]. Experimental determination of cutting forces is very time-consuming [5 - 12]. Analytical models are of greater interest [13 - 16]. Many researchers have studied the effect of specific parameters of the cutting process on cutting forces [17 - 21]. To predict cutting forces when contour turning on CNC lathes, multifactor models are required that take into account variable cutting conditions.

Under the unsteady conditions, a significant part of the resulting errors is the dimension errors in the dynamic adjustment. To predict these errors, it is necessary to evaluate the cutting forces under conditions of multiaxis movement of the cutting tool. Cutting forces with sufficient practical accuracy can be determined based on considering the elementary components of the cutting force acting on an infinitely small section of the cutting tool edge. This approach makes it possible to build a universal mathematical model of the cutting force that is invariant to different types of processing [22].

Methods and results

Knowing the magnitude of the force acting on the elementary sections of the active part of the tool cutting edges, it is possible by integrating to determine the components of the cutting force for all processing conditions, both simple surfaces with generatrices located parallel to the machine coordinate axes and complex surfaces arbitrarily located in the machine coordinate system.

The magnitude and direction of the components of the cutting force that occurs during non-free cutting depends on the forces on the face and back surfaces of both the main and auxiliary cutting edges. The resulting force can be found as a vector sum of forces that occur on the main and auxiliary cutting edges.

$$\bar{P}_{xy} = \bar{P}_{xy(d)}^{main} + \bar{P}_{xy(fr)}^{main} + \bar{P}_{xy(d)}^{aux} + \bar{P}_{xy(fr)}^{aux}, \quad (1)$$

where $\bar{P}_{xy(d)}^{main}$ and $\bar{P}_{xy(d)}^{aux}$ are forces arising on the face surface of the main and auxiliary cutting edges; $\bar{P}_{xy(fr)}^{main}$ and $\bar{P}_{xy(fr)}^{aux}$ are forces arising on the back surface of the main and auxiliary cutting edges.

According to (1), the magnitude and direction of the cutting force radial-axial component depends on both the magnitude and the direction of the forces acting on the main and auxiliary cutting edges.

Let us analyze the significance of each of the components of (1) under the conditions of processing complex-profile surfaces with a variable direction of feed movement.

In the theory of metal cutting, there are no methods for analytically determining the influence of the feed movement direction on the direction of forces arising on the face surface of the main cutting edge, so this relationship was verified experimentally. Considering that the direction of the radial-axial component of the cutting force on the face surface of the cutter coincides with the direction of chip flow or differs from it by some constant value, the change in the direction of this force can be inferred by the direction of chip flow.

To fix the direction of chip flow during processing with different feed directions, we made experiments on photographing the cutting process. In order to eliminate the influence of forces on the auxiliary cutting edge on the direction of chip flow, processing was carried out under free cutting conditions. Measurements of chip flow angles along the face surface showed that the direction of chip flow does not change depending on the feed direction (Fig. 1).

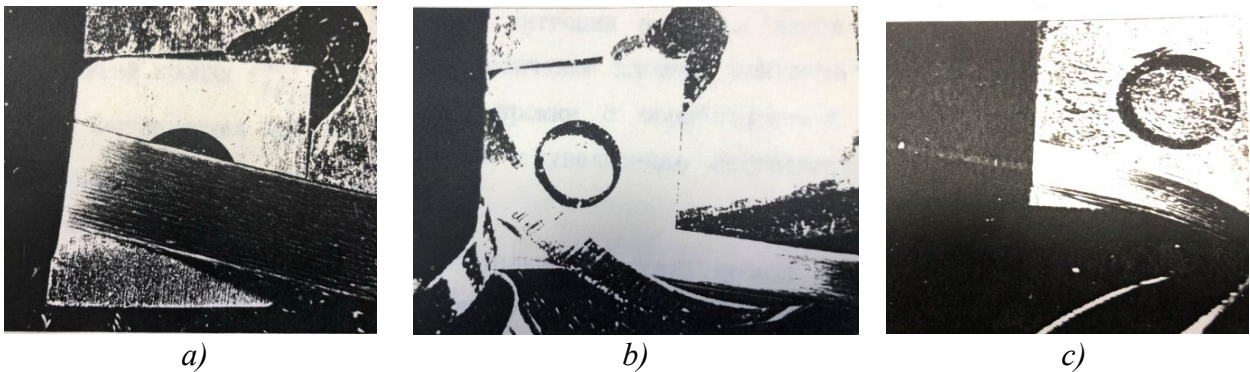


Figure. 1. Photos of chip flow along the face surface in free cutting conditions at different inclination angles of the workpiece generatrix: a) $\omega = 10^\circ$; b) $\omega = 30^\circ$; c) $\omega = 60^\circ$.

Considering that the direction of the cutting force P_{xy} component is directly related to the direction of chip flow, we can conclude that the direction of the P_{xy} component in free cutting does not depend on the direction of feed movement. Therefore, a change in the direction of feed when turning a contoured surface does not cause an inclination of the axial P_x and radial P_y components of the cutting force in free cutting conditions.

When turning contoured surfaces with a constant contour feed, with a decrease in the main kinematic approach angle φ_k , the width of cut increases, but at the same time, its thickness decreases. Calculations showed that when the angle of inclination of the workpiece surface changes from 0 to 90°, the cross-sectional area changes by no more than 5%. This change can be neglected and the area of the cut can be considered constant. From this, we can conclude that the magnitude of the force $\bar{P}_{xy(d)}^{main}$ also does not depend on the angle of inclination of the treated surface.

The active length of the main cutting edge, which increases in this case, leads to an increase in the contact area of the back surface of the main cutting edge with the surface to be machined, and, consequently, to an increase in the force component $\bar{P}_{xy(fr)}^{main}$.

To determine the degree of influence of the force $\bar{P}_{xy(fr)}^{aux}$ acting on the back surface of the auxiliary cutting edge on the change in the total radial-axial component of the force P_{xy} , experiments were carried out with the simultaneous photography of the chip flow (Fig. 2) and the dynamometry of the axial P_x and radial P_y components of the cutting force.

The hypothesis of the experiment was based on the fact that forces acting on the face surface of the tool determined the inclination angle of the chip from the normal to the cutting edge while the inclination angle η_r of the radial-axial component of the cutting force P_{xy} depended on both the forces acting on the face and back surfaces. Therefore, comparing the value of the inclination angle of the chip, measured from photographs of the cutting process, with the value of the inclination angle of the force calculated from the measured components P_x and P_y using the formula:

$$\rho = \arctg \frac{P_y}{P_x} - (0,5\pi - \varphi)$$

we can conclude about the degree of $\bar{P}_{xy(fr)}^{aux}$ influence on the change of the P_{xy} component.

Table 1 shows the values of chip inclination angles obtained from photographs. Analyzing the obtained values of the angles, we see that the chip flows perpendicular to the diagonal of the cut layer. A number of researchers has already noted this fact.

Table 1. Values of chip inclination angles η_{ch}

φ_1 , grad	3	9	15	30	45	60
η_{ch} , grad	8	8.2	8.6	9	9.2	10

Table 2 presents the values of P_x and P_y cutting force components measured at different auxiliary approach angles φ_1 .

The calculated values of inclination angles of the P_{xy} force based on Table 2 are summarized in Table 3.

Table 2. Values of P_x and P_y components when machining 40X steel with cutters at different angles φ_1

φ_1 , grad	3	9	15	30	45	60
P_x , N	469.5	394.2	340.5	322.5	308.2	274.1
P_y , N	178.0	282.0	242.6	224.1	199.5	168.8

Table 3. Inclination angles η_r of the force P_{xy} at different angles φ_1

φ_1 , grad	3	9	15	30	45	60
η_r , grad	39.2	28.37	28.25	24.42	24.19	23.97

Comparing the angle values in Tables 1 and 2, we see that the inclination angles η_r of the force P_{xy} are much larger than the corresponding chip inclination angles η_{ch} . This proves that the forces on the back surface of the auxiliary cutting edge of the tool have a significant effect on the inclination of the radial-axial component of the cutting force P_{xy} .

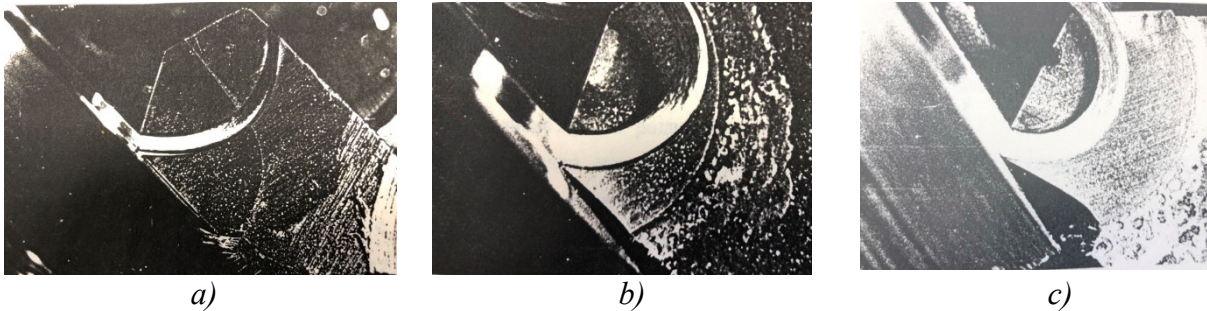


Figure. 2. Photos of chip flow in non-free cutting conditions: a) $\varphi_1 = 3^\circ$; b) $\varphi_1 = 15^\circ$; c) $\varphi_1 = 45^\circ$

Therefore, an increase in the auxiliary approach angle φ_1 leads to a decrease in the area of the cut by the auxiliary cutting edge and the area of the back surface contact with the workpiece. This causes a decrease in both components, $\bar{P}_{xy(d)}^{aux}$ and $\bar{P}_{xy(fr)}^{aux}$, of the cutting force on the auxiliary cutting edge.

The consequence of the change in forces on the auxiliary cutting edge is a change in the direction and magnitude of the P_{xy} component. Therefore, with an increase in the angle of inclination ω of the machined surface, the radial-axial component of P_{xy} can either increase if the force $\bar{P}_{xy(fr)}^{main}$ on the back surface of the main cutting edge has a dominant influence on its value, or decrease if the forces acting on the auxiliary cutting edge dominate. The radial-axial component of the cutting force P_{xy} is decomposed into radial P_y and axial P_x , which, therefore, also change during CNC contour turning. The nature of the change in P_x and P_y components depends on the static approach angles, φ and φ_1 . Thus, if the main approach angle φ is less than or equal to 90° , P_x and P_y values are:

$$\begin{aligned}\bar{P}_x &= \bar{P}_x^{main} - \bar{P}_x^{aux}; \\ \bar{P}_y &= \bar{P}_y^{main} + \bar{P}_y^{aux}.\end{aligned}$$

If the angle φ is more than 90° , P_x and P_y values are:

$$\begin{aligned}\bar{P}_x &= \bar{P}_x^{main} + \bar{P}_x^{aux}; \\ \bar{P}_y &= \bar{P}_y^{main} + \bar{P}_y^{aux}.\end{aligned}$$

The components of the cutting force are determined in accordance with the options for forming the machined surface.

In the first case, when linear cutting edges make a stock removal and form residual irregularities, the cutting force components are found by integrating the expressions that determine the forces on the surface elements of the cutting edge. As a result,

$$\begin{aligned}
 P_{xy} = & \left\{ [tg(\varphi - \eta)] \int_0^{S \cos \eta} \sigma_i \varepsilon_{li} \frac{\sin \beta}{\sqrt{3} \sin \beta_1 \cos(\beta + \beta_1)} d\varepsilon_{li} + \right. \\
 & + [tg(\varphi - \eta) + S \sin \eta] \int \frac{t \cos(\varphi - \eta)}{S \cos \eta} \frac{\sin \varphi}{\sin \varphi} \sigma_i \varepsilon_{li} \frac{\sin \beta}{\sqrt{3} \sin \beta_1 \cos(\beta + \beta_1)} d\varepsilon_{li} + \\
 & \left. + [tg(\varphi - \eta) + tg(\varphi_1 - \eta)] \int_0^{\varepsilon_1} \frac{t \cos(\varphi - \eta)}{\sin \varphi} \sigma_1 (\varepsilon_1 - \varepsilon_{li}) \frac{\sin \beta}{\sqrt{3} \sin \beta_1 \cos(\beta + \beta_1)} d\varepsilon_{li} \right\} + \\
 & + 0,16 \sigma_i \left[\frac{t(0,5\pi\rho + l_3) \cos(\varphi - \eta)}{\sin(\varphi \pm \omega)} + \frac{S(0,5\pi\rho + l'_3) \sin(\varphi \pm \omega) \cos(\varphi - \eta)}{\sin \varepsilon} \right], \quad (2)
 \end{aligned}$$

where ε_1 is a conventional width of the removed layer [22].

$$\begin{aligned}
 P_z = & \left\{ [tg(\varphi - \eta)] \int_0^{S \cos \eta} \sigma_i \varepsilon_{li} \frac{\cos \beta}{\sqrt{3} \sin \beta_1 \cos(\beta + \beta_1)} d\varepsilon_{li} + \right. \\
 & + [tg(\varphi - \eta) + S \sin \eta] \int \frac{t \cos(\varphi - \eta)}{S \cos \eta} \frac{\sin \varphi}{\sin \varphi} \sigma_i \varepsilon_{li} \frac{\cos \beta}{\sqrt{3} \sin \beta_1 \cos(\beta + \beta_1)} d\varepsilon_{li} + \\
 & \left. + [tg(\varphi - \eta) + tg(\varphi_1 - \eta)] \int_0^{\varepsilon_1} \frac{t \cos(\varphi - \eta)}{\sin \varphi} \sigma_1 (\varepsilon_1 - \varepsilon_{li}) \frac{\cos \beta}{\sqrt{3} \sin \beta_1 \cos(\beta + \beta_1)} d\varepsilon_{li} \right\} + \\
 & + 0,16 \sigma_i \mu \left[\frac{t(0,5\pi\rho + l_3)}{\sin(\varphi \pm \omega)} + \frac{S(0,5\pi\rho + l'_3) \sin(\varphi \pm \omega)}{\sin \varepsilon} \right]; \quad (3)
 \end{aligned}$$

P_x and P_y components for $\varphi \leq 90^\circ$ are:

$$\begin{aligned}
 P_x = & \sin \eta \left\{ [tg(\varphi - \eta)] + tg \eta \int_0^{S \cos \eta} \sigma_i \varepsilon_{li} \frac{\sin \beta}{\sqrt{3} \sin \beta_1 \cos(\beta + \beta_1)} d\varepsilon_{li} + \right. \\
 & + [tg(\varphi - \eta) + S \sin \eta] \int \frac{t \cos(\varphi - \eta)}{S \cos \eta} \frac{\sin \phi}{\sin \phi} \sigma_i \varepsilon_{li} \frac{\sin \beta}{\sqrt{3} \sin \beta_1 \cos(\beta + \beta_1)} d\varepsilon_{li} + \\
 & \left. + [tg(\varphi - \eta) + tg(\varphi_1 - \eta)] \int_0^{\varepsilon_1} \frac{t \cos(\varphi - \eta)}{\sin \phi} \sigma_1 (\varepsilon_1 - \varepsilon_{li}) \frac{\sin \beta}{\sqrt{3} \sin \beta_1 \cos(\beta + \beta_1)} d\varepsilon_{li} \right\}
 \end{aligned}$$

$$\begin{aligned}
 & + \left[\operatorname{tg}(\phi - \eta) + \operatorname{tg}(\phi_1 - \eta) \right] \int_0^{\epsilon_1} \frac{\sigma_1(\epsilon_1 - \epsilon_{1i})}{\frac{t \cos(\phi - \eta)}{\sin \phi}} \frac{\sin \beta}{\sqrt{3} \sin \beta_1 \cos(\beta + \beta_1)} d\epsilon_1 \left. \vphantom{\int_0^{\epsilon_1}} \right\} + \\
 & + 0,16 \sigma_i \left[\frac{t(0,5\pi\rho + l_3) \sin \phi}{\sin(\phi \pm \omega)} + \frac{S(0,5\pi\rho + l'_3) \sin(\phi \pm \omega) \sin \phi_1}{\sin \varepsilon} \right]; \quad (4)
 \end{aligned}$$

$$\begin{aligned}
 P_y = & \cos \eta \left\{ \left[\operatorname{tg}(\varphi - \eta) \right] + \operatorname{tg} \eta \int_0^{S \cos \eta} \sigma_i \epsilon_{1i} \frac{\sin \beta}{\sqrt{3} \sin \beta_1 \cos(\beta + \beta_1)} d\epsilon_1 + \right. \\
 & + \left[\operatorname{tg}(\varphi - \eta) + S \sin \eta \right] \int \frac{t \cos(\varphi - \eta)}{\sin \varphi} \frac{\sin \beta}{\sqrt{3} \sin \beta_1 \cos(\beta + \beta_1)} d\epsilon_1 + \\
 & \left. + \left[\operatorname{tg}(\varphi - \eta) + \operatorname{tg}(\varphi_1 - \eta) \right] \int_0^{\epsilon_1} \frac{\sigma_1(\epsilon_1 - \epsilon_{1i})}{\frac{t \cos(\varphi - \eta)}{\sin \varphi}} \frac{\sin \beta}{\sqrt{3} \sin \beta_1 \cos(\beta + \beta_1)} d\epsilon_1 \right\} + \\
 & + 0,16 \sigma_i \left[\frac{t(0,5\pi\rho + l_3) \cos \varphi}{\sin(\varphi \pm \omega)} + \frac{S(0,5\pi\rho + l'_3) \sin(\varphi \pm \omega) \cos \varphi_1}{\sin \varepsilon} \right]. \quad (5)
 \end{aligned}$$

In the second case, when the stock removal and the formation of residual irregularities are carried out by the radial part of cutting edges, the cutting force components are:

$$\begin{aligned}
 P_{xy} = & \left\{ \int_{\frac{r-t}{r} \pm \omega}^{0,5\pi + \phi \pm \omega} r^2 \left(1 - \frac{1-t/r}{\sin \Theta_i} \right) \sigma_i \frac{\sin \beta \cos(\Theta_i + \eta - 0,5\pi)}{\sqrt{3} \sin \beta_1 \cos(\beta + \beta_1)} d\Theta_i + \right. \\
 & \left. + \int_{0,5\pi + \phi \pm \omega}^{\arccos(0,5S/r) \pm \omega} r - S \cos \Theta_i - \sqrt{r^2 - S^2 \sin^2 \Theta_i} \frac{\sigma_i \sin \beta \cos(\Theta_i + \eta - 0,5\pi)}{\sqrt{3} \sin \beta_1 \cos(\beta + \beta_1)} d\Theta_i \right\} + \\
 & + 0,16 \int_{\frac{r-t}{r} \pm \omega}^{\arccos(0,5S/r) \pm \omega} r(0,5\pi\rho + l_3) \sigma_i [0,5\pi - \arcsin(1-t/r) +, \\
 & + \operatorname{arctg}(S/2r)] \cos(\Theta_i + \eta - 0,5\pi) d\Theta_i, \quad (6)
 \end{aligned}$$

where $\Phi = \text{arctg} \frac{\sqrt{r^2 - (r-t)^2} - S}{r-t}$; Θ_i is the current angle of contact between the cutting edge and the workpiece.

In this case, the angle η , which determines the direction of the force P_{xy} , is determined as

$$\eta = \text{arctg} \frac{t-r + [r^2 - (S/2)^2]^{0,5}}{[r^2 - (r-t)^2]^{0,5} + \left\{ r^2 - [r^2 - (S/2)^2]^{0,5} \right\}^{0,5}}.$$

$$P_z = \left\{ \int_{\frac{r-t}{r} \pm \omega}^{0,5\pi + \phi \pm \omega} r^2 \left(1 - \frac{1-t/r}{\sin \Theta_i} \right) \sigma_i \frac{\cos \beta}{\sqrt{3} \sin \beta_1 \cos(\beta + \beta_1)} d\Theta_i + \right.$$

$$\left. + \int_{0,5\pi + \phi \pm \omega}^{\arccos(0,5S/r) \pm \omega} r - S \cos \Theta_i - \sqrt{r^2 - S^2 \sin^2 \Theta_i} \frac{\sigma_i \cos \beta}{\sqrt{3} \sin \beta_1 \cos(\beta + \beta_1)} d\Theta_i \right\} +$$

$$+ 0,16r\mu(0,5\pi\rho + l_3) \sigma_i [0,5\pi - \arcsin(1 - t/r + \text{arctg}(S/2r))] . \quad (7)$$

In the third case, when the radius and linear parts of the main cutting edge perform the stock removal, and the radial parts of the cutting edges form residual irregularities, the cutting force components are determined from the expressions:

$$P_{xy} = \left\{ [\text{tg}(\varphi \pm \omega)] + \text{tg} \eta \int_0^{S \cos(\varphi - \eta)} \sigma_i \sigma_{i_1} \frac{\sin \beta \cos(\varphi - \eta)}{\sqrt{3} \sin \beta_1 \cos(\beta + \beta_1)} d\epsilon_1 + \right.$$

$$+ [tS - S^2 \sin(\varphi \pm \omega) \cos(\varphi \pm \omega)] \sigma_i \frac{\sin \beta \cos(\varphi - \eta)}{\sqrt{3} \sin \beta_1 \cos(\beta + \beta_1)} +$$

$$+ \left. \int_{0,5\pi + (\varphi \pm \omega)}^{H \pm \omega} r - \frac{r - S \sin(\varphi \pm \omega)}{\cos \Theta_i} \frac{\sigma_1 \sin \beta \cos(\Theta_i - \eta - 0,5\pi)}{\sqrt{3} \sin \beta_1 \cos(\beta + \beta_1)} d\Theta_i \right\} +$$

$$+ \int_{H \pm \omega}^{\arccos(0,5S/r) \pm \omega} r - S \cos \Theta_i - \sqrt{r^2 - S^2 \sin^2 \Theta_i} \frac{\sigma_1 \sin \beta \cos(\Theta_i - \eta - 0,5\pi)}{\sqrt{3} \sin \beta_1 \cos(\beta + \beta_1)} d\Theta_i$$

$$+ 0,16\sigma_i(0,5\pi\rho + l_3) \left[\frac{t - r(1 - \cos(\varphi \pm \omega)) \cos(\varphi - \eta)}{\cos(\varphi \pm \omega)} + \right.$$

$$\left. + r(0,5\pi - \arccos(0,5S/r)) \right] \cos(\varphi - \eta) . \quad (8)$$

$$\begin{aligned}
 P_z = & \left\{ [tg(\varphi \pm \omega)] \int_0^S \sigma_i \varepsilon_{ii} \frac{\cos \beta}{\sqrt{3} \sin \beta_1 \cos(\beta + \beta_1)} d\varepsilon_i + \right. \\
 & + [tS - S^2 \sin(\varphi \pm \omega) \cos(\varphi \pm \omega)] \sigma_i \frac{\cos \beta}{\sqrt{3} \sin \beta_1 \cos(\beta + \beta_1)} + \\
 & \left. + \int_{0,5\pi + (\varphi \pm \omega)}^{H \pm \omega} r - \frac{r - S \sin(\varphi \pm \omega)}{\cos \Theta_i} \frac{\sigma_i \cos \beta}{\sqrt{3} \sin \beta_1 \cos(\beta + \beta_1)} d\Theta_i \right\} + \\
 & + \int_{H \pm \omega}^{\arccos(0,5S/r) \pm \omega} r - S \cos \Theta_i - \sqrt{r^2 - S^2 \sin^2 \Theta_i} \frac{\sigma_i \cos \beta}{\sqrt{3} \sin \beta_1 \cos(\beta + \beta_1)} d\Theta_i + \\
 & + 0,16 \sigma_i \mu (0,5\pi \rho + l_s) \left[\frac{t - r(1 - \cos(\varphi \pm \omega)) \cos(\varphi - \eta)}{\cos(\varphi \pm \omega)} + r(0,5\pi - \arccos(0,5S/r)) \right]. \quad (9)
 \end{aligned}$$

In (8) and (9), the variable H is

$$H = -\text{arctg} \frac{r \cos(\varphi \pm \omega)}{r \sin(\varphi \pm \omega) - S}.$$

The angle η in this case is

$$\eta = \text{arctg} \frac{t - r + [r^2 - (S/2)^2]^{0,5}}{t - r(1 - \cos \varphi) \text{ctg} \varphi + r \sin \varphi + S/2}.$$

It is possible to determine the components P_x and P_y from the known relations:

$$P_x = P_{xy} \sin \eta;$$

$$P_y = P_{xy} \cos \eta.$$

Conclusion. The resulting analytical dependencies express the functional relationship between the elements of cutting modes (feed and depth of cut), the geometric parameters of the cutters (approach angles φ and φ_1 , and tip radius r), the degree of wear (l_w and ρ), the shape of the machined surface (ω), which also affects the position and length of the active parts of the cutting edges of the cutter (ε), and physical and mechanical properties of the work material (σ_i). A large set of parameters included in the formulas for determining the components of the cutting force allows adequate monitoring the nature of the force interaction of the technological system elements when processing parts.

The calculation of cutting forces according to the developed formulas shows that when the inclination angle of the machined surface changes from $+50^\circ$ to -40° (which corresponds to the real conditions for processing complex surfaces), the radial component P_y of the cutting force changes by 4 times, and the axial component P_x changes by 200 times. Such significant changes in the components of the cutting force cause instability in the force load on the technological system and generate elastic displacements of its elements, which in turn increases the cutting inaccuracies.

REFERENCES

- [1]. Vaxevanidis N.M., Kechagias J.D., Fountas N.A., Manolakos D.E. *Evaluation of Machinability in Turning of Engineering Alloys by Applying Artificial Neural Networks*. The Open Construction and Building Technology Journal. Vol., 2015, 8(1), pp. 389-399. DOI:10.2174/1874836801408010389
- [2]. Al-Ahmari A.M.A. *Predictive machinability models for a selected hard material in turning operations*. Journal of Materials Processing Technology, 2007, vol. 190(1), pp. 305-311.
- [3]. Aouici H., Yallese M.A., Chaoui K., Mabrouki T., Rigal J.F. *Analysis of surface roughness and cutting force components in hard turning with CBN tool: Prediction model and cutting conditions optimization*. Measurement, 2012, vol. 45(3), pp. 344-353.
- [4]. Chua M.S., Rahman M., Wong Y.S., Loh H.T. *Determination of optimal cutting conditions using design of experiments and optimization techniques*. International Journal of Machine Tools and and Manufacture, 1993, vol. 33(2), pp. 297-305.
- [5]. Lapshin V.P., Turkin I.A., Khristoforova V.V. *Assessment of Metal Wear in Turning on the Basis of Components of the Cutting Force*. Russ. Engin. Res., vol. 40, pp. 797–800 (2020). <https://doi.org/10.3103/S1068798X20090099>
- [6]. Vaxevanidis N.M., Fountas N.A., Kechagias J., Malonakos D.E. *Estimation of Main Cutting Force and Mean Surface Roughness in Turning of AISI D6 Tool Steel using Design of Experiments and Artificial Neural Networks*. In book MACHINING: Operations, technology and management, Nova Publishers, 2013, pp. 159-187.
- [7]. Hwang Y.K., Lee C.M. *Surface roughness and cutting force prediction in MQL and wet turning process of AISI 1045 using design of experiments*. Journal of Mechanical Science and Technology, 2010, vol. 24(8), pp. 1669-1677.
- [8]. Sieben B., Wagner T., Biermann D. *Empirical modeling of hard turning of AISI 6150 steel using design and analysis of computer experiments*. Production Engineering, 2010, vol. 4(2-3), pp. 115-125.
- [9]. Youssef Y.A., Beauchamp Y., Thomas M. *Comparison of a full factorial experiment to fractional and Taguchi designs in a lathe dry turning operation*. Computers & industrial engineering, 1994, vol. 27(1-4), pp. 59-62.
- [10]. Tan L., Chen Z., Huang J., et al. *Empirical models for cutting forces in finish dry hard turning of hardened tool steel at different hardness levels*. Int. J. Adv. Manuf. Technol., 2014, vol.76, pp. 691–703. <https://doi.org/10.1007/s00170-014-6291-8>
- [11]. Orra K., Choudhury S.K. *Mechanistic modelling for predicting cutting forces in machining considering effect of tool nose radius on chip formation and tool wear land*. Int. J. Mech. Sci., 2018, vol. 142–143, pp. 255–268. <https://doi.org/10.1016/j.ijmecsci.2018.05.004>
- [12]. Campocasso S., Poulachon G., Costes J.P., Bissey-Breton S. *An innovative experimental study of corner radius effect on cutting forces*. CIRP Ann. Manuf. Technol, 2014, vol. 63, pp. 121–124. <https://doi.org/10.1016/j.cirp.2014.03.076>
- [13]. Imani B.M., Yussefian N.Z. *Cutting force simulation of machining with nose radius tools*. IEEE. International Conference on Smart Manufacturing Application, 2008, pp. 19–23.
- [14]. Arsecularatne J.A., Mathew P., Oxley P.L.B. *Prediction of chip flow direction and cutting forces in oblique machining with nose radius tools*. Proc. Inst. Mech. Eng. Part B J. Eng. Manuf., 1995, vol. 209, pp. 305–315. https://doi.org/10.1243/PIMEPROC_1995_209_087_02
- [15]. Abdellaoui L., Bouzid W. *Thermomechanical approach for the modeling of oblique machining with a single cutting edge*. Mach. Sci. Technol, 2016, vol. 20, pp. 655–680. <https://doi.org/10.1080/10910344.2016.1224020>
- [16]. Abdellaoui L., Bouzid W. *Thermomechanical modeling of oblique turning in relation to tool-nose radius*. Mach. Sci. Technol, 2016, vol. 20, pp. 586–614. DOI:10.1080/10910344.2016.1224017.

- [17]. Özel T., Hsu T.K., Zeren E. *Effects of cutting edge geometry, workpiece hardness, feed rate and cutting speed on surface roughness and forces in finish turning of hardened AISI H13 steel*. The International Journal of Advanced Manufacturing Technology, 2005, vol. 25 (3-4), pp. 262-269.
- [18]. Endres W.J., Kountanya R.K. *The effects of corner radius and edge radius on tool flank wear*. J. Manuf. Process, 2002, vol. 4, pp. 89–96. [https://doi.org/10.1016/S1526-6125\(02\)70135-7](https://doi.org/10.1016/S1526-6125(02)70135-7)
- [19]. Bartarya G., Choudhury S. K. *Effect of cutting parameters on cutting force and surface roughness during finish hard turning AISI52100 grade steel*. Procedia CIRP, vol. 1, pp. 651-656 (2012).
- [20]. Meyer R., Köhler J., Denkena B. *Influence of the tool corner radius on the tool wear and process forces during hard turning*. Int. J. Adv. Manuf. Technol, 2012, vol. 58, pp. 933–940. <https://doi.org/10.1007/s00170-011-3451-y>
- [21]. Childs T.H.C., Sekiya K., Tezuka R., et al. *Surface finishes from turning and facing with round nosed tools*. CIRP Ann, 2008, vol. 57, pp. 89–92. <https://doi.org/10.1016/j.cirp.2008.03.121>
- [22]. Guzeev V.I. *Improving the efficiency of integrated technological processes at the stages of design and implementation*. (in Russ). Science-intensive technologies in mechanical engineering, 2014, No. 7 (37). pp. 36-41.

Received: 14.03.2023

Accepted: 16.05.2023



PROCESSING OF TIME SIGNALS IN A DISCRETE TIME DOMAIN

Victor ARTEMYEV^{1*}, Sergey MOKRUSHIN², Sergey SAVOSTIN³,
Artem MEDVEDEV⁴, Vitaly PANKOV⁵

^{1*234}Federal State Budgetary Educational Institution of Higher Education “Russian Biotechnological University (ROSBIO TECH)”, departments of “Computer Science and computer technology of food production”, Moscow, Russian Federation

⁵Federal State Budget Educational Institution of Higher Education “MIREA-Russian Technological University”, Moscow, Russian Federation

E-mail: artemyevvs@mgupp.ru^{1*}, mokrushin@mgupp.ru², savostin@mgupp.ru³, am@helpexcel.pro⁴,
pankovvv@mirea.ru⁵

Abstract: This article is devoted to the processing of time signals in a discrete time domain. Time signals are the main object of analysis in many areas, such as signal processing, communication, control and much more. Today, for efficient signal processing, it is necessary to use methods adapted to the discrete time domain, using the Z-transform method to solve difference equations in the discrete time domain. The Z-transform method is a powerful and most effective tool for analyzing and solving difference equations, widely used in control systems, signal processing and other fields. The main steps of applying the Z-transformation method are also presented, starting from the formulation of the difference equation to obtaining a solution in the original time domain. Special attention is paid to the Z-transformation process, where the difference equation turns into an algebraic equation with respect to the Z operator. The basic properties of the Z-transformation and the operations with them necessary for the successful application of the method are described.

Keywords: temporary domain, discrete form, transformations, geometric progression, difference equation.

Introduction. Processing of time signals is one of the key tasks in many areas, including signal processing, communication, control and many others. Effective signal processing is based on the use of methods adapted to the discrete time domain [1,2].

In the discrete time domain, the signals are presented in a discrete form consisting of a sequence of samples. This allows the use of various algorithms and processing methods specially designed to work with such discrete signals [3].

In the constant striving for the development and improvement of technologies in the modern scientific community, the study and application of various methods for solving difference equations is relevant. One of such methods that attracts considerable attention of researchers and engineers is the Z-transformation method. In this article we present an exhaustive analysis and new results obtained using this method [4].

The problem of solving difference equations is to find an analytical expression for the dependence between successive values of discrete variables in a discrete time domain. The Z-transform method allows you to move from a discrete time domain to a complex frequency domain using the Z operator. It provides an effective tool for analyzing and designing various systems based on difference equations [5-9].

In the course of our research, we conducted an in-depth analysis of the basic principles and theoretical aspects of the Z-transformation method. We have studied its properties, established convergence and stability conditions, and developed new methods and approaches for solving difference equations using this method [10-15].

The main results of our research include the development of algorithms for solving difference

equations by the Z-transform method, analysis of their accuracy and stability, as well as optimization of the solution process using modern computing technologies.

One of the key aspects of processing time signals in a discrete time domain is sampling and quantization. Sampling is the process of splitting a continuous time signal into discrete samples. Quantization, in turn, refers to the process of converting analog signal values into a finite number of levels.

The main tool for processing time signals in a discrete time domain is the Fourier series transformation. The Fourier transform makes it possible to analyze the spectral characteristics of a signal, isolate its component frequencies and filter the signal in the frequency domain. To quickly calculate the Fourier transform, there is a fast Fourier transform algorithm that significantly reduces computational complexity.

Another method of processing time signals in a discrete time domain is the discrete cosine transform, which is widely used in data compression, image and sound compression, as well as in other areas where signal analysis and processing are required.

In addition, in the field of processing time signals in a discrete time domain, methods of spectral analysis, power spectral density estimation, time characteristics extraction and many other methods and algorithms are actively used. The use of these methods makes it possible to achieve more accurate analysis and processing of time signals, as well as to reveal hidden features and information contained in these types of signals.

One of the areas where processing of time signals in a discrete time domain is widely used is digital audio processing. With the help of appropriate methods, it is possible to process audio signals, including noise reduction, equalization, compression and other operations.

Another area of application of time signal processing in the discrete time domain is image processing. Using the appropriate algorithms, you can perform filtering, sharpening, segmentation and other operations on images. It finds application in the fields of computer vision, medical diagnostics, as well as in various tasks of image processing and analysis.

Along with these areas, the processing of time signals in a discrete time domain also finds application in radio communications, radar, signal management and many other areas where it is necessary to analyze, process and transmit signals using digital methods.

In addition, processing time signals in a discrete time domain has its advantages over analog signal processing. It allows the use of digital processing methods that provide higher stability, accuracy and flexibility when working with signals [16,17].

One of the key components of processing time signals in a discrete time domain is the conversion of time signals into sequences of numbers. This is done by sampling, where the signal is split into discrete samples, which can then be processed by digital algorithms [19].

After sampling, the signal can be represented in the form of a sequence of numbers that can be processed using various methods and algorithms. An important tool in this process is the Z-transform, which allows you to analyze and process signals in a discrete time domain.

The Z-transform method is a powerful tool for analyzing and processing time signals. It allows you to represent a time signal in the form of a Z-transformation, which is expressed in terms of coefficients and powers of the Z operator. Then, using algorithms and methods based on the Z-transformation, various operations can be performed with signals, such as filtering, deconvolution, spectrum estimation, and others [20,21].

The advantages of the Z-transform method include its versatility and applicability to various types of signals, the ability to accurately model and analyze signal systems, as well as ease of use and understanding. This makes the Z-transform method one of the main tools in the field of time signal processing [22,23].

Problem statement. Thus, our research is devoted to the deep analysis and development of the Z-transformation method for solving difference equations. In which the results obtained are an important contribution to the field of theory and practical application of this method.

Our work is aimed at improving the accuracy, efficiency and reliability of solving difference equations using this method.

By analyzing and optimizing Z-transformation algorithms to improve speed and computational efficiency. We found that this allowed us to reduce the calculation time and improve the performance of systems based on difference equations.

Secondly, by applying this Z-transformation method in combination with other methods and algorithms, such as the finite difference method, the finite element method or artificial intelligence methods. it allowed us to create more complex and powerful tools for solving complex problems and optimizing systems.

And finally, we are going to expand the scope of the Z-transformation method to new areas, such as discrete-time systems, nonlinear systems and systems with variable coefficients [24]. This will allow us to explore new aspects and possibilities of this method and unlock its potential in a wider range of applications.

The Z-transform method is one of the effective methods for solving difference equations in a discrete domain. To solve the difference equation by the Z-transformation method, the following steps follow [25]:

We set the difference equation in discrete form, for example:

$$a_n y[n] + a_{\{n-1\}} y[n-1] + \dots + a_0 y[0] = b_n x[n] + b_{\{n-1\}} x[n-1] + \dots + b_0 x[0] \quad (1)$$

Here $y[n]$ and $x[n]$ are the values of the function $y(t)$ and $x(t)$ at discrete time points n , a_i and b_i are the coefficients of the difference equation.

We apply the Z-transform to both parts of the equation:

$$a_n Y(z) z^n + a_{\{n-1\}} Y(z) z^{\{n-1\}} + \dots + a_0 Y(z) = b_n X(z) z^n + b_{\{n-1\}} X(z) z^{\{n-1\}} + \dots + b_0 X(z) \quad (2)$$

Here $Y(z)$ and $X(z)$ are the Z-transformations of $y[n]$ and $x[n]$, respectively.

We express the Z-transformation of the desired function $Y(z)$ through the Z-transformation of the input function $X(z)$ and the initial conditions:

$$Y(z) = (b_n X(z) z^n + b_{\{n-1\}} X(z) z^{\{n-1\}} + \dots + \frac{b_0 X(z)}{(a_n z^n + a_{\{n-1\}} z^{\{n-1\}})} + \dots + a_0 \quad (3)$$

Using the table of Z-transformations and the properties of the algebra, we find the inverse Z-transformation for the resulting expression $Y(z)$ in order to obtain a solution of $y[n]$ in the time domain.

The inverse Z-transformation can be performed using methods such as the method of partial fractions, the method of decomposition into the simplest fractions or tables of Z-transformations.

The application of the Z-transformation method makes it possible to transfer the difference equation from the time domain to the Z-domain, where its solution can be found using algebraic operations and knowledge of the Z-transformation table. The result will be the solution of the equation in discrete moments of time.

Considering the simplest equation, which is the sum of the geometric progression using this method:

$$x[n] = 2^n \quad (4)$$

To solve this equation by the Z-transformation method, we apply the following approach: Apply the Z-transformation to both sides of the equation:

$$Z\{x[n]\} = Z\{2^n\} \quad (5)$$

We use the well-known Z-transformation of the geometric progression:

$$Z\{a^n\} = \frac{1}{(1 - az^{(-1)})}, \text{ npu } |z| > |a| \quad (6)$$

Applying this transformation to the right side of the equation, we get:

$$X(z) = \frac{1}{(1 - 2z^{(-1)})}; \quad (7)$$

Now we have an expression for $X(z)$. To get the inverse transformation, we find the decomposition into rational fractions:

$$X(z) = \frac{1}{(1 - 2z^{(-1)})} = \frac{1}{\left(1 - \frac{2}{z}\right)} = \frac{1}{(z - 2)} \quad (8)$$

We apply the inverse Z-transform to find the solution of the original equation:

$$x(n) = Z^{(-1)}\{X(z)\} = Z^{(-1)}\left\{\frac{1}{(z - 2)}\right\} \quad (9)$$

Thus, the solution of this equation of the sum of the geometric progression will be this sequence. Graphically, the sequence $x[n]$ will tend to infinity even faster than in the previous case. The growth will be exponentially accelerated and more pronounced. This is due to the fact that the exponent in the equation has become much larger, which leads to a sharper increase in each element of the sequence.

Solving the problem. We set the difference equation in discrete form, for example:
 Find the solution of the difference equation by the z-transformation method

$$2y_k - 3y_{k-1} + 1,12y_{k-2} = 2 \times 1(k) \quad (10)$$

under zero initial conditions ($y_{-1} = 0$ и $y_{-2} = 0$)

Solving this equation (10) to Z-images taking into account the given zero initial conditions. If $Z\{y_k\} = y(z)$, then according to the lag theorem we have:

$$Z\{y_{k-1}\} = z^{-1}y(z), \quad Z\{y_{k-2}\} = z^{-2}y(z) \quad (11)$$

According to the transformation table, we also find $Z\{1[k]\} = \frac{z}{(z-1)}$. Substituting z-transformations instead of variables in (10) and grouping similar terms, we get

$$(2 - 3z^{-1} + 1,12z^{-2})y(z) = 2 \frac{z}{z-1}$$

Hence follows

$$y(z) = \frac{z^3}{(z-1)(z^2 - 1,5z + 0,56)} \quad (12)$$

Now, to solve the equation, it is enough to find the original of the resulting expression. To this end, we will take out z , and decompose the remaining fraction into the simplest fractions. The roots of the equation $z^2 - 1,5z + 0,56 = 0$ are equal to $z_1 = 0,7, z_2 = 0,8$. Therefore, the right part (12) can be represented as

$$z \left(\frac{z^2}{(z-1)(z-0,7)(z-0,8)} \right) = z \left(\frac{A}{z-1} + \frac{B}{z-0,7} + \frac{C}{z-0,8} \right) \quad (13)$$

The undefined coefficients in this equation will be found:

$$A = \frac{z^2}{(z-0,7)(z-0,8)} \Big|_{z=1} = \frac{1}{0,3 \cdot 0,2} = 16,67,$$

$$B = \frac{z^2}{(z-1)(z-0,8)} \Big|_{z=0,7} = \frac{0,49}{-0,3 \cdot (-0,1)} = 16,33,$$

$$C = \frac{z^2}{(z-1)(z-0,7)} \Big|_{z=0,8} = \frac{0,64}{-0,2 \cdot 0,1} = -32.$$

Substituting the obtained values in (13) and then in (12), and we get

$$y(z) = 16,67 \frac{z}{z-1} + 16,33 \frac{z}{z-0,7} - 32 \times \frac{z}{z-0,8} \quad (14)$$

In accordance with the transformation table, you can write correspondences:

$$\frac{z}{z-1} \rightarrow 1[k], \quad \frac{z}{z-0,7} \rightarrow 0,7^k, \quad \frac{z}{z-0,8} \rightarrow 0,8^k \quad (15)$$

Therefore, the solution of the given equation can have the form

$$y_k = 16,67 \cdot 1[k] + 16,33 \cdot (0,7)^k - 32 \times (0,8)^k \quad (16)$$

The equation is the sum of three components: the first term $16,67 \times 1[k]$ is constant and independent of k , the second term $16,33 \times (0,7)^k$ is a geometric progression with decaying values, and the third term $-32 \times (0,8)^k$ is also a geometric progression, but with increasing values.

The value of y_k depends on the value of k . As k increases, the second term decreases, and the third term increases, which leads to a change in the overall value of y_k . The first term remains constant.

The dependence on the value of k can be used to model various processes where it is necessary to take into account decaying or growing values over time.

Graphically, the values of y_k can be represented as a curve that combines a constant component and two geometric progressions with different rates of change. The shape of the curve will depend on the values of the coefficients and initial conditions, where a variety of dependencies is demonstrated and can be useful for modeling various processes where changes over time are important.

The results of the calculations can be visualized using a graph, where the value of the index k will be plotted on the x axis, and the corresponding value y_k will be plotted on the y axis. This will allow you to visualize the change in the sequence y_k depending on the value of the index k . The graph of the resulting solution is shown in Fig.1.

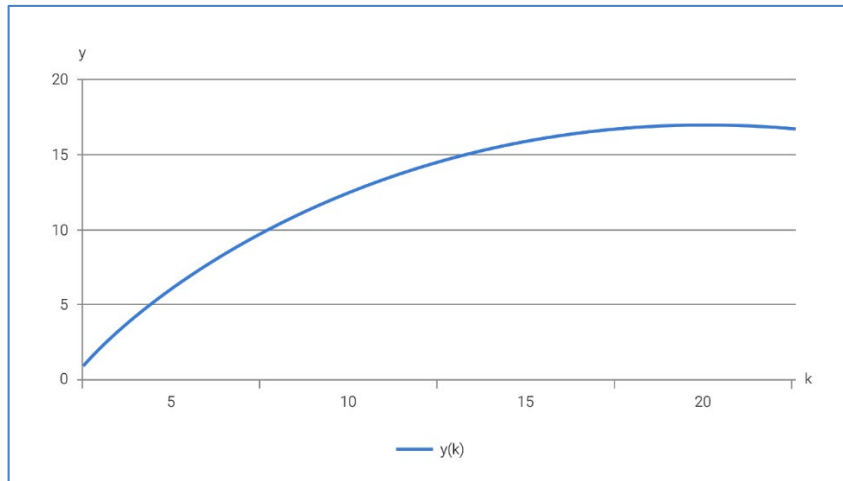


Figure 1. Graph of the solution of the difference equation

The same example is only for a system of differential equations

$$\dot{x} = \begin{bmatrix} -3 & 2 \\ 1 & -2 \end{bmatrix} x + \begin{bmatrix} 0 \\ 1 \end{bmatrix} g \quad (17)$$

$$y = \begin{bmatrix} 2 & 0 \end{bmatrix} x + 0,2g$$

for $x_0 = [1 \ 1]^T$ and $g(t) = 1,5t, t \geq 0$, and plot the dependence of $y(t)$ and $g(t)$ in Figure 2

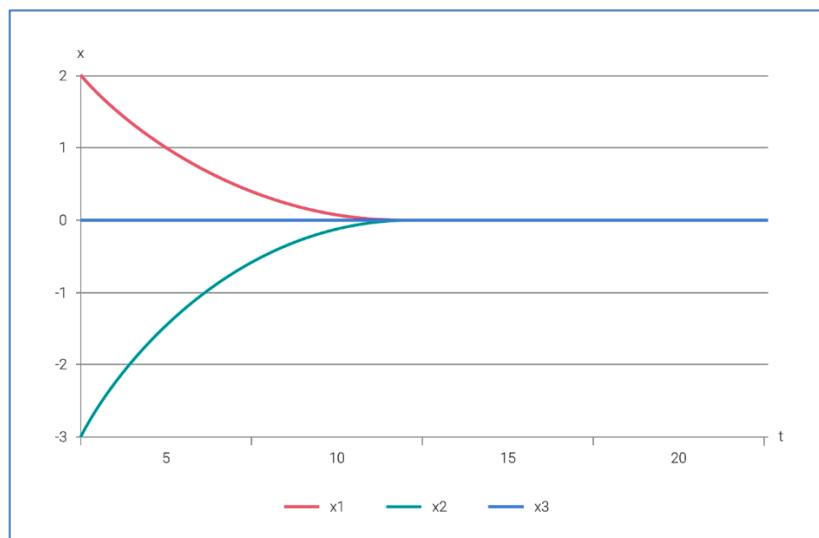


Figure 2. Graph of variable states

The given system of differential equations (17) is a special case of the system

$$\dot{x} = Ax + Bg, \quad (18)$$

$$y = Cx + Dg. \quad (19)$$

The solution of the system (18), (19) is determined by the Cauchy formula:

$$y = Ce^{At}x_0 + \int_0^t Ce^{A(t-\tau)}Bg(\tau)d\tau + Dg(t) \quad (20)$$

Thus, according to the formula (7), it is necessary to first find the matrix e^{At} . In the case of system (17), the matrix A coincides with the matrix for which the matrix e^{At} (18) is found in example (12). Using this expression, we find that the free component of the solution (20) of system (17) will be equal to

$$y_{cB}(t) = Ce^{At}x_0 = \begin{bmatrix} 2 & 0 \end{bmatrix} \begin{bmatrix} 2e^{-4t} + e^{-t} & 2e^{-t} - 2e^{-4t} \\ e^{-t} - e^{-4t} & e^{-4t} + 2e^{-t} \end{bmatrix} \begin{bmatrix} 1 \\ 1 \end{bmatrix} \frac{1}{3} = 2e^{-t} \quad (21)$$

To calculate the integral in (20), we first find the product

$$Ce^{A(t-\tau)}B = \begin{bmatrix} 4e^{-4t} + 2e^{-t} & 4e^{-t} - 4e^{-4t} \end{bmatrix} \begin{bmatrix} 0 \\ 1 \end{bmatrix} \frac{1}{3} = \frac{4}{3}(e^{-t} - e^{-4t}) \quad (22)$$

Next, replacing t by $t - \tau$ here, we write the integral of (20):

$$I = \int_0^t \frac{4}{3}(e^{-(t-\tau)} - e^{-4(t-\tau)})1,5\tau d\tau = 2e^{-t} \int_0^t e^{\tau} \tau d\tau - 2e^{-4t} \int_0^t e^{4\tau} \tau d\tau. \quad (23)$$

Integrating in parts or applying the calculation for $\alpha = 1$ and $\alpha = 4$, we will have

$$I(t) = 2e^{-t} [e^t(t-1) + 1] - 2e^{-4t} \left[e^{4t} \left(\frac{t}{4} - \frac{1}{16} \right) + \frac{1}{16} \right] = \frac{3}{2}t - \frac{15}{8} + 2e^{-t} - \frac{1}{8}e^{-4t} \quad (24)$$

Now, summing up, according to (7), all the components of the solution, we get:

$$y(t) = 2e^{-t} + \frac{3}{2}t - \frac{15}{8} + 2e^{-t} - \frac{1}{8}e^{-4t} + 0,2 \cdot 1,5t = 1,8t - \frac{15}{8} + 4e^{-t} - \frac{1}{8}e^{-4t} \quad (25)$$

The graphs of the functions $g(t)$ and $y(t)$, taking into account the fact that the "slowest" exponent "fades" in this case in 3c, are shown in Fig. 3

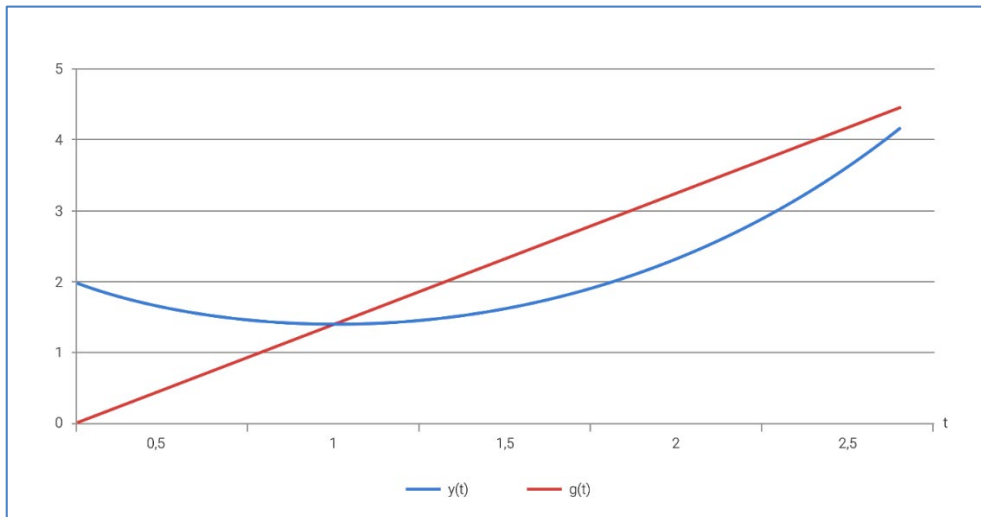


Figure 3. Exciting function of the differential equation system

The resulting solution has a component of $1,8t$ proportional to the input effect $g(t) = 1,5t$, and two exponents $\exp(-t)$ and $\exp(-4t)$, whose exponents are equal to the roots of the characteristic polynomial of the matrix A of a given system of equations (17). All these exponents are eigenmodes of some dynamic the system that is described by these equations.

Conclusion. As a result of the conducted research and application of the Z-transformation in the field of time signal processing, the following complex conclusions can be drawn that when using the Z-transformation, signals can be represented in the form of difference equations, which allows for analysis and processing of signals in a discrete time domain.

The advantages of the Z-transform include its ability to represent complex time signals in a compact and convenient form, as well as to enable various signal processing operations, such as filtering, decomposition and reconstruction of signals, the Z-transform provides an effective tool for analyzing and processing time signals in a discrete time domain.

With the use of the Z-transform, a high degree of flexibility and accuracy can be achieved in the processing of time signals, thanks to the possibility of setting parameters and applying various processing methods. The use of the Z-transform makes it possible to solve various tasks of processing time signals, such as noise filtering, data compression, signal characterization, and others.

The results of the research and application of the Z-transform in this work allow us to assert that this method is an effective tool for analyzing and processing time signals, and its application can lead to significant results in various fields of application.

REFERENCES

- [1]. Sekar, E. Tamilselvan, A. *Finite difference scheme for third order singularly perturbed delay differential equation of convection diffusion type with integral boundary condition*. Journal of Applied Mathematics and Computing, 2019, №61, pp. 73–86.
- [2]. Selvi, P. A. and Ramanujam, N. *A parameter uniform difference scheme for singularly perturbed parabolic delay differential equation with robin type boundary condition*. Applied Mathematics and Computation, 2017, №296, pp. 101–115.
- [3]. Amiraliyev, G. M., Amiraliyeva, I. G., and Mustafa, K., *A numerical treatment for singularly perturbed differential equations with integral boundary condition*, Applied Mathematics and Computation, 2007, №185, pp. 574–582.
- [4]. Kornilov, V.S. *Interdisciplinary scientific communication in the content of teaching applied mathematics*. Bulletin of the RUDN. Series: Informatization of education, 2019, №2, pp. 162-172.
- [5] Ansari, A.R., Bakr, S.A. and Shishkin, G.I. *A parameter-robust finite difference method for singularly perturbed delay parabolic partial differential equations*. Journal of Computational and Applied Mathematics, 2007, №205, pp. 552–566.
- [6] Bashier, E.B.M. and Patidar, K.C. *A novel fitted operator finite difference method for a singularly perturbed delay parabolic partial differential equation*, Applied Mathematics and Computation, 2011, Vol. 217, №9, pp. 4728–4739.
- [7] Das, A. and Natesan, S. *Second-order uniformly convergent numerical method for singularly perturbed delay parabolic partial differential equations*. Int. J. Comput. Math, 2018, 95, pp. 490–510.
- [8] Govindarao, L. and Mohapatra, J. *Numerical analysis and simulation of delay parabolic partial differential equation involving a small parameter*. Engrg. Comput., 37 (2019), 289-312.
- [9] Govindarao, L., Mohapatra, J., and Das, A. *A fourth-order numerical scheme for singularly perturbed delay parabolic problem arising in population dynamics*. J. Appl. Math. Comput., 2020, 63, pp. 171–195.
- [10] Debela, H.G. and Duressa, G.F. *Exponentially fitted finite difference method for singularly perturbed delay differential equations with integral boundary condition*. Int. j. eng. appl. sci., 2019, 11, pp. 476–493.
- [11] Debela, H.G. and Duressa, G.F. *Accelerated fitted operator finite difference method for singularly perturbed delay differential equations with non-local boundary condition*. J. Egyptian Math. Soc., 2020, 28, pp. 1–16.

- [12] Debela, H.G. and Duressa, G.F. *Uniformly convergent numerical method for singularly perturbed convection-diffusion type problems with nonlocal boundary condition*. Int J Numer Methods Fluids, 2020, 92, pp. 1914–1926.
- [13] Kumar D. and Kumari P. *A parameter-uniform collocation scheme for singularly perturbed delay problems with integral boundary condition*. J. Appl. Math. Comput., 2020, 63, pp. 813–828.
- [14] Sekar, E. and Tamilselvan, A. *Singularly perturbed delay differential equations of convection-diffusion type with integral boundary condition*. J. Appl. Math. Comput., 2019, 9, pp. 701–722.
- [15] Sekar, E. and Tamilselvan, A. *Third order singularly perturbed delay differential equation of reaction diffusion type with integral boundary condition*. J. Appl. Math. Comput. Mech., 2019, 18, pp. 99-110.
- [16]. Gorodetskaya, O.Y., Gobareva, Ya. L., Medvedev, A.V. *Forecasting of financial markets using a convolutional neural network*. Problems of Economics and legal practice. 2021, Vol. 17, No. 3. pp. 65-72. – EDN NSUFLT.
- [17]. Artemyev, V.S., Savostin S.D. *Analytics and methods of mathematical modeling of artificial intelligence in automation of control and testing*. Agrarian Science - 2022: Materials of the All-Russian Conference of Young Researchers, Moscow, November 22-24, 2022. – Moscow: Russian State Agrarian University - Moscow Agricultural Academy named after K.A. Timiryazev, 2022. – pp. 340-343.
- [18]. Artemyev, V.S., Savostin S.D. *Automated resource security management systems in digitalization issues*. Agrarian Science - 2022: Materials of the All-Russian Conference of Young Researchers, Moscow, November 22-24, 2022. Moscow: Russian State Agrarian University, Moscow Agricultural Academy named after K.A. Timiryazev, 2022. pp. 344-347.
- [19]. Lu, Huang & Xiaoyu, Yuan & Haodong, Wang & Jin, Li & Xuejiao, Ma & Caihong, Zhang. *Research on Application of Digital Signal Processing Technology in Communication*. IOP Conference Series: Materials Science and Engineering. 799. 012026. 10.1088/1757-899X/799/1/012026.
- [20]. Daud, S. & Chaudhary, K. & Bahadoran, M. & Ali, J. *Z-transform method for optimization of add-drop configuration system*. Laser Technology and Optics. 2015, Vol. 74 No. 8. pp. 101-105.
- [21]. Artemyev, V.S., Savostin S.D. *Automation of methods and algorithms of information and analytical systems*. Vavilov readings - 2022: Collection of articles of the International scientific and practical Conference dedicated to the 135th anniversary of the birth of Academician N.I. Vavilov, Saratov, November 22-25, 2022. – Saratov: Limited Liability Company "Amirit", 2022. – pp. 639-642.
- [22]. Björck, Å. *Numerical Methods in Matrix Computations*. Texts in Applied Mathematics, 2015, Springer International Publishing, 800 p.
- [23]. Artemyev, V.S., Savostin S.D. *Modeling of organizational and technological systems and complexes in the generation of new flows*. Vavilov readings - 2022: Collection of articles of the International scientific and Practical Conference dedicated to the 135th anniversary of the birth of Academician N.I. Vavilov, Saratov, November 22-25, 2022. – Saratov: Limited Liability Company "Amirit", 2022. – pp. 642-646.
- [24]. Gong, Liutang & Wang, Wei. *The Z-transform and comparative dynamics in discrete-time models*. Macroeconomic Dynamics, 2013, 17, pp. 1 - 17.
- [25]. Savoye, Philippe. *On the Inclusion of Difference Equation Problems and Z Transform Methods in Sophomore Differential Equation Classes*. PRIMUS, 2009, 19, pp. 491-499.

Received: 16.02.2023

Accepted: 03.06.2023



THEORETICAL BASIS FOR THE DEVELOPMENT OF AN ALGORITHMIC UNIFIED COMPLEX OF MATHEMATICAL MODELS OF CUTTING FORCES

Nizami YUSUBOV^{1*}, Heyran ABBASOVA², Ramil DADASHOV³

^{1*, 2, 3}Department of Machine Building Technology, Azerbaijan Technical University, Baku, Azerbaijan

E-mail: nizami.yusubov@aztu.edu.az^{1*}, abbasova.heyran@aztu.edu.az²,
dadashov@aztu.edu.az³

Abstract: In the article for practical application within the framework of creating a matrix theory of accuracy of multi-tool machining for a range of multi-tool adjustments (tool setups) of previously developed models of machining error, the necessity of dependence of the coordinate components of cutting forces on technological factors is shown. (parameters of cutting conditions, strength properties of the material being machined, deformation properties of the technological system, etc.). For this purpose, the tasks of cutting force models are established, a systematics of machining schemes used on modern lathes is carried out, highlighting two schemes for the formation of a machined surface (trajectory and profile), and the principles for developing cutting force models are given. Thus, the development of an algorithmic unified complex of mathematical models of cutting forces is substantiated, taking into account the introduced systematics of machining schemes according to the mechanism of formation of the machined surface.

Keywords: *Multi-tool machining, Multi-tool adjustment, Systematics of machining schemes, empirical and analytical models, cutting force models, mathematical models of cutting forces.*

Introduction. As part of the creation of a matrix theory of the accuracy of multi-tool machining [1-17], for a range of multi-tool adjustments, two classes of error models for the dimensions performed have been developed:

- a generalized analytical model of distortion of performed dimensions (for the entire set of multi-tool adjustments performed on automated machines of the turning group);
- models of scattering fields of dimensions performed in multi-tool adjustment.
- In turn, scattering field models are subdivided into two types according to the methodology:
 - analytical models (for homogeneous multi-tool adjustments - tools of the same type in setup);
 - simulation stochastic models (for non-homogeneous multi-tool adjustments - different types of tools in setup, for example, cutters and drills).

In all the listed categories of machining error models, the connection between the error and the technological conditions of machining is carried out through the components of the cutting forces.

Thus, for the practical application of the machining error models developed in [1-17], the dependences of the coordinate components of the cutting forces on technological factors are necessary (parameters of cutting conditions, strength properties of the material being machined, deformation properties of the technological system, etc.). These dependencies establish the so-called cutting force models.

Tasks of Cutting Force Models. The main task of cutting force models, when applied in the developed theory of machining accuracy, is the most complete account of the entire set of factors that determine the magnitude and direction of the cutting force for each used cutting tool and the conditions for its use.

A.A. Koshin's plane-parallel accuracy theory [18] of multi-tool machining is based on

Nizami YUSUBOV, Heyran ABBASOVA, Ramil DADASHOV
Theoretical basis for the development of an algorithmic unified complex of mathematical models of cutting forces

traditional empirical power dependences for the components of cutting forces. Machining error models in the proposed matrix theory of accuracy [1-17] are also formed using power dependences for the components of cutting forces:

$$\begin{aligned}
 P_z &= C_{p_z} t^{x_{p_z}} S^{y_{p_z}} V^{z_{p_z}} K_{p_z}; \text{ where } K_{p_z} = K_{\varphi p_z} K_{\gamma p_z} K_{\lambda p_z} K_{M p_z} K_{r p_z} \\
 P_y &= C_{p_y} t^{x_{p_y}} S^{y_{p_y}} V^{z_{p_y}} K_{p_y}; \text{ where } K_{p_y} = K_{\varphi p_y} K_{\gamma p_y} K_{\lambda p_y} K_{M p_y} K_{r p_y} \\
 P_x &= C_{p_x} t^{x_{p_x}} S^{y_{p_x}} V^{z_{p_x}} K_{p_x}; \text{ where } K_{p_x} = K_{\varphi p_x} K_{\gamma p_x} K_{\lambda p_x} K_{M p_x} K_{r p_x}
 \end{aligned} \tag{1}$$

These dependencies reflect the influence of almost all of the factors mentioned above. Cutting condition parameters t , s and v are taken into account directly. The geometry of the cutting tool is taken into account by means of correction factors $K_{\gamma p_i}$, $K_{\alpha p_i}$, $K_{\varphi p_i}$, $K_{\lambda p_i}$, $K_{r p_i}$ ($i=x, y, z$). The type of cutting and machined materials is determined by the coefficient C_{p_i} ($i=x, y, z$). The hardness of the processed material is given by the coefficient $K_{M p_i}$ ($i=x, y, z$).

In the special and reference literature there are tables of values of the main parameters C_p , exponents x_p, y_p, z_p and correction factors $K_{M p}, K_{\varphi p}, K_{\gamma p}, K_{\lambda p}, K_{r p}$ for common and well-studied cutting conditions [19].

It should be noted that the coordinate components of the cutting force, determined by formulas (1), are specified in the tool coordinate system generally accepted in cutting theory. The Y axis is directed normal to the surface to be machined (for a through cutter, this is the tool axis, for a boring cutter, it is normal to it). The X axis is oriented along the feed vector. The Z axis is perpendicular to the XY plane.

For single-coordinate machining, when the feed vector S is directed along one of the coordinate axes of the machine coordinate system, the components of the cutting forces calculated from the dependencies (1) are trivially consistent with the machine coordinate system, in which the errors of the performed dimensions are calculated in the theory of accuracy. For longitudinal turning, the coordinate systems of the tool and the machine are the same, therefore, from formulas (1), we directly obtain the normal component P_y , the tangential P_z , and the component in the direction of the feed vector (for longitudinal turning, this is the axial component P_x). In transverse turning, the normal to the machined surface is directed along the X axis of the machine, therefore, P_y calculated by (1) is directed along the X axis of the machine, P_x from (1) is directed along the Y axis of the machine.

Machining, when the feed vector is directed along one of the coordinate axes of the machine coordinate system, is typical for traditional universal lathes, as well as for cam-controlled automatic machines (multi-spindle and turret-automatic and semi-automatic). Modern CNC machines of the turning group are characterized by spatial adjustments, when the axes of the tool and machine coordinate systems, as well as the feed vector, are arbitrarily oriented relative to each other in space. Therefore, in the models of cutting forces, this mutual spatial orientation of the tool and machine coordinate systems, as well as the direction of the feed vector, must be taken into account.

As a result, many determining factors for cutting forces can be divided into the following three groups:

-cutting tool characteristic (cutting material, rake angle γ , clearance angle α , nose radius r , side cutting edge angle φ , end cutting edge angle φ_l);

Nizami YUSUBOV, Heyran ABBASOVA, Ramil DADASHOV
Theoretical basis for the development of an algorithmic unified complex of mathematical models of cutting forces

-properties of the material to be machined (strength characteristics – HB, HRC, σ_B , σ_T , surface condition);

-technological factors (amount s and direction e_s of feed S , cutting speed v and depth of cut t , cutting tool orientation e_u).

In addition, stochastic characteristics of the initial parameters are necessary for models of scattering fields of the dimensions performed. In cutting force models, this is, first of all, the magnitude of the scattering of the strength properties of the material being machined (for example, ΔHB) and the range of fluctuations in the depth of cut Δt .

Another, and perhaps the main, task of developing a complex of cutting force models is the mandatory coverage of the entire range of cutting schemes applicable on modern lathes.

Systematics of Machining Schemes. The analysis of multi-tool and single-tool adjustments on modern lathes of the turning group, carried out in [1], showed that there are two different schemes for the formation of a machining error due to different mechanisms for the formation of a machined surface.

It is possible to distinguish two basics, from the standpoint of the mechanism of formation of the machined surface, machining schemes - trajectory and profile. (see Table 1).

Table 1. Basic machining schemes from the point of view of the mechanism of formation of the machined surface

Machining scheme name	Description of the machining scheme	Machining scheme type
Trajectory	The machined surface is formed as a result of moving the cutting tool tip along some given trajectory, while the tool trajectory is a generatrix for the formed surface - a body of revolution.	1
Profile	The machined surface is formed as a result of copying the profile of the cutting tool, i.e. the profile of the tool is a generatrix for the formed surface - the body of revolution.	2

The distribution of the nomenclature of technological transitions for the type of cutting tools on modern lathes of the turning group according to the selected types of machining schemes (Table 1) is given in Table. 2.

Principles for Developing Cutting Force Models. The analysis of existing mathematical models of cutting forces showed that the methodologies for creating a variety of existing models of cutting forces are divided into two types: empirical and analytical. Each of the selected types has a significant number of models developed for various cutting patterns. Table 2 shows the availability of cutting force models for machining schemes for the type of cutting tools on machines of the turning group.

As follows from Table 2, out of the entire set of positions of the cutting tool codifier (21 positions) used in turning, only 5 are provided with cutting force models in full. There are both empirical and analytical models for them. 9 positions, i.e. 42% of tools are not fully provided with cutting force models, there are not even empirical models. 7 positions, i.e. 33% of cutting tools are provided with models at the initial level - there are only the simplest empirical models that reflect typical machining conditions.

Turning on modern automatic machines provides for the simultaneous participation in the

Nizami YUSUBOV, Heyran ABBASOVA, Ramil DADASHOV
Theoretical basis for the development of an algorithmic unified complex of mathematical models of cutting forces

adjustment of several different types of cutters [1, 2, 20] - turning, facing, forming, chamfering, boring, cut-off, grooving, wide, chamfering boring. There is also an extensive range of cutters for CNC machines (carbide prefabricated with mechanical fastening of polyhedral inserts). These are turning tool for contour turning, boring tool, grooving tool. The work of the listed types of cutters refers to various cutting patterns: orthogonal and oblique, free and not free. Therefore, it is necessary to have mathematical models that allow calculating the values of the cutting force components in the direction of the main coordinate axes for various types of turning tools in a wide range of variation of technological factors.

Until now, to calculate the forces when cutting metals, empirical dependencies are used, which provide quite sufficient accuracy for practice. On their basis, normative materials are developed according to cutting conditions. However, in order to obtain empirical dependencies for each material being machined, it is necessary to carry out special experiments, which, due to the large number of factors affecting the cutting forces, turn out to be quite numerous and laborious.

Table 2. Availability of cutting force models for machining schemes for the type of cutting tools on lathes

Type of cutting tool	Models		Type of machining scheme
	Empirical	Analytical	
Turning tool	+	+	1
Chamfer cutter	-	-	2
Grooving cutter	+	-	2
Wide cutter	-	-	2
Form tool	-	-	2
Knurling tool	-	-	
Boring tool	+	+	1
Boring chamfer cutter	-	-	2
Facing tool	+	+	1
Cut-off tool	+ ($\varphi=\pi/2$)	-	2
Drill-centering tool	-	-	2 _o
Drill	+	-	1 _o
Core-drill	+	-	1 _o
Countersink	+	-	2 _o
Reamer	+	-	1 _o
Thread cutter	+	-	2
Turning tool made for CNC machines	+	+	1
Contour cutter with multifaceted insert for CNC machines	-	-	1
Boring cutter made for CNC machines	+	+	1
Thread cutter with multifaceted insert for CNC machines	-	-	2
Grooving cutter made for CNC machines	-	-	2

In addition, empirical models are subjective in form and set of variables and, therefore, have a number of significant drawbacks. The nature of dependencies, as a rule, is taken from the conditions of their greatest simplicity. Because of this, power-law models are most often used, although the real

curves describing force dependences are complex, often extremal.

The modern concept of metal cutting is based on the position that this process is a kind of elastic-plastic deformation process. Such processes are mathematically described, which is a prerequisite for the analytical determination of cutting forces.

In principle, for the theory of machining accuracy, it does not matter what the nature of the mathematical model of cutting forces is - empirical or analytical. It is important that it reliably reflects all the necessary patterns of the cutting process and the influence of control factors - cutting conditions.

In [1], the problem was posed and, in relation to multi-tool machining on modern lathes, an algorithmically unified complex of error models for the dimensions performed was developed. To ensure the algorithmic unity of the developed theory of accuracy of multi-tool machining, it is necessary that the complex of mathematical models of cutting forces be algorithmically unified.

Conclusions. Two schemes for the formation of machined surface are distinguished: trajectory and profile. It is substantiated that the most effective way to ensure algorithmic unity is the development of analytical models of cutting forces, taking into account the introduced systematics of machining schemes according to the mechanism of formation of machined surface. The developed set of force models will allow using the obtained accuracy models for all adjustments from the classifier of multi-tool adjustments.

REFERENCES

- [1]. Yusubov, N.D. *Multi-tool machining on automatic lathes (Matrix theory of multi-tool machining accuracy on modern CNC lathes)*. AV Akademikerverlag GmbH & Co. KG / LAP LAMBERT Academic Publishing, Saarbrücken, 2013.
- [2]. Yusubov N.D. *Fundamentals of matrix theory of accuracy of multi-tool turning. (Principles and structure of the theory, design and management of multi-tool machining processes)*. AV Akademikerverlag GmbH & Co. KG / LAP LAMBERT Academic Publishing, Saarbrücken. (2013).
- [3]. Yusubov N.D. *Improving the efficiency of multi-tool processing on the machine tools of the lathe*. Abstract of Dissertation doctor technical sciences, 2009, Baku.
- [4]. Yusubov N.D., Movlazade V.Z., Abbasova, H.M. *Research of sensitivity of full-factor models of scattering fields of dimensions performed in multi-tool machining*. The 8th International Conference on Control and Optimization with Industrial Applications (COIA 2022), vol. II, pp. 480-482.
- [5]. Yusubov N.D., Movlazade V.Z., Abbasova, H.M. *Accuracy models of machining in multi-tool adjustments*. The 8th International Conference on Control and Optimization with Industrial Applications (COIA 2022), vol. II, pp. 477-479.
- [6]. Yusubov N.D., Abbasova H.M. *Model of machining process control on multi-tool single-carriage adjustments*. International Conference on Artificial Intelligence and Applied Mathematics in Engineering 2022 (ICAIAME 2022), pp. 186.
- [7]. Koshin A.A., Yusubov N.D. *Elements of the matrix theory of multi-tool machining accuracy in spatial adjustments*. Technical journal "Bulletin of mechanical engineering", 2013, 9, pp. 13-17.

- [8]. Yusubov N.D., Abbasova H.M. *Full-factor matrix model of accuracy of dimensions performed on multi-purpose CNC machines*. *Obrabotka metallov (tekhnologiya, oborudovanie, instrumenty) = Metal Working and Material Science*, 2021, vol. 23, no. 4, pp. 6–20.
<https://doi.org/10.17212/1994-6309-2021-23.4-6-20>
- [9]. Bogatenkov S.A., Sazonova N.S., Yusubov N.D., Mammadov P.V., Bazhenov R.I. *Increasing the Productivity of Multitool Machining on Automated Lathes by Optimizing the Machining Plan*. *Russian Engineering Research*, 2021, vol. 41, pp. 1071–1074.
<https://doi.org/10.3103/S1068798X21110046>
- [10]. Bogatenkov S.A., Sazonova N.S., Guzeev V.I., Yusubov N.D., Abbasova H.M. *Increasing the Productivity of Multitool Machining on Automated Lathes by Optimizing the Tool Positions*. *Russian Engineering Research*, 2021, vol. 41, pp. 1075-1079.
<https://doi.org/10.3103/S1068798X21110058>
- [11]. Yusubov N., Abbasova H., Khankishiyev I. *Entwicklung einer Projektierungstheorie für die Mehrwerkzeuga bearbeitung mit den Möglichkeiten der modernen CNC-Werkzeugmaschinen*. *Forschung im Ingenieurwesen*, 2021, 85, pp. 661-678.
<https://doi.org/10.1007/s10010-021-00478-7>
- [12]. Yusubov N.D., Abbasova H.M. *Models for Machining Accuracy in Multi-Tool Adjustment*. *International Journal of Automotive and Mechanical Engineering*, 2020, vol. 17, no. 3, pp. 8067-8085. <https://doi.org/10.15282/ijame.17.3.2020.01.0605>
- [13]. Yusubov N.D., Abbasova H.M. *Full Factorial Models of Dimensional Accuracy of Multi-Tool Machining on Automatic Turning Machines*. *Bulletin of the South Ural State University. Ser. Mechanical Engineering Industry*, 2019, vol. 19, no. 1, pp. 56–67.
- [14]. Yusubov N.D. *Matrix Models of Processing Accuracy in Multitool Turning*. *Mechanical Engineering Technology*, 2013, no.1, pp. 57-63.
- [15]. Koshin A.A., Yusubov N.D. *The simulation stochastic model of the dispersion fields of the size performed in multi -tool multi-carriage items*. *Scientific Notes*, 2007, no.1, pp. 32-35.
- [16]. Yusubov N., Maemmaedov A., Abbasova H. *Ein stochastisches Simulationsmodell der Streufelder der zu erfuellenden Masse fuer Mehrwerkzeuq – Mehrsupport – Einrichtungen bei der Drehbearbeitung*. *Brandenburgische Technische Universitaet Cottbus–Senftenberg*, 4. Ingenieurtag 2018 der Fakultaet Maschinenbau Elektro-und Energie-systeme und der Fakultaet Architektru, Bauingenieurwesen und Stadtplanung, neseff – Netzwerktreffen 2018. *Tagungsband*, pp. 115-124.
- [17]. Yusubov, N.D. *Matrix models of the accuracy in multitool two-support setup*. *Russian Engineering Research*, 2009, 29, pp. 268-271. <https://doi.org/10.3103/S1068798X09030125>
- [18]. Koshin A. *Precision theory and optimization of multi-tool turning*. *Dissertation*, University of Chelyabinsk, 1997.
- [19]. Dalsky A., Kosilova A., Mesheryakova R., Suslova A. *Handbook of a mechanical engineering*. in 2 volumes. T.1. *Mechanical engineering*, Moscow, 2003.
- [20]. Yusubov N.D. *Experimental determination of the cutting force in turning*. *Mechanical Engineering*, 2003, vol 43, no. 3, pp. 23-25.

Received: 16.02.2023

Accepted: 03.04.2023

KINEMATIC CALCULATION OF VARIABLE CURVATURE FIST MECHANISM WITH CONVEX PROFILE

Ahmad IMANOV

Department of Mechatronics and Machine Design of Azerbaijan Technical University, Baku, Azerbaijan

E-mail: ehmed.imanov@aztu.edu.az

Abstract: In order to take into account more boundary conditions, a new modified equation was obtained to establish the profile of the fist by adding a constant to the equation obtained from the solution of the differential equation of curvature (i.e., $k < 0$ - convex profile surface as a special case). Based on this equation, the expression defining the movement of the pusher based on the rotation angle of the fist was deduced. The kinematic report of the punching mechanism was performed on the basis of a modified formula. During the kinematic calculations, it was found that there are no jumps in the displacement, velocity and acceleration diagrams of the pusher, that is, the mechanism works smoothly. In order to verify that the curvature takes a negative value along the profile, the equation of the curvature was deduced, its graph was plotted and its accuracy was confirmed.

Keywords: profile, punch, flat pusher, speed, momentum, punch mechanism, impact, radius of curvature.

Introduction. The task of the punch is to convert the rotational movement of the shaft into the forward movement of the pusher. The profile of the fist is formed by a circle, a straight line and various curved lines that meet each other [1]. Figure 1 shows a convex profile gas distribution mechanism that actuates the valve of an internal combustion engine with a flat pusher.

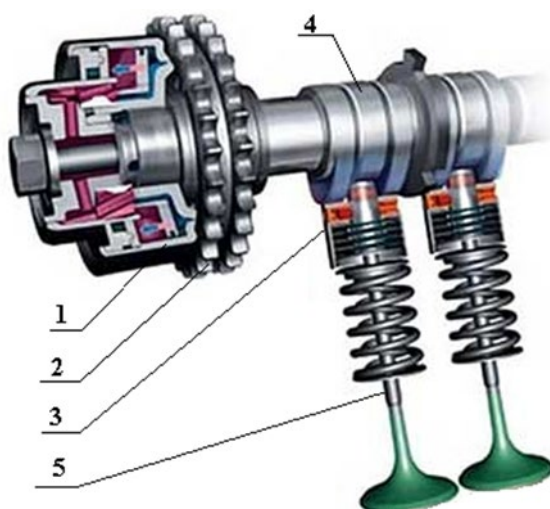


Figure 1. Gas distribution mechanism:

1 - clutch; 2 - wheel; 3 - thruster; 4 - punched shaft; 5 - valve.

The works of many authors are devoted to the modeling, design, kinematic and dynamic analysis of punching mechanisms. For example, T.A. Polyakova (with co-authors) carried out a kinematic report of the camshaft punch of the gas distribution mechanism of diesel engines using the graphical method, using the MathCAD program. As a result, they constructed displacement, velocity and acceleration diagrams of the thruster [2]. H.D.Desai and V.K.Patel performed computer-aided kinematic and dynamic analysis of the punch and pusher to determine the critical angular velocities of each section [3]. R.D.V. Prasad (with co-authors) performed a kinematic and dynamic analysis for

the modification of a flat pusher punch mechanism. The aim of the study was to improve the performance of the mechanism by reducing the contact stresses in the meeting areas. The authors defined expressions for displacement, speed and acceleration of the pusher and punch based on geometrical parameters [4]. M. Mali (with co-authors) used point contact, replacing the flat pusher with a convex pusher, in order to increase the efficiency of the mechanism in four-stroke internal combustion engines, to reduce the friction force [5]. I.A. Khalilov (with co-author) kinematic analysis of the punched mechanism built on the basis of the curvature quality indicator, in his scientific article, in solving the design and optimization issues of the punched mechanism profiled on the basis of the curvature, which is one of the geometric criteria of quality, analytical with the application of the MathCAD program, and with the application of the SolidWORKS program, the most promising for today considered, kinematic analysis based on computer numerical experiment was given [6].

Modern CNC (Computer Numerical Control) machines, which perform profiling with high precision, are widely used in punch manufacturing technologies. It is very important to have accurate coordinates for processing the profile on CNC machines. Since the known graphical methods for determining coordinates [7] are rather imprecise, profiling is mainly built with analytically obtained curves.

Analytical calculation of the fist. At high speeds of the shaft, the smooth change of curvature along the profile ensures the absence of shocks in the punch mechanism. The only geometrical parameter that affects the contact stress in punched mechanisms intended to work under a large load is the introduced curvature radius [8]. The monotonous change of the radius of curvature without a jump in the graph during the departure and approach phases allows for the absence of the first type of shocks in those phases.

The profile of the punch in mechanisms with a flat pusher punch is made in a convex shape. To provide convexity to all points of the profile, its curvature factor $k < 0$ condition must be met. In the presented article, the differential equation of curvature (1) for constructing a profile with a variable curvature coefficient with a convex profile, in a special case, the equation of a convex profile curve (2) was obtained [9].

$$k(x) = \frac{\frac{d^2 y}{dx^2}}{\sqrt{\left(1 + \left(\frac{dy}{dx}\right)^2\right)^3}}, \quad (1)$$

The equation of the curve in (1) is not clearly defined. With the coefficient of curvature being negative, that is, convex, the equation of the profile line can be obtained by using the trigonometric equation (2) provided that certain criteria are met [10-12]:

$$k(x) = -a \cdot \sin(p \cdot x), \quad (2)$$

where $k(x)$ - function of curvature; y is the equation of the profile curve.

Equation (2) can be solved taking into account (1) and the following expression can be obtained

$$y(x) = \frac{1}{p} \ln \left(\sin(p \cdot x) + \sqrt{\left(\frac{p}{a}\right)^2 - \cos^2(p \cdot x)} \right) + C, \quad (3)$$

where C is an integral constant.

The presence of three constants (a, p, C) in expression (3) complicates the use of four boundary conditions. That is, the report is redone by changing some input parameters to satisfy the fourth boundary condition. This increases the number of iterations and necessitates undesired corrections to some of the input parameters. However, this problem can be solved by adding a new constant to expression (3). By adding the constant K to expression (3), all basic boundary conditions can be taken into account. These are: starting (x_1, y_1), ending (x_2, y_2) points and tangents at these points (t_1 and t_2) (Figure 2).

$$y(x) = \frac{K}{p} \ln \left(\sin(p \cdot x) + \sqrt{\left(\frac{p}{a}\right)^2 - \cos^2(p \cdot x)} \right) + C, \quad (4)$$

Expression (4) is called the modified equation of (3).

Input parameters are set to perform kinematic calculations using MathCAD software. These parameters include: $r_0 := 20$, $r_1 := 20$, $\varphi_1 := 10^\circ$, $\varphi_2 := 10^\circ$, $a_0 := |o_0o_1| = 28$, $x_1 := r_0 \cdot (1 - \cos(\varphi_1 \cdot \text{deg}))$ (Figure 2), $x_2 := \frac{-r_1 \cdot \tan(\varphi_2 \cdot \text{deg})}{\sqrt{1 + \tan^2(\varphi_2 \cdot \text{deg})}} + r_0$, $y_1 := r_0 \cdot \sin(\varphi_1 \cdot \text{deg})$, $y_2 := \sqrt{r_1^2 - (x_2 - r_0)^2} + a_0$ - y_2 is obtained

To find the coefficients of p, a, C, K in (4), the following system of equations is jointly solved in Mathcad, subject to the aforementioned boundary conditions.

Given

$$\frac{K}{p} \ln \left(\sin(p \cdot x_1) + \sqrt{\left(\frac{p}{a}\right)^2 - \cos^2(p \cdot x_1)} \right) + C = y_1$$

$$\frac{K}{p} \ln \left(\sin(p \cdot x_2) + \sqrt{\left(\frac{p}{a}\right)^2 - \cos^2(p \cdot x_2)} \right) + C = y_2$$

$$\frac{dy(x_1)}{dx} = \tan(\varphi_1 \cdot \text{deg})$$

$$\frac{dy(x_2)}{dx} = \cot(\varphi_2 \cdot \text{deg})$$

$$\begin{pmatrix} p \\ a \\ C \\ K \end{pmatrix} = \text{Find}(p, a, C, K)$$

The following formulas are used to convert from the Cartesian coordinate system to the polar coordinate system (Figure 3). Polar angle $\varphi(x) := a \tan\left(\frac{y(x)}{r_0 - x}\right)$ and polar radius $|o_0A| := \sqrt{y(x)^2 + (r_0 - x)^2}$ are determined by expressions. Figure 3 is used to derive the thruster displacement equation at interval $|x_1, x_2|$. From the figure, it is the angle formed by the tangent at

point $\varphi_t(x) := a \tan\left(\frac{dy(x)}{dx}\right) - x, y$ with the axis of x . In interval $(x_2, r_0]$, equation $y(x)$ is replaced by $y_{r_1}(x) := \sqrt{r_1^2 - (x - r_0)^2} + a_0$, and $\varphi_t(x)$ by $\varphi_{r_1}(x) := a \tan\left(\frac{dy_{r_1}(x)}{dx}\right)$ for a circle with a radius of r_1 .

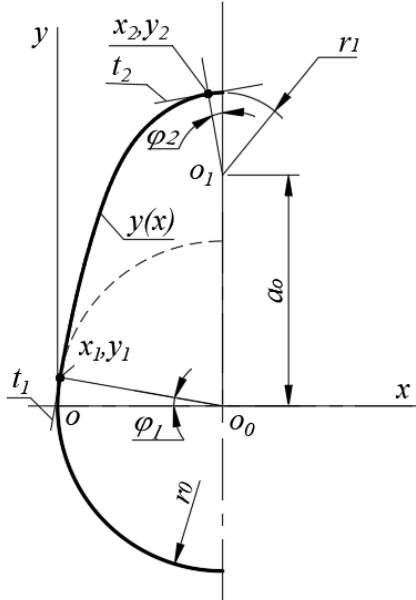


Figure 2. Graphical representation of boundary conditions.

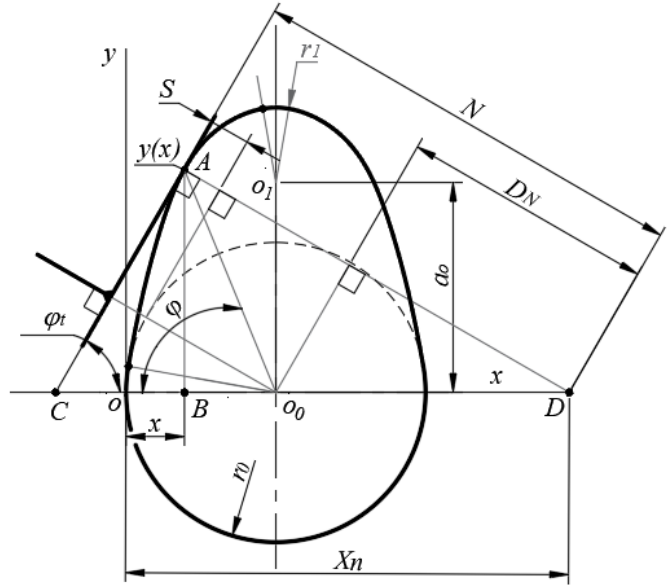


Figure 3. Profile of the fist

As can be seen from Figure 2 and Figure 3, the displacement of the thruster is denoted by S and is found as follows.

$$S(x) := \begin{cases} N(x) - D_N(x) - r_0 & \text{if } x \leq r_0 \\ \frac{y_{r_1}(x)}{\cos(\varphi_{r_1}(x))} - r_0 & \text{otherwise} \end{cases} \quad (5)$$

where from Figure 3, $N(x) = \frac{y(x)}{\sin\left(\frac{\pi}{2} - \varphi_t(x)\right)}$, $D_N(x) = \left(\frac{y(x)}{\tan\left(\frac{\pi}{2} - \varphi_t(x)\right)} + x - r_0 \right) \cdot \cos\left(\frac{\pi}{2} - \varphi_t(x)\right)$.

The movement of the pusher is carried out by the equation (5) in the interval $|x_1, x_2|$, and the equation of the circle with the center point o_1 and the radius r_1 in the interval $(x_2, r_0]$ is used.

Figure 4 shows the dependence diagram of the thruster rotation angle obtained on the basis of (5). The maximum value of the displacement corresponds to the maximum of a circle with a radius of r_1 at a turning angle of 90° (18 mm), as intended. As can be seen from the speed diagram, it changes smoothly, which means that there are no shocks of the first type (Figure 5). A sharp increase in the speed of the pusher during the take-off phase is an indication of rapid opening of the valves. There are no jumps in the momentum diagram, it changes smoothly, and this is the main condition for the absence of the second type of shocks (Figure 5).

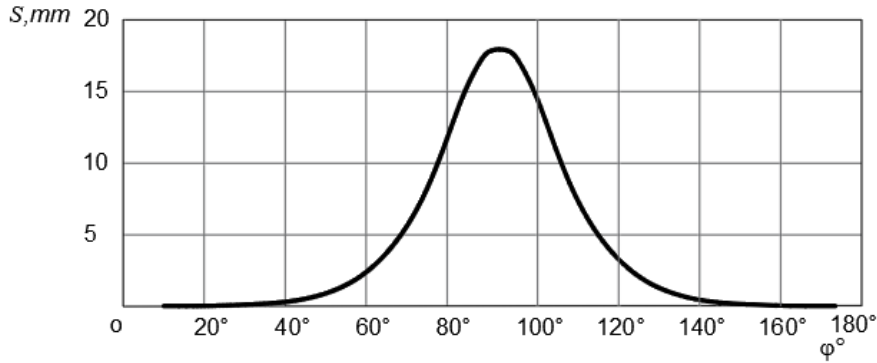


Figure 4. Diagram of dependence of thruster displacement on rotation angle

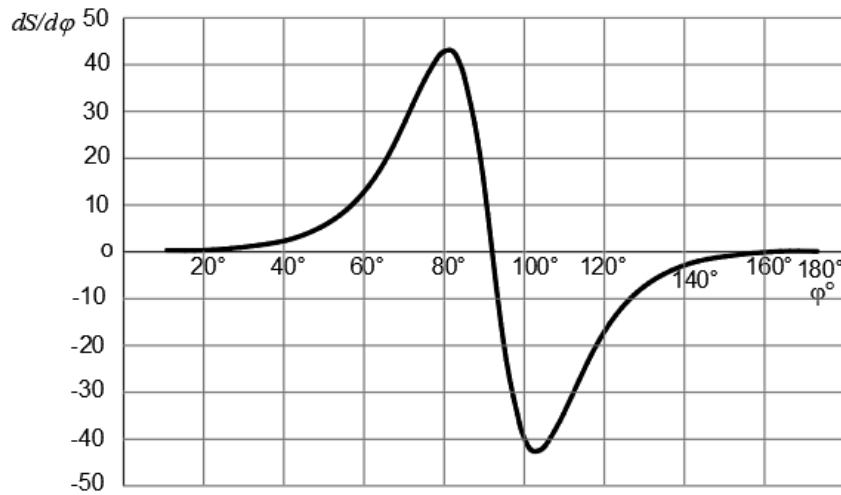


Figure 5. Diagram of the dependence of the speed analog of the thruster on the angle of rotation

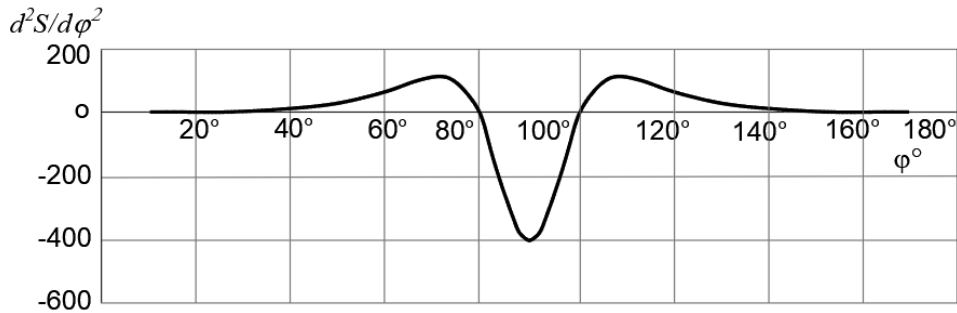


Figure 6. Diagram of dependence of the thruster's momentum analogue on the angle of rotation

As we mentioned, the value of the curvature coefficient is negative throughout the profile, so the profile should theoretically be convex. This boundary condition was used in the derivation of equation (3). However, expression (4) was used to draw the profile curve by adding K correction factors to equation (3) to account for the basic boundary conditions. Equation (4) is a modified version of (3). The curvature coefficient of the profile curve drawn by (4) is determined by expression (6).

$$k(x) := \left(\frac{p}{a}\right)^2 \cdot K \frac{-p \cdot \sin(p \cdot x)}{\left[\left(\frac{p}{a}\right)^2 + \cos(p \cdot x)^2 \cdot (K^2 - 1)\right]^{\frac{3}{2}}} \quad (6)$$

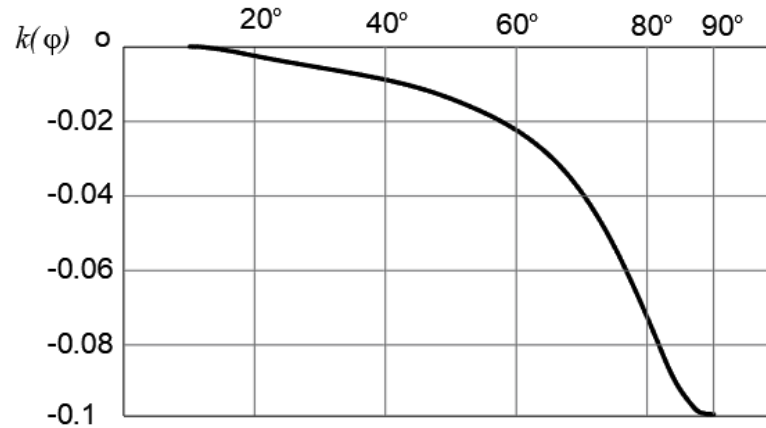


Figure 7. The curvature coefficient of the profile line

As can be seen in Figure 7, the value of the curvature coefficient is negative along the entire profile line. This is the main condition for the profile to be prominent.

Since the pusher is plane and located in the position touching the fist, the pressure angle is zero.

Conculations.

1. The differential equation of curvature for a convex profile, for a special case, was solved and the obtained expression was modified to take into account the main boundary conditions, and a new equation was obtained.

2. The thruster's displacement equation was deduced and the speed and acceleration expressions were obtained by differentiating it. Based on the received statements, the punch mechanism was kinematically calculated, and displacement, speed, and acceleration graphs of the pusher were constructed for visual display.

3. A new approach for the kinematic calculation of a punch mechanism with a convex profile and a variable radius of curvature is given.

4. The curvature formula of the curvature base, which is a criterion of geometric quality, has been derived.

5. The presented method can be used in the creation of special software for kinematic calculation and automatic design of punched mechanisms with a convex profile.

REFERENCES

- [1]. Artobolevsky, I.I. *Theory of mechanisms and machines*. Moskow, Nauka, 1988, 640 p (in Russian).
- [2]. Polyakova, T.A., Makushev, Yu.P., Volkova, L.Yu., Ryndin, V. V. *Kinematic calculation of convex profile cams using the Mathcad program*. Omsk Scientific Bulletin, 2021, No. 5 (179), pp. 34–40.
- [3]. Patel, H.D.P.V. *Computer aided kinematic and dynamic analysis of cam and follower*. In Proceedings of the World Congress on Engineering, 2010, Vol. 2, (in Russian).
- [4]. Prasad, R.D.V., Satyanarayana, K., Maheswara, Ch. et al. *Analysis of Cam and Follower Mechanism to Reduce Jerk and Induced Stresses*. Journal of Recent Trends in Mechanics, 2020, Vol. 5 (3), pp. 8–17.
- [5]. Mali, M., Maskar, P., Gawande, S., and Bagi, J. *Design Optimization of Cam & Follower Mechanism of an Internal Combustion Engine for Improving the Engine Efficiency*. Modern Mechanical Engineering, 2012, Vol. 2, No. 3, pp. 114-119.
- [6]. Khalilov, I.A., Imanov, A.S. *Modeling of the cam mechanism taking into account quality criteria*. Bulletin of Kherson Technical University, 2017, 4(63), pp. 126 – 134 (in Russian).

- [7]. Pylaev, B.V. *Method for profiling flat cams*. Moscow State Agro engineering University named after V.P. Goryachkina, 2010, pp. 78-81 (in Russian).
- [8]. Birger, I.A., Shorr, B.F., Iosilevich, G.B. *Calculation of the strength of machine parts*. Moscow, 1979, 702 p (in Russian).
- [9]. Imanov, A.S., Khalilov, I.A., Aliyev, A.G. *New approach to calculation of transition curves on curved roads*. Proceedings of the International Conference on Problems of Logistics, Management and Operation in the East-West Transport Corridor (PLMO), Baku, Azerbaijan, October 27-29, 2021.
- [10]. Imanov, A.S., Khalilov I.A. *Research of development processes in three-dimensional gas Flows in turbomachine*. "Machine-building and Energy: New Concepts and Technologies" International Scientific-practical Conference materials, AzTU, Baku, Azerbaijan, December 2-3, 2021.
- [11]. Imanov, A.S., Khalilov, I.A. *Blade profile optimization built based on the differential curvature equation*. Proceedings of the 8th International Conference on Control and Optimization with industrial applications. Baku, Azerbaijan. 24-26 August, Vol. 2, 2022, pp. 240-242.
- [12]. Imanov, A.S., Khalilov, I.A. *3D modeling and analysis of gas flow in the interblade channel*. SOCAR Proceedings, 2022, Special Issue 1, pp. 1-5.

Received: 14.09.2022

Accepted: 24.01.2023



INVESTIGATION OF OPTIMAL CONTROL OF VARIABLE SYSTEMS IN THE DYNAMIC SPECTRUM

Victor Artemyev^{1*}, Artem Medvedev², Victor Yaroshevich³

^{1,2}Federal State Budgetary Educational Institution of Higher Education “Russian Biotechnological University (ROSBIOTECH)”, Moscow, Russian Federation

³Belarusian State University of Economics, Minsk, Republic of Belarus

E-mail: artemyevvs@mgupp.ru^{1*}, am@helpexcel.pro², jaroshevich1970@gmail.com³

Abstract: The article presents a study of systems of difference equations, their role and application in modeling and analysis of dynamical systems in various fields. The purpose of the work is to analyze and develop methods for solving difference equations with a special emphasis on their application in automation and mechanics.

Difference equations are mathematical models describing the evolution of variables in a discrete time space. Their study allows for a deeper understanding of complex dynamic processes and effective modeling of systems of diverse nature.

The paper presents an overview of various methods of analysis and solution of difference equations. Numerical integration methods, approximation methods and stabilization methods of systems of difference equations are considered. Special attention is paid to the properties of stability, convergence and controllability of such systems.

The results of the study contribute to a deep understanding of the dynamics of systems of difference equations and the development of effective numerical methods for their solution. The solution of difference equations is widely used in automatic control, robotics, aviation, mechatronics and other industries. It plays an important role in modeling and controlling various systems, including electromechanical systems, robots, autopilots, automation processes, and others.

Keywords: numerical integration methods, approximation methods, stabilization methods for systems of difference equations.

Introduction. Numerical integration methods play an important role in solving differential and difference equations, which are widely used in various fields of science and engineering. One of the most common methods is the Euler method, based on the approximation of the derivative by a difference ratio. This method allows you to approximate the solution of the equation by breaking it into small steps and sequentially updating the values of variables. Thus, the Euler method provides a fast and simple numerical solution of differential and difference equations. It allows you to approximate the value of the function at the next point based on the known value at the previous point. The Euler method is simple to implement, but may not be accurate enough for some tasks [1].

More precise numerical integration methods include Runge-Kutta methods, which use several intermediate steps to refine the approximate solution. Runge-Kutta methods of various orders of accuracy allow to achieve high accuracy of calculations with a sufficiently small integration step [2].

Another common method of numerical integration is the trapezoid method, which is based on the approximation of the area under the graph of the function. It represents the arithmetic mean of the function values at two adjacent points. The trapezoid method has high accuracy and is widely used in numerical calculations.

There are also numerical integration methods based on interpolation, splines and other mathematical approximations. These methods allow you to more flexibly and accurately approximate functions, taking into account their features and the requirements of a specific task.

Numerical integration methods play an important role in solving various problems, such as modeling physical processes, numerical solution of differential equations, calculation of integrals and other mathematical operations.

Approximation methods provide tools for the approximate representation of complex functions that cannot always be accurately described analytically. These methods include various approaches such as polynomial approximation, interpolation, spline approximation, least squares methods and others.

Polynomial approximation is one of the simplest and most widely used methods [3]. It is based on the representation of a function in the form of a polynomial that best approximates its values at a given interval. Depending on the degree of the polynomial, different degrees of approximation accuracy can be achieved. There are several interpolation methods, such as linear interpolation, Lagrange interpolation, Newton interpolation, and others. Each of them has its advantages and limitations depending on the specific task.

Spline approximation is a method that splits an interval into several segments and approximates a function using piecewise polynomial functions called splines [4]. Splines have smoothness and allow more accurate approximation of complex functions, taking into account the peculiarities of the data [5].

Least squares methods are used to find the best approximation of a function by minimizing the sum of squared deviations between the approximating function and the original data. This method allows you to take into account measurement errors and noise in the data, providing the best approximation in terms of least squares.

One of the important areas where approximation methods play a key role is numerical integration. Numerical integration is used to calculate the values of certain integrals when an analytical solution is not available or inefficient. Approximation methods, such as quadrature formulas and Monte Carlo methods, allow you to approximate the values of integrals and obtain results with a given accuracy.

One of the common methods of stabilization is the feedback method. It consists in adding feedback to the system of difference equations in order to suppress possible instabilities and improve its dynamic properties. Feedback can be implemented both linear and nonlinear, and its choice depends on the specific system and the required characteristics.

Another method of stabilization is the use of additional control signals. These signals can be specially designed to maintain the stability of the system and provide the desired characteristics. For example, to stabilize systems of difference equations with nonlinear elements, the adaptive control method can be used, which allows the system to independently adjust control parameters in accordance with changing conditions.

There are also stabilization methods based on the use of filters and compensators. Filters are used to suppress noise and interference in the system, as well as to improve signal quality. Compensators, in turn, are designed to compensate for some dynamic characteristics of the system, such as lag or uneven response.

An important aspect of stabilization methods is the mathematical analysis and study of the stability of systems of difference equations. This includes determining the stability conditions, constructing stable areas, and analyzing the influence of parameters on the stability of the system. This analysis allows you to optimize the stabilization process and choose the most appropriate methods and strategies.

Problem statement. To demonstrate the calculations in numerical integration methods, consider the following equation:

$$\int [a, b] f(x) dx \approx \frac{h}{2} \times [f(a) + 2 \sum [i = 1, n - 1] f(x_i) + f(b)] \quad (1)$$

integration boundaries, $f(x)$ is an integrable function, h is an integration step, n is the number of integration steps, x_i is the values of x at each step.

For example, take the equation:

$$\int [0, 1] x^2 dx \quad (2)$$

Using the numerical integration method, we apply the rectangle formula:

$$\int [a, b] f(x) \approx h \times \sum [i=1, n] f(x_i) \quad (3)$$

where $x_i = a + \left(i - \frac{1}{2}\right) \times h$,

where $i = 1, 2, \dots, n$.

In our case, $a = 0, b = 1, f(x) = x^2$. Let $n = 4$

For each subsequent integration step, in order to obtain a sequence of values of states and control actions during a given time interval, it should be noted that the accuracy and efficiency of integration depends on the chosen numerical integration method and integration step, as well as on the properties and features of the system of difference equations itself. If necessary, you can use more complex integration methods with a smaller step to improve the accuracy of the result.

Then the integration step $h = \frac{(b - a)}{n} = \frac{(1 - 0)}{4} = 0,25$

Calculate the values of x_i :

$$x_1 = 0 + \left(\frac{1}{2}\right) \times 0,25 = 0,125$$

$$x_2 = 0 + \left(\frac{3}{2}\right) \times 0,25 = 0,375$$

$$x_3 = 0 + \left(\frac{5}{2}\right) \times 0,25 = 0,625$$

$$x_4 = 0 + \left(\frac{7}{2}\right) \times 0,25 = 0,875$$

Now substitute the values of x_i into the function $f(x) = x^2$ and calculate:

$$f(x_1) = (0,125)^2 = 0,015625$$

$$f(x_2) = (0,375)^2 = 0,140625$$

$$f(x_3) = (0,625)^2 = 0,390625$$

$$f(x_4) = (0,875)^2 = 0,765625$$

Now we apply the rectangle formula to calculate the approximate value of the integral:

$$\begin{aligned} \int [0, 1] x^2 dx &\approx 0,25 \times [f(x_1) + f(x_2) + f(x_3) + f(x_4)] = \\ &0,25 \times [0,015625 + 0,140625 + 0,390625 + 0,765625] = 0,328125 \end{aligned}$$

Thus, the approximate value of the integral $\int [0, 1] x^2 dx$ is 0 328125, obtained using the numerical integration method and the rectangle formula.

Continuing the complex calculation in the methods of stabilization of systems of difference equations, let's look at a more detailed example.

Suppose we have a system of difference equations of the following form:

$$x[k+1] = Ax[k] + Bu[k] \quad y[k] = C \times x[k] \quad (4)$$

here $x[k]$ is the vector of the system state at time k , $u[k]$ is the vector of input signals at time k , $y[k]$ is the vector of output signals at time k , A , B , C are the matrices of the system.

For simplicity of calculations, assume that the matrices have the following form:

$$A = \begin{bmatrix} 0.8, & 0 \\ 0, & 0.9 \end{bmatrix}$$

$$B = \begin{bmatrix} 0.2 \\ 0.1 \end{bmatrix}$$

$$C = \begin{bmatrix} 1, & 0 \end{bmatrix}$$

Our goal is to stabilize the system, that is, to place the poles inside a single circle.

To do this, we will use the feedback method with positive feedback and select the feedback matrix K .

The feedback is set as follows:

$$u[k] = -K \times x[k] \quad (5)$$

Substitute it back into the system:

$$x[k+1] = Ax[k] + B(-Kx[k]) = (A - BK) \times x[k] \quad (6)$$

Now we have a new system with a matrix $A' = A - B \times K$.

To stabilize the system, it is necessary to choose a suitable feedback matrix K so that all the eigenvalues of the matrix A' are inside the unit circle.

One of the approaches to choosing the K matrix is to use the full control method. To do this, we can use the formula:

$$K = R \times (B^T)^{-1} \times P \quad (7)$$

where R and P are matrices found from the solution of the algebraic Riccati equation:

$$A^{(T)}PA' - P + Q - A^{(T)}PBR^{(-1)}B^TPA' = 0 \quad (8)$$

where Q is the matrix denoting the weight of the error that we want to minimize.

Solving the equations according to this principle, we can always get the matrix K , which will ensure the stabilization of the system.

Solving the problem. The solution of systems of difference equations is of great importance in the field of automation and mechanics, where dynamic systems play a key role in modeling and controlling various processes. Difference equations are discrete analogs of differential equations and are widely used to describe the dynamics of systems that change their values at discrete points in time.

One of the main tasks in automation and mechanics is the development of effective methods for solving systems of difference equations. These methods allow analyzing and predicting the behavior of the system over time, optimizing its parameters, designing and implementing control algorithms.

An important aspect in choosing the method is to ensure the stability and accuracy of the solution of the system of difference equations, as well as taking into account the features of the system and its dynamics. We will find a solution to the system:

$$x_{k+1} = \begin{bmatrix} 0,8 & 1 \\ -0,15 & 0 \end{bmatrix} x_k + \begin{bmatrix} 1 \\ 0,5 \end{bmatrix} g_k, x_0 = \begin{bmatrix} 0,5 \\ -1 \end{bmatrix}, \quad (9)$$

$$y_k = [21] x_k \quad (10)$$

where, x_k and y_k by the z -transformation method, when $T = 0,8c$ and $g_k = kT$.

First of all, only with the help of the method z -transformations $g(z)$ of external influence $g_k = kT$:

$$g(z) = \frac{0,8z}{(z-1)^2} \quad (11)$$

Next, we subject the z -transformation under non-zero initial conditions to obtain

$$zx(z) - zx_0 = \begin{bmatrix} 0,8 & 1 \\ -0,15 & 0 \end{bmatrix} x(z) + \begin{bmatrix} 1 \\ 0,5 \end{bmatrix} g(z)$$

From here, taking into account (11), we deduce

$$\left(zE - \begin{bmatrix} 0,8 & 1 \\ -0,15 & 0 \end{bmatrix} \right) x(z) = zx_0 + \begin{bmatrix} 1 \\ 0,5 \end{bmatrix} \frac{0,8z}{(z-1)^2} \quad (12)$$

To find $x(z)$ from this expression, we calculate first solve the matrix

$$A^{-1}(z) = \text{adj} \frac{A(z)}{\det A(z)} \quad \text{In our case}$$

$$A(z) = \begin{bmatrix} z-0,8 & -1 \\ 0,15 & z \end{bmatrix}, \quad \text{adj}A(z) = \begin{bmatrix} z & 1 \\ -0,15 & z-0,8 \end{bmatrix}$$

$\det A(z) = z^2 - 0,8z + 0,15$. The roots of equation $z^2 - 0,8z + 0,15 = 0$ are $z_1 = 0,3; z_2 = 0,5$.

Therefore $\det A(z) = (z-0,3)(z-0,5)$, and the matrix

$$A^{-1}(z) = \begin{bmatrix} z & 1 \\ -0,15 & z-0,8 \end{bmatrix} \frac{1}{(z-0,3)(z-0,5)}.$$

Multiplying equation (12) by matrix $A^{-1}(z)$ on the left, we get

$$x(z) = \frac{z}{(z-0,3)(z-0,5)} \begin{bmatrix} z & 1 \\ -0,15 & z-0,8 \end{bmatrix} \left\{ x_0 + \begin{bmatrix} 1 \\ 0,5 \end{bmatrix} \frac{0,8}{(z-1)^2} \right\}. \quad (13)$$

First, we calculate the component $x_{ce}(k)$ due to the initial conditions. Her image

$$x_{ce}(z) = \frac{z}{(z-0,3)(z-0,5)} \begin{bmatrix} z & 1 \\ -0,15 & z-0,8 \end{bmatrix} \begin{bmatrix} 0,5 \\ -1 \end{bmatrix} = \frac{z}{(z-0,3)(z-0,5)} \begin{bmatrix} 0,5z-1 \\ 0,725-z \end{bmatrix}. \quad (14)$$

In order to determine $x_{ce}(k)$ from (14) using transformation tables, we decompose the ratio into the simplest fractions

$$\frac{Az+B}{(z-0,3)(z-0,5)} = \frac{D}{z-0,3} + \frac{C}{z-0,5}, \quad (15)$$

where A and B are the given coefficients available in (14), and D and C are unknown coefficients to be found. Applying our methodology, we get

$$D = \frac{Az + B}{z - 0,5} \Big|_{z=0,3}, \quad C = \frac{Az + B}{z - 0,3} \Big|_{z=0,5}. \quad (16)$$

Comparing (14) with (15) and applying formulas (16), we find:

$$x_{ce}(z) = z \begin{bmatrix} \frac{0,5z - 1}{(z - 0,3)(z - 0,5)} \\ \frac{-z + 0,725}{(z - 0,3)(z - 0,5)} \end{bmatrix} = \begin{bmatrix} \frac{4,25z}{z - 0,3} - \frac{3,75z}{z - 0,5} \\ \frac{-2,125z}{z - 0,3} + \frac{1,125z}{z - 0,5} \end{bmatrix}.$$

Next, using the z-transformation tables, we get $x_{ce}(k) = \begin{bmatrix} -3,75 \cdot (0,5)^k + 4,25 \cdot (0,3)^k \\ 1,125 \cdot (0,5)^k - 2,125 \cdot (0,3)^k \end{bmatrix}$.

For verification, let 's put $k = 0$ here, then $x_{ce}(0) = [0,5 \quad -1]^T$. Since the forced component of the solution will be zero at $k = 1$ (since there are no δ functions in the input effect), $x_{ce}(0)$ should be equal to the given vector x_0 . In our case, this condition is obviously fulfilled.

Let 's move on to the definition of the forced component $x_{bhh}(k)$, z -the image of which is determined by the expression.

$$x_{bhh}(z) = \begin{bmatrix} z & 1 \\ -0,15 & z - 0,8 \end{bmatrix} \begin{bmatrix} 1 \\ 0,5 \end{bmatrix} \frac{0,8z}{(z - 1)^2 (z - 0,3)(z - 0,5)}$$

or

$$x_{bhh}(z) = \begin{bmatrix} 0,8z + 0,4 \\ 0,4z - 0,44 \end{bmatrix} \frac{z}{(z - 1)^2 (z - 0,3)(z - 0,5)}. \quad (17)$$

As above, we decompose into the simplest fractions the corresponding ratios in (17), i.e.

$$\frac{Az + B}{(z - 1)^2 (z - 0,3)(z - 0,5)} = \frac{C}{(z - 1)^2} + \frac{D}{z - 1} + \frac{K}{z - 0,3} + \frac{L}{z - 0,5}.$$

Since there is a multiple pole ($z = 1$) here, it is impractical to apply formulas similar to (13). In this regard, we will find additional factors for each fraction and compose a system of algebraic equations of the following form:

$$\begin{bmatrix} 0,15 & -0,15 & -0,5 & -0,3 \\ -0,8 & 0,95 & 2 & 1,6 \\ 1 & -1,8 & -2,5 & -2,3 \\ 0 & 1 & 1 & 1 \end{bmatrix} \begin{bmatrix} C \\ D \\ K \\ L \end{bmatrix} = \begin{bmatrix} B \\ A \\ 0 \\ 0 \end{bmatrix} \quad (18)$$

This system is obtained by equating coefficients with the same degrees in the numerator of the right and left parts of equality (17), after bringing its right part to a common denominator. It is

written by substituting the coefficients of additional multipliers for each term in the right part (17) into the corresponding columns of the matrix in the left part of the system (18).

Conclusion. One of the key elements of optimal control of variable systems is the definition of an objective function that reflects the required optimality criteria, such as minimizing costs, maximizing efficiency or achieving a certain level of productivity. Then, based on the system model and taking into account constraints, various optimization methods are used to find optimal control actions, and also related to issues of safety, reliability and stability [6]. It is important to take into account the possibility of failures, errors or external influences and develop management strategies that ensure the stability of the system, minimize potential risks and protect against undesirable situations [7].

Optimal control of variable systems in the dynamic spectrum is a complex and multifaceted field of research that plays a key role in automation and has wide application in various fields of human activity. Automation, as the science of automatic control and control of systems, strives to ensure the optimal operation of the system, taking into account the set goals, limitations and conditions.

The application of optimal control of variable systems in automation also faces a number of difficulties and challenges. For example, the need to take into account uncertainty and noise in the system, changing operating conditions, non-linearity and complexity of models. In addition, the computational complexity of optimal algorithms can be high, requiring efficient methods and high-performance computing systems [8].

It is necessary to delve into various optimization methods, adapt them to the specific requirements of specific systems, and develop new approaches, taking into account the development of technologies and the emergence of new challenges. This will make it possible to achieve more efficient and sustainable management of variable systems and apply them in various fields.

REFERENCES

- [1]. Vashchenko, G. V., Novikov E.A. *Parallel implementation of the explicit Euler method with control of the accuracy of calculations*. Journal of the Siberian Federal University. Series: Mathematics and Physics, 2011, Vol. 4, No. 1, pp. 70-76. – EDN NCBQKR.
- [2]. Shornikov, Yu. V. *Stability analysis of explicit Runge -Kutta methods in the ISMA instrumental environment*. Problems of Informatics. 2009. – № 2(3). – Pp. 42-51.
- [3]. Tsitouras, C. (2007). *Runge–Kutta interpolants for high precision computations*. Numerical Algorithms, 2007, 44, pp. 291-307.
- [4]. Gorozhankin, S.A., Shitov, A.A., Savenkov N.V. *Methods for approximating the dependencies of several variables in the MS Excel and Mathcad software environment*. Scientific and Technical Bulletin of St. Petersburg State Polytechnic University. Computer science. Telecommunications. Management, 2016, № 3(247), pp. 35-47. – DOI 10.5862/JCSTCS.247.4. – EDN WZRGKT.
- [5]. Medvedev, A.V., Gorodetskaya, O.Y. *Modeling of optimal development of the region in the system of economic relations of the Russian Federation*. Chronoeconomics, 2017, № 4(6), pp. 27-30.
- [6]. Artemyev, V.S., Savostin S.D. *Analytics and methods of mathematical modeling of artificial intelligence in automation of control and testing*. Agrarian Science - 2022: Materials of the All-Russian Conference of Young Researchers, Moscow, November 22-24, 2022. – Moscow: Russian State Agrarian University - Moscow Agricultural Academy named after K.A. Timiryazev, 2022, pp. 340-343.
- [7]. Artemyev, V.S., Savostin S.D. *Automated resource security management systems in digitalization issues*. Agrarian Science - 2022: Materials of the All-Russian Conference of

- Young Researchers, Moscow, November 22-24, 2022. Moscow: Russian State Agrarian University, Moscow Agricultural Academy named after K.A. Timiryazev, 2022. pp. 344-347
- [8]. Artemyev, V.S., Savostin S.D. *Automation of methods and algorithms of information and analytical systems*. Vavilov readings - 2022: Collection of articles of the International scientific and practical Conference dedicated to the 135th anniversary of the birth of Academician N.I. Vavilov, Saratov, November 22-25, 2022. – Saratov: Limited Liability Company "Amirit", 2022. – pp. 639-642.
- [9] Debela, H.G. and Duressa, G.F. *Exponentially fitted finite difference method for singularly perturbed delay differential equations with integral boundary condition*. Int. j. eng. appl. sci., 2019, 11, pp. 476–493.
- [10] Debela, H.G. and Duressa, G.F. *Accelerated fitted operator finite difference method for singularly perturbed delay differential equations with non-local boundary condition*. J. Egyptian Math. Soc., 2020, 28, pp. 1–16.
- [11] Debela, H.G. and Duressa, G.F. *Uniformly convergent numerical method for singularly perturbed convectiondiffusion type problems with nonlocal boundary condition*. Int J Numer Methods Fluids, 2020, 92, pp. 1914–1926.
- [12] Kumar D. and Kumari P. *A parameter-uniform collocation scheme for singularly perturbed delay problems with integral boundary condition*. J. Appl. Math. Comput., 2020, 63, pp. 813–828.
- [13] Sekar, E. and Tamilselvan, A. *Singularly perturbed delay differential equations of convectiondiffusion type with integral boundary condition*. J. Appl. Math. Comput., 2019, 9, pp. 701–722.
- [14] Sekar, E. and Tamilselvan, A. *Third order singularly perturbed delay differential equation of reaction diffusion type with integral boundary condition*. J. Appl. Math. Comput. Mech., 2019, 18, pp. 99-110.
- [15]. Gorodetskaya, O.Y., Gobareva, Ya. L., Medvedev, A.V. *Forecasting of financial markets using a convolutional neural network*. Problems of Economics and legal practice. 2021, Vol. 17, No. 3. pp. 65-72. – EDN NSUFLT.
- [16]. Sekar, E. Tamilselvan, A. *Finite difference scheme for third order singularly perturbed delay differential equation of convection diffusion type with integral boundary condition*. Journal of Applied Mathematics and Computing, 2019, №61, pp. 73–86.
- [17]. Selvi, P. A. and Ramanujam, N. *A parameter uniform difference scheme for singularly perturbed parabolic delay differential equation with robin type boundary condition*. Applied Mathematics and Computation, 2017, №296, pp. 101–115.
- [18]. Amiraliyev, G. M., Amiraliyeva, I. G., and Mustafa, K., *A numerical treatment for singularly perturbed differential equations with integral boundary condition*, Applied Mathematics and Computation, 2007, №185, pp. 574–582.
- [19] Ansari, A.R., Bakr, S.A. and Shishkin, G.I. *A parameter-robust finite difference method for singularly perturbed delay parabolic partial differential equations*. Journal of Computational and Applied Mathematics, 2007, №205, pp. 552–566.

Received: 21.10.2022

Accepted: 15.03.2023



STRUCTURAL SYNTHESIS OF SERIAL SPHERICAL MANIPULATORS

Allahverdi ALAKBAROV

Department of Mechatronics and Machine Design of Azerbaijan Technical University, Baku, Azerbaijan

E-mail: allahverdi.elekberov@aztu.edu.az

Abstract: Serial manipulators are a serial of links connected by joints. The manipulator is called serial, because the drives of this manipulator are arranged in series, one after the other. Most often, the drives of the sequential manipulator are located on jointes or are coordinated with the joint. All links, the base, as well as the executive link, make up the kinematic chain of the manipulator. Serial manipulators have a large working area, it is much larger than the working area of parallel manipulators, which allows them to work with large parts, which undoubtedly increases the area in which the manipulator is capable of working.

Mass-produced robots typically have six joints because at least six degrees of freedom are required to place a controlled object in an arbitrary position and orientation in the robot's workspace. The inverse kinematics of sequential manipulators with six rotary joints and with three consecutive intersecting joints can be solved in closed form, i.e. analytically. This result had a huge impact on the design of industrial robots.

This section provides a unified work for the calculation of the mobility and constraints in a general over constraint spherical manipulators based on spherical serial manipulator plus the different spherical structural groups with two, three and four classes. The results of the section can be considered by knowledges of structural groups with general constraint three constructed to the serial spherical manipulator with 3DoF. The 3DoF serial spherical manipulators represent as a series of 1DoF revolute joints with the axes intersecting in the center of sphere. Three illustrative examples showcasing the method are presented.

Keywords: *Serial spherical manipulator, end effector, spherical structural groups, structural synthesis, mobility analysis.*

Introduction. Serial spherical manipulators are made an one base link and end effector link connected by the kinematic chains with three revolute joints with the axes intersecting in the center of sphere. The mobility of serial robotic system indicates the number of independent actuators. If mobility $M = 0$ of spherical kinematic chains we will get a simple spherical structural group of second class with $n = 2$ and $p_1 = 3$. By the same way we will get spherical structural groups $n = 4$, $p_1 = 6$ (third and fourth classes). Class of spherical structural groups describe the number of joints on platforms and by the number of joints on the closed loop.

In [1;2] the mobility number is characteristic of an independent loop $L = C - B$, where B number of platform and $C = C_l + C_b + C_{jb}$ is sum of legs, branches and joints between two platforms. Various analytical methods are used to calculate the mobility λ of manipulators using constraint screw theory [3]. The matrix notation was introduced in [4] represent mobility. Structural synthesis of same classes manipulators with configurable platform has been investigated in [5]. Recently, the analytical and numerical calculation of the mobility of over constraint manipulators with reconfigurable end-effectors has been done in [6].

Structural formulas for structural synthesis and analysis of robot manipulators. This section provides a unified frame framework for the calculation of the mobility and number of independent loops in a spherical serial manipulators of second, third and fourth classes. This results may be considered as known, but present framework provides the necessary background for the structural synthesis of complex serial manipulators.

Allahverdi ALAKBAROV
Structural synthesis of serial spherical manipulators

A general serial spherical manipulator comprises by three moving link and one fixed leg. The motion of end-effector will displaced on the face of sphere. The three main types of 1-DoF joints are revolute joints with the directions intersecting in the senter of sphere, so

$$M = \sum_{i=1}^j f_i = 3 \quad \text{it means} \quad \begin{matrix} \text{---} \\ \text{---} \\ \text{---} \end{matrix} \text{---} \text{---} \quad (1)$$

where: $j=3$, brakes “()” – represents the intersection directions of kinematic pairs; “---” – fixed frame; --- - end effector.

As were showed in [2] the number of independent loops is equal:

$$L = j_b - B - C_b - C_{j_b} \quad (2)$$

where:

B – the number of mobile platforms;

j_b - the total number of joints on the mobile platforms;

C_b - the total number of branches between mobile platforms;

C_{j_b} - the total number of joints between mobile platforms.

The total number of joints on the mobile platforms can be also describe a

$$j = C_l + 2C_b + 2C_{j_b} \quad (3)$$

where: C_l - the total number of legs.

Combining equations (2) and (3) we will get the total number of independent loops in the following form:

$$L = C - B \quad (4)$$

where:

$C = C_l + C_b + C_{j_b}$ is the sum of numbers legs, branches and joints between platforms.

It is known that the position and orientation of the rigid body in space can be described by parameter $\{\lambda_k\}_1^6$. In the same time the general constraint for motion of the rigid body in space can be described by parameter $\{d_k\}_0^5$. So, the general constraint for motion of rigid body in space can be written as follow:

$$\{\lambda_k\}_1^6 + \{d_k\}_0^5 = \lambda + d = 6 \quad (5)$$

It is known that the position and orientation of the couple “ k ” in each closed loop it is equal to the motion parameter λ_k of close loop, so for “ k ” structural group we will have

$$\sum_{i=1}^j f_i + \sum_{k=1}^L \lambda_k = 0 \quad (6)$$

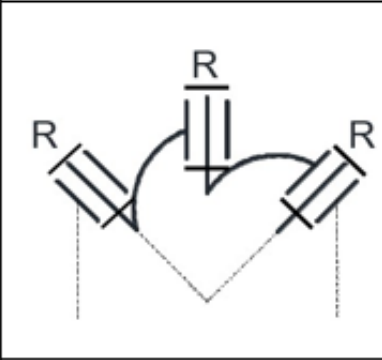
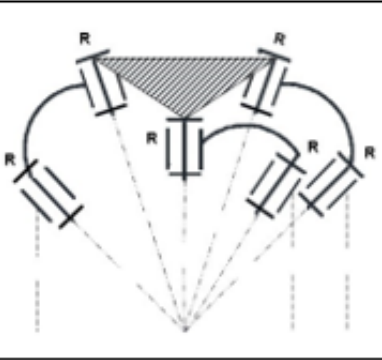
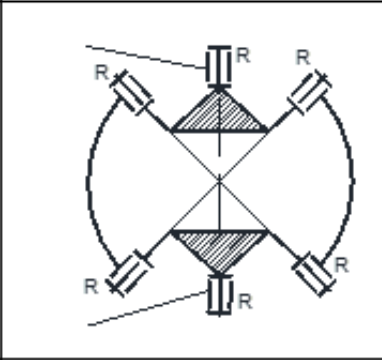
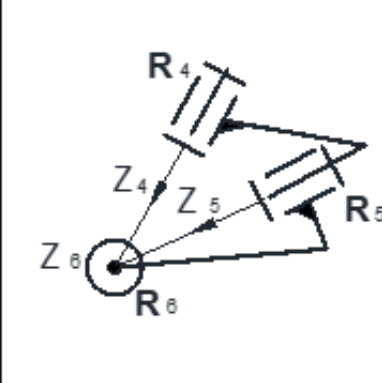
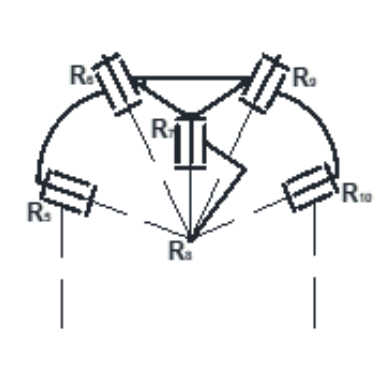
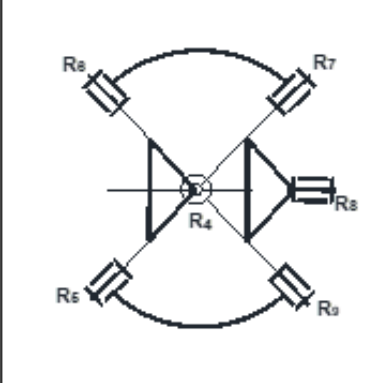
When the displacement variables in structural groups correspondence with DoF of joint in serial manipulators and combining equations (6) and (1) we will get the structural formula for the multiloops serial manipulators as follows:

$$M = \sum_{i=1}^j f_i - \lambda L \quad \text{or} \quad M = \sum_{i=1}^j f_i - (6 - d_k)L \quad (7)$$

The above equations (1), (6) and (7) show that basically the mobility number of serial multiloop manipulator is associated with the constraint of an independent loop.

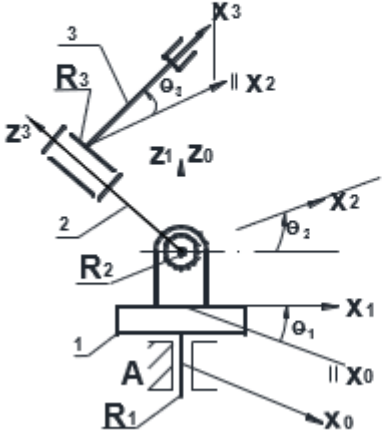
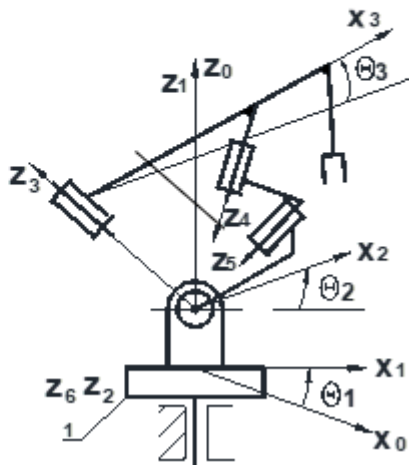
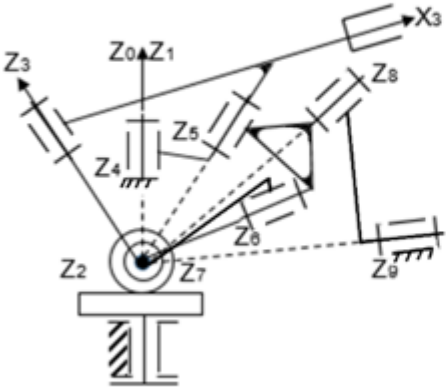
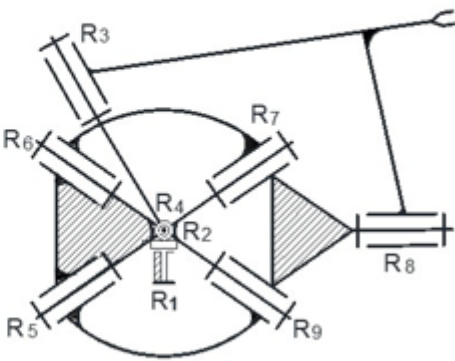
New serial spherical multiloop manipulators. The classic geometrical structural synthesis for the spherical groups with mobilities $M=0$ are illustrated in Table 1. It is introduced the three structural spherical groups (RRR) , $(R-RRR-R)$ and $((R < \begin{smallmatrix} R & R \\ R & R \end{smallmatrix} > R))$ from space $\lambda = 3$ with numbers of independent loops $L(1,2,2)$, number of moving link $n(2,4,4)$, number of legs $c_l(2,3,2)$, number of branch $c_b(0,0,2)$ and number of platform $B(1,1,2)$ respectively.

Table 1. Kinematic chains of spherical structural groups

Second class of structural group	Third class of structural group	Fourth class of structural group
$M = 0, \lambda = 3, L = 1, n = 2$	$M = 0, \lambda = 3, L = 2, n = 4$	$M = 0, \lambda = 3, L = 2, n = 4$
		
1	2	3
$B = 1, c_l = 2, R = 3,$ (RRR)	$B = 1, c_l = 3, R = 6,$ $(R - R, R - R, R - R)$	$B = 2, c_l = 2$ $c_b = 2, R = 6$ $\begin{bmatrix} R - R & & \\ R & & R \\ & R - R & \end{bmatrix}$
		
4	5	6

So, the first two spherical structural groups are called second and third classes on the base of platform legs (Table 1(1, 2)), by the third spherical structural group is called fourth class on the base of links number of closed loop (Table 1(3)). The structural synthesis process is to design a new spherical serial manipulators with closed loops structures (Table 2). The process are transform the serial spherical (RRR) manipulator to the serial spherical multiloop manipulators by adding the spherical structural groups of second, third and fourth classes (Table 2).

Table 2. Structural synthesis of spherical manipulators

Structure of serial spherical manipulators $M = 3, \lambda = 3, d = 3$	Structures of serial multiloop spherical manipulators $M = 3, \lambda = 3, d = 3$; Second class
	
1	2
$M = 3, \lambda = 3, d = 3$; Third class	$M = 3, \lambda = 3, d = 3$; Fourth class
	
3	4

In order to construct a serial spherical multiloop manipulators should be consistent with the following conditions:

- Creating simple over constraint spherical structural groups.
- Class spherical structural groups are defined by the number of independent points on the moving platforms (two, three-Table 1.1 and 1.2) and by the number of moving links in the closed spherical loops (four-Table 1.3).
- Create new serial spherical multiloop manipulators by added spherical structural groups to the serial spherical manipulators.
- Computer-aided spherical structural synthesis.
- Generation of the branches and legs of spherical manipulators by describing the axes of kinematic pairs directed through the center of sphere.

Conclusion Spherical structural synthesis is performed for serial spherical multiloop manipulators the structural groups of second, third and fourth classes. One of the fundamental area

of the robotic science “Structural synthesis of robotic system” is applied and developed for the serial spherical multiloop manipulators with general constraints three. A new procedure for structural synthesis of multiloop serial spherical manipulator are proposed.

Several spherical manipulators with general constraint three are given. Using this study any designer can develop the structural synthesis problem of serial spherical multiloop manipulators.

REFERENCES

- [1] Freudenstein, F., Alizade, R. *On the degree of freedom of mechanisms with variable general constraint. IV World IFToMM Congress*, England, 1975, pp. 51-56.
- [2] Alizade, R., Bayram, C. *Structural Synthesis of parallel manipulators*. IFToMM Mechanism and Machine Theory, 2004, 39, pp. 857-870.
- [3] Dai, J.S., Huang, Z., Lipkin, H. *Mobility of over constrained parallel mechanisms*, Journal of Mechanical Design, 2006, 128, pp. 220-229.
- [4] Lambert, P., Herder, J. *Mobility analysis of non series-parallel mechanisms*. New Trends in Mechanisms and Machines Science, Springer, 2012, pp. 63-71.
- [5] Kong, X., Jin, Y. *Type synthesis of 3DoF multi-mode translational spherical parallel mechanisms with lockable joints*. Mechanism and Machine Theory, 2016, Volume 96, Part 2, pp. 323-333.
- [6] Alizade, R., Temirov, A., Alakbarov, A. *Engineering design as key area of technical background for engineers*. Machine Science, 2022, №1, pp. 10-13.
- [7] Fatih, C.C, Hayrettin, S. *Real time controlled two DoF five bar robot manipulator*. Machine Science, 2022, №1, pp. 14-22.
- [8] Lambert, P., Cruz L.D., Bengales, C. *Mobility of overconstrained parallel mechanisms with reconfigurable end-effectors*. IFToMM Mechanism and Machine Theory, 2022, 171, pp. 1-20.

Received: 24.02.2023

Accepted: 15.05.2023



RESEARCH OF THE INTERACTION IMPACT FEATURES OF THE COTTON WICKS WHILE HITTING THE GRATES IN THE COTTON GINNING MACHINES

Husnu KARIMOV

Department of Light Industry Engineering and Design of Azerbaijan Technological University, Ganja, Azerbaijan

E-mail: kerimov_husnu@mail.ru

Abstract: During the cleaning process of the raw cotton, in the saw drum and grate network zone of the cotton ginning machines, the cotton mass is being subjected to the mechanical impact. At this moment, when the cotton wicks hit the grates, the cotton seed is mechanically being damaged and free fibers are being formed. When the cotton seed is mechanically damaged, its maturity decreases, and the formation of free fibers reduces the curvature/spinning ability of the fiber. Keeping the natural quality indicators of raw cotton and taking into account its physical and mechanical features, there is a great demand to conduct theoretical studies and researches for designing new machines. Taking into consideration the elastic properties of cotton wicks during their impact on the grate, the formulas revealing the movement speed of wicks and recovery of wicks coefficient were determined.

The article reveals the possibility of prevention the cotton elements from damage by determining the interaction characteristics of cotton wicks with grates and by adjusting the technological parameters to the equipment before processing.

Keywords: *cotton wick, extraneous impurities, grate, deformation, impact force*

Introduction.

Since the rate of raw cotton harvesting with the help of machines increases with every passing year, the amount of extraneous impurities in it also increases. This complicates the work of ginning machines. There is a need to increase the cleaning effect of the ginning machines in the flow line, no matter those working with batteries and/or the equipment continuously connected to the technological process [1]. Separation of large impurities (such as lint, stalks, stems, thorn, stem fractures etc.) that are in active contact with cotton fibers requires greater responsibility. The main cleaning section of the ginning machines, used for this purpose is called the saw drum-grate network zone [2]. Keeping the natural quality indicators of raw cotton and taking into account its physical and mechanical features, there is a great demand to conduct theoretical studies and researches for designing new machines [8, 9, 11]. The solution of this issue could be possible as a result of the joint effort of scientific research project organizations, as well as machine-building and cotton processing enterprises.

Materials and methods. At all stages of the regulated technological process, the raw cotton is exposed to shock loads, which leads to the mechanical damage of the cotton wicks and the formation of free fibers. As a result of it its maturity and the curvature/spinning ability of the fiber decrease [7, 10].

The impact impulse in the process of ginning/purifying the raw cotton was experimentally studied in the article [4]. In this work the interaction of circular, trapezoidal and elastic working surface grates with fibrous mass was studied in a wide range.

It was shown in research work [5] that the interaction of raw cotton and grates according to a number of factors was a complex process and depended on the reaction of grates during the contact of extraneous mixtures with grates. It was also determined that the friction of the fiber with the surface of the grates activates the fibrous layer, which leads to the weakening of the connection of the external mixtures with the fiber. Grates with different profiles were studied in this work.

It is possible to determine the interaction characteristics of cotton wicks with working parts of the ginning machines, and to prevent damage to cotton elements by adjusting the technological parameters to the equipment before starting the cleaning process.

According to the reporting scheme of the impact process in the grate - wick system (Fig. 1), some relations of the impact process of cotton wicks on the grates were determined.

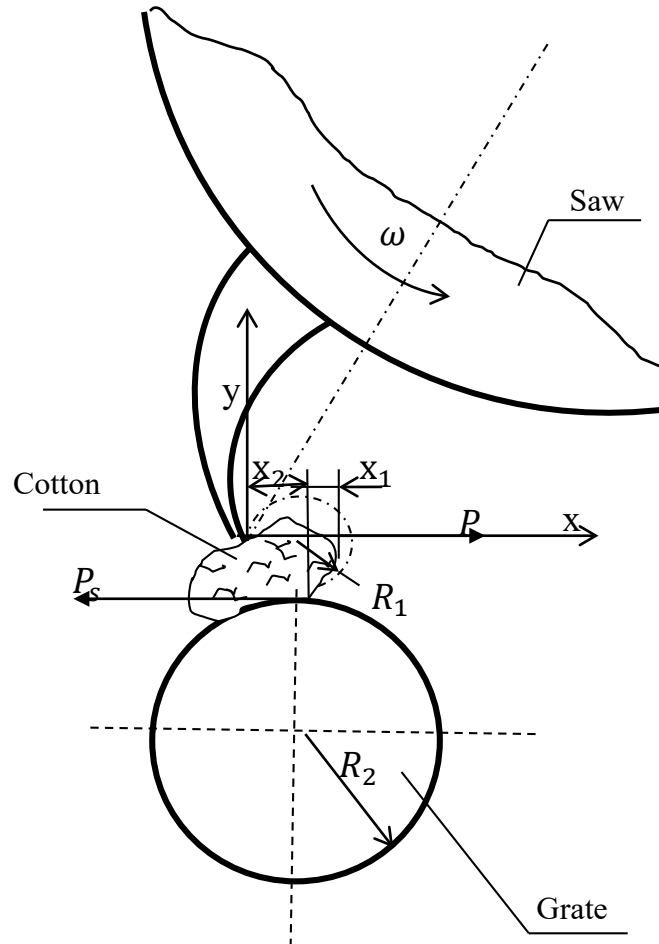


Figure 1. Reporting scheme of the impact process in the grate-wick system

When looking at the process of mutual impact of cotton wicks with grates, we can observe that at certain critical values of impact loads, elastic and plastic deformations occur in the fibrous part of the wick, which means that the process does not obey Hers's law, i.e., it cannot be characterized by Hers's law.

According to the empirical law of Herstner [3], when the elasticity exceeds the limit, not depending on each other when loading, the increasing x deformation consists of x_1 elastic and x_2 plastic components.

In theoretical studies, it is considered that the elastic deformation depends on Hers's law, and the plastic deformation depends linearly on the contact force:

$$x = x_1 + x_2 = kP^{\frac{2}{3}} + m(P - P_s) \quad (1)$$

where k – is the coefficient characterizing the material (depends on the material property and the configuration of the deformable element); m - is the empirically determined coefficient; P - contact force; P_s – is the value of this force when plastic deformations occur.

In the static loading, the value of x approximation is as follows:

$$x = kP^{\frac{2}{3}} + mP_{\max}$$

where $mP_{\max} = x_{2\max}$ is the maximum plastic deformation.

In the process of unloading, the value of approximation due to plastic deformations remains unchanged. We can determine the k coefficient by equating the inverse coefficient β of the Hers formula.

$$P = \beta x^{\frac{3}{2}}$$

Where

$$\beta = \frac{4}{3} \frac{q_k}{(\delta_1 + \delta_2)\sqrt{A+B}}$$

where q_k is the coefficient; δ_1, δ_2 – elastic constants of objects; A, B – are the coefficients determining the geometry of the colliding surfaces.

For a spherical wick model with radius R_1 , $A = \frac{1}{2R_1}$ and for a grate with radius R_2 we can use

$$B = \frac{1}{2} \left(\frac{1}{R_1} + \frac{1}{R_2} \right)$$

Since the coefficient m cannot be determined analytically, the plastic deformation of the components is calculated experimentally. However, if it is not possible to facilitate the solution of this issue with a certain theoretical approach, it can be solved experimentally.

In the general case, expression (1) can be presented as follows:

$$x = bP^n \tag{2}$$

Where b and n are experimentally determined coefficients.

The deformation work in the contact zone could be as follows:

$$A = \int_0^x P(x) dx = \int_0^x x^{\frac{1}{n}} dx = \frac{1}{\frac{1}{n} + 1} = \frac{n}{1+n} Px$$

Since the total work equals the voltage energy.

$$\frac{1}{1+n} P_{\max} x_{\max} = U_{\text{д}} = \Delta T \tag{3}$$

where ΔT is the kinetic energy spent on deformation of the wick during impact [3].

$$\Delta T = \frac{m_n}{2} \left[O_0^2 - O_1^2 \left(1 + \frac{m_{np}}{m_{\text{д}}} \right) \right]$$

If we make transformations in the formula (3), we would get;

$$\frac{n}{1+n} \cdot \frac{x^{\frac{1+n}{n}}}{b^{\frac{1}{n}}} = \Delta T$$

where

$$x_{\max} = \left[\frac{\Delta T b^{\frac{1}{2}} (Hn)}{n} \right]^{\frac{1}{1+n}}$$

Accordingly, the maximum value of the contact force during compression would be the following:

$$P_{\max} = \frac{1}{b^{\frac{1}{2}}} x^n \left[\frac{\Delta T (1+n)}{bn} \right]^{\frac{1}{1+n}}$$

If we integrate the impact equation twice [3], we would write

$$\frac{\partial V}{dt} = \frac{\partial^2 x}{\partial t^2} = -\frac{1}{m_n} P(x)$$

Here, if we write the known values instead of x_{\max} and P_{\max} , we would get:

$$\frac{2P_{\max} \tau}{m_{uc} V_0} = \frac{1+n}{n} F_1(n) = F_2(n)$$

there, F_1 and F_2 are unique criteria of dynamic similarity during the impact. If we take into consideration the ready values of these functions [3], we would write

$$\frac{V_0 \tau}{x_{\max}} = F_1(n)$$

where τ - is the time of the blow/kick in the active phase.

And in the passive phase, elastic deformations are being restored:

$$x_{\max} = bP^n = (x_1)_{\max} + (x_2)_{\max} = b_1 P^{n_1} + (x_2)_{\max}$$

In the passive stage, the equation of deformation would take the following form:

$$\frac{\partial^2 x}{\partial t^2} = \frac{1}{m_{uc}} P(x) = \frac{1}{m_{uc} b_1^{\frac{1}{n_1}}} [x - (x_2)_{\max}]^{\frac{1}{n_1}}$$

If we integrate the equation and make certain transformations, we would get

$$\tau_y = \tau + 1,65 P_{\max}^{\frac{1}{6}} \sqrt{m_{uc} b}$$

where τ_y - is the precise impact time.

At the end of the passive phase, the movement speed of the wick during the impact on the grate would be:

$$V_2 = P_{\max}^{\frac{1+n_1}{2}} \sqrt{\frac{2b_1 n_1}{m_{uc} (1+n_1)}}$$

Thus, the recovery coefficient would be determined as follows:

$$\beta = \frac{V_2}{V_0} = P_{\max}^{\frac{1+n_1}{2}} \sqrt{\frac{l_1 n_1}{T_0 (1+n_1)}}$$

If we also take into account the aerodynamic resistance during the impact on the grates, we can take 0.2 [6].

During the report, the value of the n index [6] (dynamic characteristic coefficient) can be taken practically the same for elements of the same shape made of different materials but deformed. The dynamic characteristic coefficient (n) at the speed limit $v = 1.62\text{--}31.0$ m / s does not depend on the deformable elements of the material and the impact speed.

The coefficient b depends on the properties of the material and the configuration of the deformable elements and is determined as follows [3].

$b = \frac{b_{st}}{\varphi^{1+n}}$ where φ was the dynamism coefficient and $\varphi = 1.3$ is taken. b_{st} – is being determined experimentally at static voltage.

The values of the quantities n and b can also be found from the relation (3), in this case the work of the deformation energy and the kinetic energy of the falling wick are being equalized, provided that one of these equations is determined experimentally or according to the values of V_0 and P [4] and taking from the research work [5], it can be solved by a system of two-variable equations.

Conclusions.

1. When studying a number of characteristics of the impact of the cotton wicks on the grates, it was determined that it is necessary to determine the specific values of these characteristics.
2. Taking into consideration the elastic properties of cotton wicks during their impact on the grate, the formulas revealing the movement speed of wicks and recovery of wicks coefficient were determined.
3. It was determined that it is possible to prevent the damage of cotton elements by determining the interaction characteristics of cotton wicks with grates and by adjusting the technological parameters to the equipment before starting the processing.

Acknowledgements.

This work was carried out under the guidance of Doctor of Technical Sciences, Professor Fazil Ali oglu Valiyev.

REFERENCES

- [1]. Lugachev, A. E., Salimov, A. M., *Primary processing of cotton*, Tashkent, 2007, p. 131.
- [2]. Miroshnichenko, G.D. *Fundamentals of designing machines for primary processing of cotton*. Tashkent: Ukutuvchi, 2008, p. 241.
- [3]. Batuyev, G. C. and others. *Engineering methods for studying impact processes*. Mechanical engineering, 2007, p. 240.
- [4]. Burnashev, R.Z., Lugachev, A.E. *Experimental study of shock impulses in the process of cleaning raw cotton and fibers*. Cotton industry. 2009, No. 5. pp. 8-9.
- [5]. Burnashev R.Z., Lugachev, A.E., Fazylov S. *Experimental study of the shock interaction of raw cotton bats with the grate of a coarse litter ginning machine*. Cotton industry, 2010, No. 1.
- [6]. Burnashev, R. Z., Miroshnichenko, G. I. *Determination of the coefficient of dynamic stiffness of the raw cotton bat when it hits the grate*. Cotton Industry, 2011, No. 4.
- [7]. Kerimov, U. G., Veliyev, F. A., Influence of the grate profile on the intensity of the release of weed impurities, Young Scientist No. 9 (11), Moscow, 2016, pp. 496-500.
- [8]. Valiyev, F.A., Karimov, H.G., *Grates for cleaning raw cotton network*, F 2020 No. 0023, Patent for utility model, Republic of Azerbaijan, Baku, 2020, p.8.
- [9]. Karimov, H., Mustafayeva, E., Jafarov, E., Safarova, T., Veliyev, F., *Theoretical research of the grate-saw cleaner of a large litter of the mounted type*. EASTERN EUROPEAN journal of enterprise technologies, 2021 2/7 (110), pp. 74-84.

- [10]. Korabelnikov, R. V., Ibragimov, Kh. I., *A complex indicator of the impact of a cotton cleaner on raw cotton during the cleaning process*. Technology of the textile industry. 2008, No. 3, pp. 35-38.
- [11]. Tashpulatov, D. S. Djuraev, A. D., Plekhanov, A. F. *Grates oscillations on elastic supports with nonlinear rigidity with random resistance from cotton-raw maternity*. European Sciences review Scientific journal. 2018, № 5-6. pp. 353-355.

Received: 16.10.2022

Accepted: 25.02.2023



ANALYSIS OF TRACTION TRANSMISSION OF RAILWAY VEHICLES AND THEIR DYNAMIC CHARACTERISTICS

Ilham HUSEYNOV

Department of Mechatronics and Machine Design of Azerbaijan Technical University, Baku, Azerbaijan

E-mail: ilham.huseynov@aztu.edu.az

Abstract: In the article, traction transmissions of railway vehicles, which are an important component of the transport industry, are studied. Dynamic events in the functional chain, as the main factors that ensure the structural condition of the main parts of the mechanical system, the longevity of the system, effective measures to improve the operation of the service, effective measures to improve the performance of the structures, the operation of improved structures, the in-depth determination of maintenance and repair technologies, as well as the service outstanding features. The relevance of technical quality assessment is justified by the development of an innovative model. The condition, construction and operation of modern traction drives are explained. Experimental studies are underway and have strong implications for transmission control. With the device that checks the possibilities of using defectoscopic methods, the cases that caused rejections were determined.

Keywords: *Railway, train, locomotive, wagon, innovative, transmission, reducer, dynamics, model, gear.*

Introduction. Demands for world logistics cargo and transportation are increasing every year, the demand also ensures the provision of economic services at a high level in accordance with modern technologies, and ensures that the energy systems of different countries provide each other. requires tools that satisfy the principles of flexibility. One of the bases in logistic transportation is railway [1,2]. Ensuring that railway vehicles comply with the above-mentioned requirements is related to the reliability and operation of their traction transmissions and other mechanisms. A complete study of the dynamic characteristics of the drag transmission and the development of a stable model have not yet been achieved. Thus, narrow transition significantly complicates the problems of creating a reliable node that can be exploited for a long time, since it is "inherently" conflict-free from the beginning. It is no coincidence that drag transmission schemes and constructions are constantly being modified and improved, but despite this, it remains one of the weakest nodes. Comparative calculations of different types of dart transmissions based on scientifically based mechanical-mathematical models make it possible to visually reconcile different dart transmission options under the same conditions and demonstrate their features, advantages or disadvantages [3].

Traction transmission is a set of devices that serve to convert a certain type of energy into movement to overcome resistance. The function of converting energy directly into work is performed by the executive body of transport - the driver of the vehicle.

In addition to the mover, the draft transmission, which converts electrical energy into mechanical work, includes a draft reducer, a draft engine, a converter and regulating devices (Fig. 1).

Since the **traction motor** serves to convert electrical energy into mechanical energy, it is included in the composition of both electrical and mechanical parts.

The draft **reducer** ensures the transmission of power flow from the draft engine to the actuator. Dart transmission is the main element of the mechanical part of the transmission. As a rule, it is a complex mechanism that requires considerable costs during production, operation and maintenance. The dynamic events that occur in it are distinguished by their high intensity, and as a result, they can lead to a decrease in the general reliability of railway vehicles.

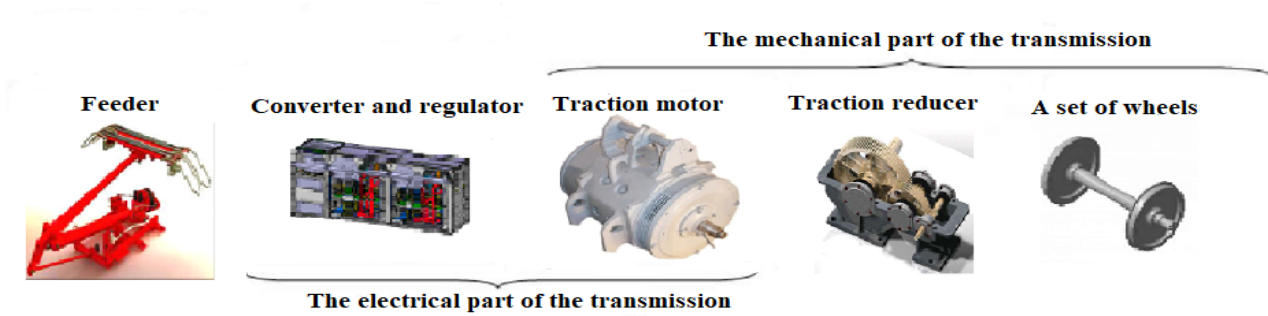


Figure 1. Structural diagram of traction transmission

Converters and regulators serve to convert the electrical energy received from the source to the type required for the selected thruster and to regulate the power flow.

A wheel is used as a driving force in the traction transmission of a traditional train of railways. Already there are contradictions in it that limit the parameters and constructive solutions of a number of elements of the locomotive and traction transmission in general. Indeed, such a mover realizes its traction force at the point of contact between the wheel and the rail. Its limit value is determined by the friction properties of the contact pair elements and their compression force. Therefore, the transfer of a large static load from the wheel to the rail is a prerequisite for achieving a significant traction force. This is practically done by giving the wheel the function of a support element and increasing the mass of the locomotive to ensure that the wheel is pressed against the rail with the necessary force. Such a solution is especially unfavorable for the transmission, such as the increase of the transported useless mass, the increase of the mass-dimension indicators of the moving parts, including the pair of wheels, and the fact that the main element of the transmission - the mover (in a space that is never straight-line due to the imperfection of the road) must follow the trajectory of the support element and its negative consequences are obvious. As a result, dynamic processes occur in the entire transmission system. It helps the dynamic loading of the transmission, and the wheel pair acts as a guide for the locomotive, and therefore interacts directly with the track in the transverse direction as well.

A lot of research works have been carried out related to the study of dynamic characteristics of mechanical systems. Let's take a look at some of them, for example: the author studied the effect of joint clearances on the dynamic characteristics of the machine drive by means of simulation [4], stiffness and damping of couplings during torsion, structural clearances, forced vibration of the system, as well as moments of inertia of the rotating masses in the control and driven arms of the transmission. taking into account the dynamic properties of machine transmissions are studied [5], taking into account the physico-mechanical properties and geometry of the elastomer, as well as the dynamic characteristics of the machine transmission, the influence of the damping ability of elastic couplings on temperature changes is studied [6], In this work, a supercapacitor (CSS_SC) single-phase traction power supply system is required to evaluate power system control and power quality management. In addition, a coordinated control strategy is introduced according to the operating mode, including traction, regenerative braking, peak shaving and valley filling. A simulation model was built in MATLAB/Simulink to check the feasibility of a system with dynamic work consumption [7], this document offers a simulation modeling method for application plans for digital twins, calibrated shake maps, and friction measurement calculation methods. The method is to enhance the potential of incorporating rate-dependent friction properties, co-simulation of a locomotive traction mechatronic system, and mechanical properties of wheel and rail materials measured in tensile tests. A number of operating conditions are simulated on a high-performance computing cluster, the resulting stress is then processed into calibrated shock heatmaps. The method clearly showed the effect of special operating conditions on obtaining a rail for a specific combination of single-rail materials configuration highways [8], The electrical dynamics of the locomotive traction motor and

its effect on the rail and car under transient wheel-rail contact conditions have not been thoroughly investigated. Such transient traction behavior may be more important to dynamic traction performance and road degradation (eg, corrugation, fatigue, wear, etc.) than steady-state behavior. To find out, detailed numerical simulations are conducted to investigate the locomotive multibody dynamic response to the change in AC and DC traction motor contact conditions, respectively. In particular, creep response, locomotive vibration, dynamic normal and traction forces are determined using the developed full-scale locomotive dynamics model. The model includes detailed AC and DC motor dynamics. Additional research was conducted to understand wear during and after changing friction conditions from dry to wet and from wet to dry[9].

The state of modern traction. In many parts of the world, especially in developed countries, modern railway vehicles are in operation. Among them, Stadler trains, new generation electric trains operated in our country, Alstom freight and passenger locomotives and others can be mentioned. Although the mentioned new generation vehicles are equipped with systems that meet modern standards, since they are new in operation, their operation characteristics have not been fully studied. As we know, the technical characteristics of railway vehicles are formed in their traction transmissions. In this regard, issues such as researching, evaluating and developing an innovative model of the technical level of dart transmission are particularly relevant[10].

The motorized bogie of STADLER electric trains of modern railway vehicles is an H-shaped frame equipped with wheel pair elements, tireless wheels, draft reducer and draft engine (Fig 2). The draft reducer is held on one side by means of a flexible coupling on the wheel pair shaft. On the other hand, the engine-reducer block is hung from the trolley frame by means of a holding mechanism. Pairs of wheels are connected to the frame by means of elastic springs and rubber-metal materials, so that the transmission of mutual forces can be softened to a certain extent. In modern trains, airbags are used to connect the carriage with the body. In case of airbag failure, additionally installed rubber supports act as a support. These rubber supports partially provide comfort, allow the movement to continue at low speed, prevent derailment and ensure the safety of the movement.

Two motors are installed in each carriage. The traction reducer transfers the engine shaft rotation frequency and torque to the wheel pair shaft by changing the gear ratio of the reducer. Braking of the stroller occurs when the brake discs are pressed against the wheels. Braking is carried out by means of four bending discs with linkage mechanisms and brake cylinders. Each axle is equipped with two brake mechanisms, one of which is spring-loaded. Pneumatic supports compensate for discomfort and unevenness caused by dynamic effects during movement. Traction and braking forces are transmitted from one trolley to another by means of a trailer equipped with a shock absorber mounted on the trolley.

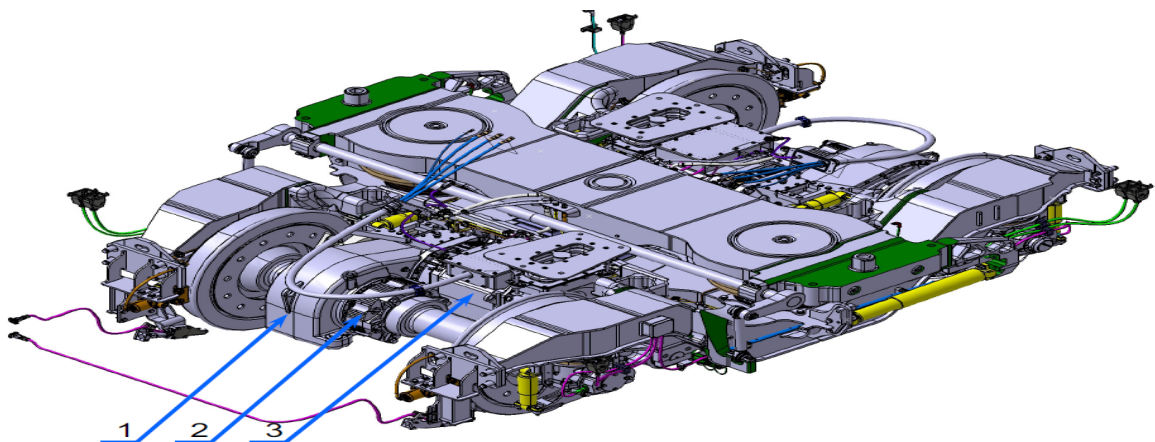


Figure 2. STADLER electric train carriage

Air cushions, elastic springs, anti-slip system, elastic side supports, and hydraulic supports system to suppress vertical and horizontal vibrations are installed in order to protect the trolley traction transmission of modern Stadler electric trains from dynamic effects. Oscillation along the

longitudinal axis is stabilized with the help of hydraulic shock absorbers. All systems are interconnected to ensure the safety and smooth operation of the train. The trolley is optimized for derailment resistance.

The traction motors are mounted on the carriages and are designed to drive and brake the wheel pairs through the traction reducer. Each motorized cart has two thrust motors, one for each axle. The figure below shows the MB200 and MB250 motor carriages (Fig 2). It is a three-phase asynchronous pulse converter motor according to the design of traction motors. It is externally cooled in open circuit.

The traction reducer connects the engine and the pair of wheels and performs a transmission function in the conversion of electrical energy into mechanical work. It is extremely difficult to increase the reliability of reducers, because they work under conditions of complex, multifactorial, multidirectional and variable influences. In this regard, economic utility should be taken into account when designing them. Modern STADLER electric trains use a two-stage traction reducer type GMK 2-58-495D (Fig 3). The reducer is connected on the one hand to the wheel pair shaft through a flexible coupling, and on the other hand to the motor through a diaphragm coupling. Thus, the motor shaft is the input shaft of the reducer, and the wheel pair shaft is the output shaft of the reducer. In addition, in order to ensure the minimum value of the number of steps and the distance between the centers, an intermediate shaft is installed on the body of the reducer, which rests on both sides. On the motor shaft, one driven cylindrical gear, one driven gear of the first stage and one driven gear of the second stage are placed on the intermediate shaft. block gear and one driven gear are placed on the shaft of the wheel pair. The reducer is lubricated in a closed environment. equipped with additional oil temperature and level controls. The figure below shows the traction reducer-engine block of STADLER trains [11].

Among the modern electric locomotives operated in our country, the latest model four-axle Az4-type passenger locomotives produced by the French company "ALSTOM" were investigated and the missing aspects were determined. On the basis of the proposed draft transmission, it is clearly possible to see the improvement of the technical level indicators due to the reduction of the metal capacity and the reduction of overall dimensions. In order to increase the speed of Az4 type passenger locomotives, the size of the large gear wheel was reduced by the manufacturer. As a result, it became necessary to use a parasitic gear to transmit the movement. This leads to excess metal capacity and reduced efficiency. The bogie of the AZ4 type locomotive is an H-shaped frame equipped with 2 drawbar transmissions and additional devices, and the drawbar transmission is two wheels, an engine shaft as a driving shaft, an intermediate shaft, and an engine with a pair of wheels as a driven shaft, one cylinder on each shaft being a spur gear, a two-stage cylindrical spur gear transmission is a mechanical system equipped with bushings and attachments[12].



Figure 3. STADLER electric train reducer-engine block

Functional requirements for traction. The operating conditions of the transmission are determined by three main groups of factors.

The first group of factors is related to the fulfillment of the main purpose of the thrust transmission, that is, the power flow received from the energy source is converted and transferred to the drive. At this time, the indicators that determine the loading of transmission elements are not

constant in terms of absolute value and time. Depending on the driving mode of the train, the power, torque and rotation frequency of the transmission can vary widely. Thus, at the moment of the train's movement, the gear transmission works in the mode characteristic of the so-called "slow-speed" transmissions - at low rotation frequency and high torques. During movement at maximum speed, the gear transmission operates in a mode typical of "high-speed" transmissions. All this depends on the optimal geometric dimensions of the tooth, the type of lubrication, etc. makes it difficult to choose.

In addition, it is also possible to change the direction of rotation and the direction of power flow during the working process of the thrust transmission. The first case is observed when the mechanical system changes the direction of movement, and the second case is observed during the transition from traction to electric braking. The continuous operation of the tooth, sometimes in the leading and sometimes leading mode, makes it especially difficult to work on its side surfaces.

The second group of factors is determined by the use of one of the main elements of the transmission - the engine as a supporting and guiding element of the mechanical system. In this regard, it is inevitable that the mover of the draft transmission and, above all, more or less elements related to the draft transmission are exposed to the vibrations given to the pair of wheels in vertical and horizontal directions by the rail.

The third group of factors is related to climatic conditions. If we look at all climate zones, we will see that the temperature range in which the railways that pass through all climate zones operate is characterized by the following indicators:

- absolute minimum – 54 °C;
- average perennial minimum – 47 °C (North-Siberian climate region);
- absolute maximum + 55 °C;
- average perennial maximum + 50 °C (Central Asian climate zone).

Traction motors and brake systems being unprotected from ambient temperature, as well as their own heat dissipation, can significantly increase the upper level of the operating temperature of the traction drive.

The deterioration of the working conditions of the moving train is also helped by the high level of vertical roughness caused by the structural characteristics of the track surface. On most Western European roads, it is accepted to "skip" the junctions of the right and left lanes. In this case, the unevenness of the joint is one-sided, and the shocks transmitted to the plane of the location of gears and bearings are much less than those affecting the wheels.

In the microatmosphere surrounding the transmission elements, there is always water, snow, dust, which consists of a large amount of abrasive and active chemical particles, and significant pressure changes caused by aerodynamic phenomena during movement at high speeds help these particles penetrate into the internal spaces. In addition, the drawbar transmission is one of the few nodes that does not allow visual observation of the locomotive both in motion and at rest. Constantly increasing traction power while maintaining overall dimensions dictated by the width of the railway and the diameter of the locomotive's wheels has led to the creation of constructions that use a high degree of materials and fill the allocated space, which in turn complicates the possibilities of sensory control (visual, acoustic, etc.). Thus, drag transmissions are not only stationary, but also work in much more difficult and especially complex conditions compared to the vast majority of transmissions in many other vehicles.

In such conditions, the requirements for traction drives are mainly thermal. The main one is based on providing fail-safe operation during operation, since there is no back-up of the traction drive and its failure practically leads to the failure of the locomotive and therefore the failure of the train. schedule. However, no guarantee of safety can be made when designing a thruster, as economic considerations must be taken into account. For this purpose, work is being done to reduce the level of energy loss, material consumption and labor intensity during repair work. Since all the useful power flow of the locomotive passes through the draft gear, the transmission has a high f.i.e. should be Constructive and technological solutions are considered suitable for ensuring a high level of

normalization and unification, repairability and control of parts and assemblies. An important consequence of the above for designers is the tendency to reduce the number of energy flow transformations, which are always associated with energy loss, and also, if possible, to abandon surface-friction dynamic connections that require periodic lubrication of transmission mechanisms. their surfaces. Reduction of labor, energy and material consumption is also required at the production stage of transmission. Sometimes they may conflict with operational requirements, and in such cases operational requirements prevail, as the overall technical and economic efficiency of the locomotive is determined by the duration of the operational cycle.

Determination of dynamic problems. As with any mechanical system, rolling stock is affected by a number of exciting factors. Conventionally, they can be divided into two parts: external and internal. External factors are those whose nature does not depend on the characteristics of the towing vehicle, and internal factors are those whose occurrence is determined directly by the characteristics of the towing vehicle. In addition, force, kinematic and parametric excitations are also distinguished. External force excitations occur when the resistance to the movement of the train (locomotive) changes. Kinematic excitations are determined by the non-linearity of the track in the profile caused by the collapses and bulges of the rail profiles, as well as local defects of the top layer of the track. Parametric factors are related to the uneven distribution of its dissipative, inertial and elastic properties along the length of the road.

Internal force excitations are generated by the electromagnetic torque of traction motors and the imbalance of rotating parts. Due to the non-ideal roundness and inclination of the rolling surface of the wheel due to the geometric axis of the wheel pairs, as well as internal kinematic excitations as a result of the kinematic errors of the gear coupling and the traction coupling, the radial stiffness of the coupling at the given coordinate (the inclination of the elastic elements in the environment changes during rotation), as well as the conditions of the coupling in the contact of the wheel with the rail parametric excitations arise as a result of its change.

By means of cushions placed inside the bushings of the traction transmission, the traction and braking forces of the vehicle are protected, at the same time from static and dynamic effects, etc. It plays an important role in maintaining the functionality of the mechanical system by receiving the generated forces and transferring them to the trolley and the wheel pair accordingly. Thus, the bushings should maximize the degree of reliability by maintaining long-term working ability under the interaction of both static forces and dynamic forces of different directions. In order to obtain maximum reliability, each force affecting the transmission through the buck joint should be calculated by progressive methods, critical limits should be determined, systematic probability calculation should be developed for the design of new structures, mathematical optimization models and automation should be used to find the optimal ratios between the main elements. it is possible to balance the forces, prevent uneven loading, and eliminate vibrations and wear by building a raised layer algorithm.

In the scheme below, the system of forces affecting the thrust transmission is shown schematically (Fig 4).

The mentioned factors usually occur at the same time during train movement. However, each of the mentioned factors manifests itself in different ways, since both the draft vehicle and the draft transmission represent a dynamic system with many degrees of freedom. Each of them causes a forced oscillation of the dynamic system depending on the ratio of the specific oscillation frequency of the system and the frequency of the acting excitation effects, the amplitude of the effect and the dissipative properties of the system.

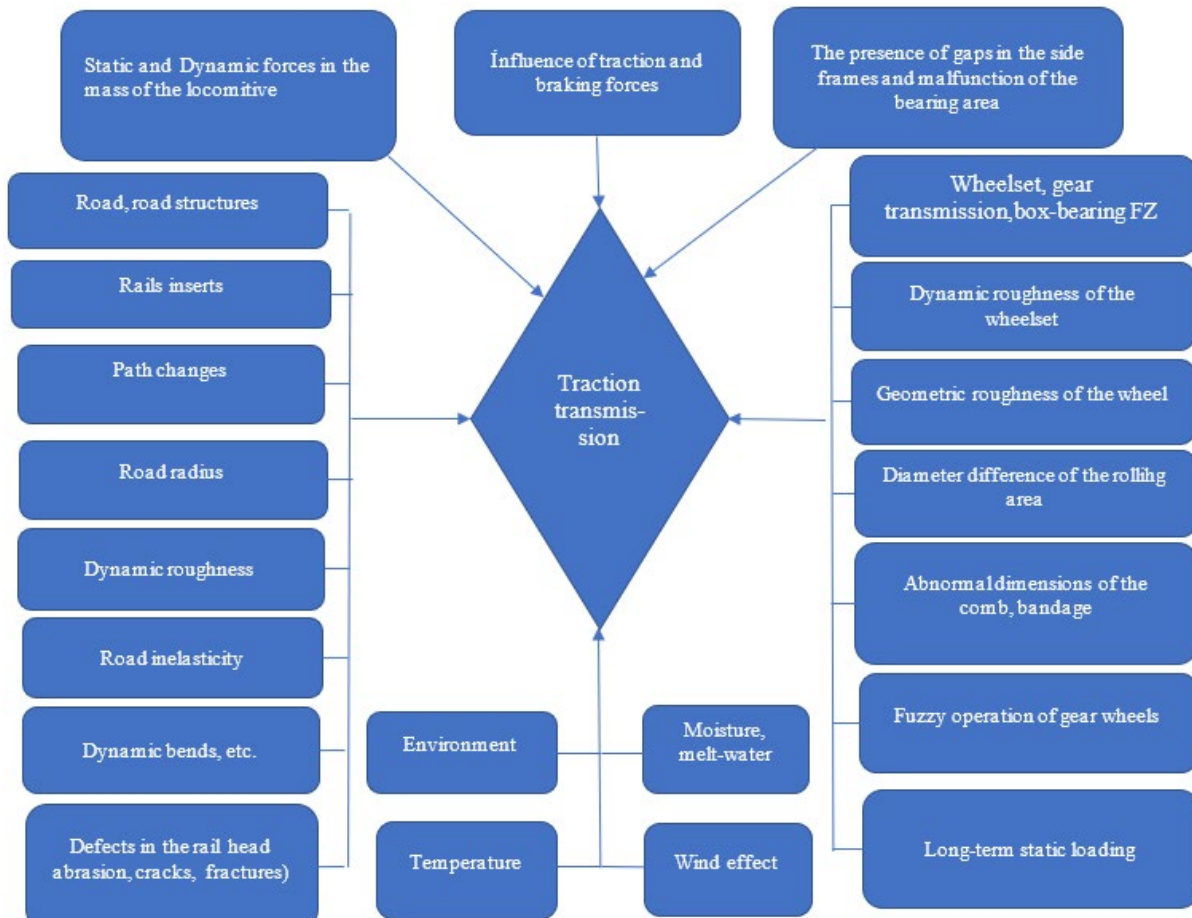


Figure 4. Static, dynamic and aerodynamic loading scheme of the cushion

The dynamic processes that form abnormal effects on the traction transmission of the train are shown in the following oscillogram (Fig 5.). The most dangerous defects according to the severity of the result detected by the "Pioneer Integral" infrastructural diagnostics complex during the diagnostics of the geometrical parameters of the track, the results of Deviation from the plan a), Level b), Distance between two rails c) and Track lying right/left d) given in the table (table 1).

Table 1. Diagnostic results of railway geometrical parameters

Defect	Deviation, mm	Level difference, mm	Distance between two rails, mm	Road collapse, mm
The situation				
size norm	9	5	1520 (+8), (-4)	9
fact	84	24	1511	21

External dynamic influences usually manifest themselves in two ways:

1. Quickly effective. In this case, a sharp deviation of defects from the norm, several of them are the same

its timely appearance results in the derailment of vehicles, which leads to failure and damage to parts of traction drives.

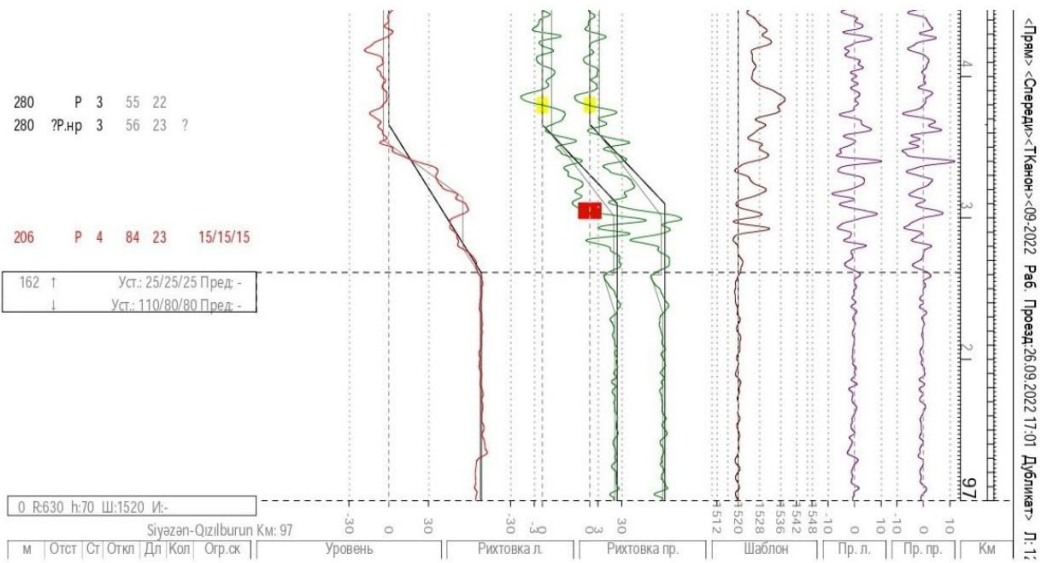
2. Late effective. At this time, the defects differ little from the norm, practically from the movement of trains

does not prohibit, its effects can be reduced to a certain extent by limiting the speed. But if it continues for a long time, it causes premature wear, cracking, and fatigue of the transmission parts, thereby reducing the service life.

Ilham HUSEYNOV

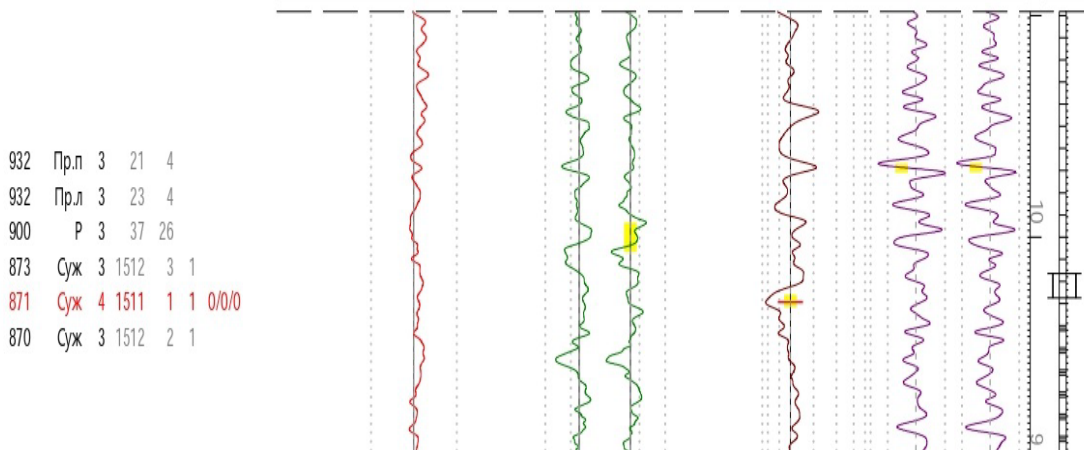
Analysis of taction transmission of railway vehicles and their dynamic characteristics

Biləcəri - Yalama (55101) Путь:1 Км:97 ПЧ - 1/ПЧУ - 1/ПД - 9/ПДБ - 1 Уст: 110/80/80 Пред: -/-/
Кол.ст.- 2:79; 3:2; 4:1. Кол.орг.:1/0 Орг.:15/15/15 Скор:23 КрдПЧ

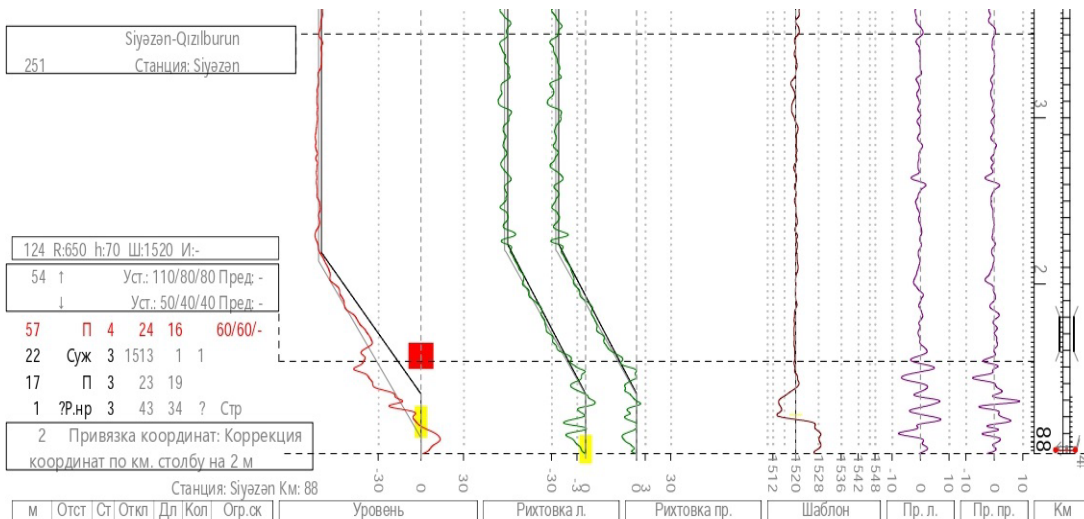


a)

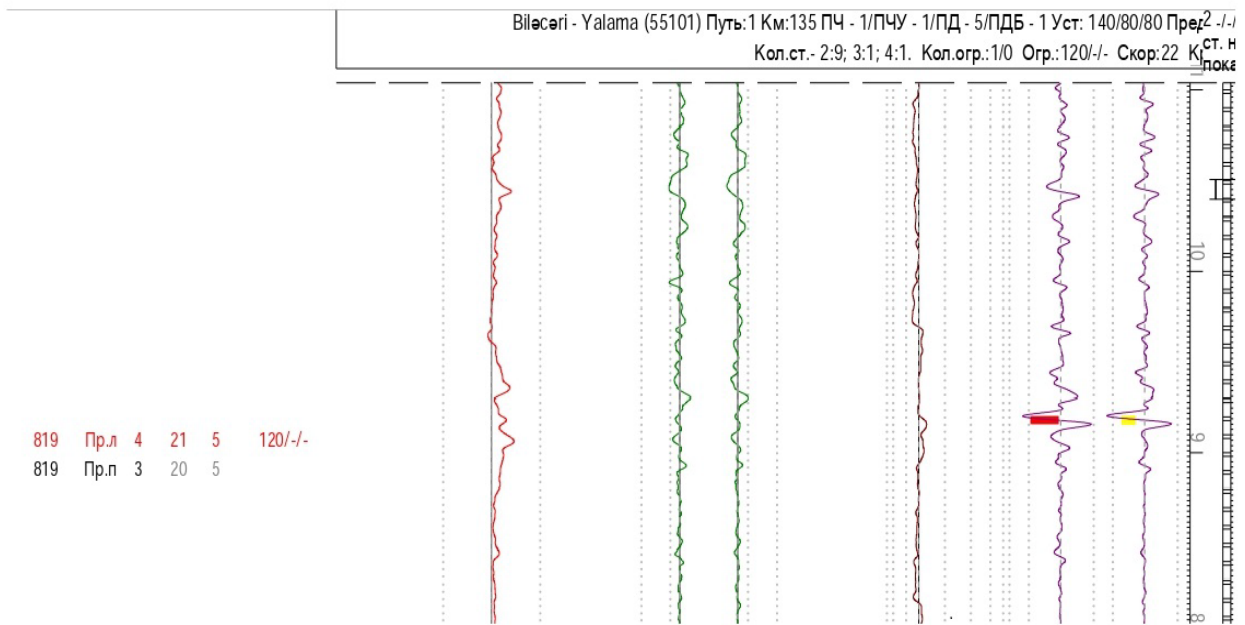
Ələt Baş - Horadiz (55107) Путь:2 Км:123 ПЧ - 8/ПЧУ - 1/ПД - 1/ПДБ - 1 Уст: 80/60/60 Пред: 2/1/1
ст. не показ. Кол.ст.- 2:30; 3:5; 4:1. Кол.орг.:1/0 Орг.:0/0/0 Скор:33 КрдПЧ



b)



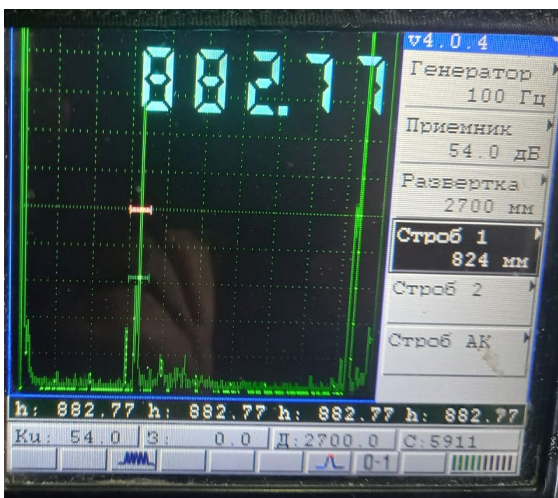
c)



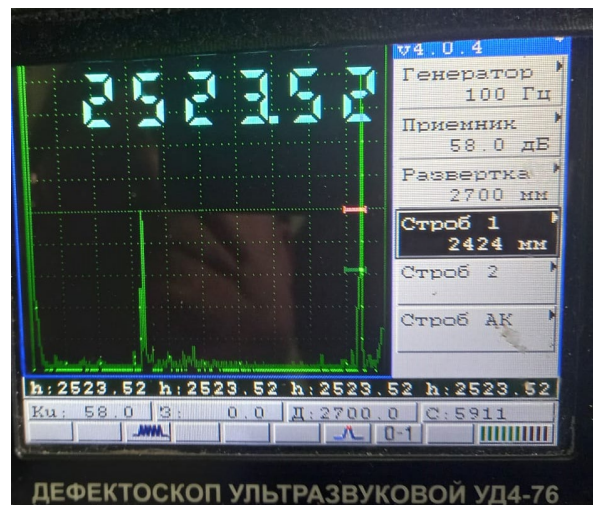
d)

Figure 5. Diagnostic results of checking the geometric parameters of the track by the "Pioneer Integral" infrastructural diagnostics complex.

Results and discussion. Dynamic processes caused by intrinsic and extrinsic defects may dominate for a number of transmission elements. Among these processes, the most dangerous due to the degree of severity of the consequences are defects in the wheel pair shaft. Failure to detect these defects in time results in the breakage of the wheel pair shaft, which leads to the failure of the vehicle. On the other hand, such dangerous situations can result in accidents and serious accidents. In order to detect these defects in time, ultrasonic inspection of the shafts is carried out with the UD4-76 defectoscopic device. The device determines the presence of any defects in the shaft and its level of serviceability. Figure 6 shows the defectoscopy results of serviceable (a) and unserviceable (b) wheelset shafts of the electric train. Defects (cracks) in the wheel pair shaft or motor shaft, vibration of the reducer body, kinematic errors of gear coupling, asymmetry of load distribution, critical moment of inertia of rotating parts, errors in the braking system and. s is determined by factors.



a)



b)

Figure 6. Defectoscopy of the wheel pair shaft of the electric train

Brake systems are one of the most important components that depend on the technical condition of traffic safety [13]. Currently, pneumatic automatic brakes are the most widely used in railway vehicles. The main power unit of brakes, which converts the kinetic energy of compressed air into mechanical work, is the brake cylinder. Currently, industrial enterprises produce a large number of brake cylinders due to their constructional characteristics. The analysis of their constructions allowed us to conclude that one of the main disadvantages is the impossibility of compensating the angular inclinations of the rod at the maximum output from the housing (Fig. 7).

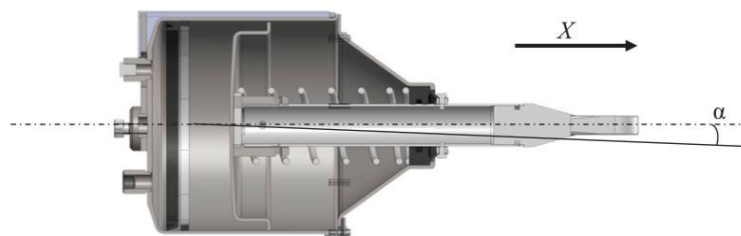


Figure 7. View of the angular inclination of the brake cylinder

This contributes to bending of the rod, disruption of the operation of the brake cylinder and, accordingly, poses a potential threat to the safety of the train. The angular inclination of the brake cylinder rod disrupts the functionality of the mechanical system and creates unpleasant errors. Thus, during pneumatic braking, the movement of the rod at a certain distance from the cylinder activates a series of interconnected mechanisms, and finally, the brake pads are pressed against the wheel, which is the actuator of the connecting rod actuator. At this time, the errors of the angular inclinations when the rod exits the cylinder are observed with various defects in the pressing of the brake mold carried by the sequentially controlled mechanisms to the wheel. These defects serve to reduce reliability by increasing the intensity of rejections in transmission drive wheels, traction reducers, traction motors, etc. This suggests that when analyzing the dynamic characteristics of traction drives, the braking system of the train should be considered as an influencing factor, and research should be carried out to improve the brake cylinders as one of the most important ones. issues of increasing the efficiency of brakes. In this direction, our article No. conducted extensive research and presented the results.

In order to determine the dynamic loads and the nature of their changes, it is necessary to know the working mode of the transmission, the excitations corresponding to them, to have a mechanical-mathematical model of the impulse transmission and to know its research methods.

In order to study the dynamic effects on draft transmissions in more detail, it is necessary to find the optimal methods of elimination, taking into account the defects, their nature and their manifestation characteristics. Defects in the transfer of darts have been found to be sporadic and subject to regularity [13, 14]. This indicates that the causes of the same defects are the same or similar. It is proposed to develop a generalized mathematical model, taking into account all the components that can have a negative effect on the mechanical system, and determining their causes and malfunctions based on statistical indicators. traction transmission, simplify repair processes and facilitate the identification of defects.

From the analysis of the dynamic characteristics of traction transmissions, it can be seen that the mechanical system has very complex, multi-state and very efficient working conditions. Therefore, the system should be studied in detail, taking into account the situation, influence and transition parameters from one state to another, and innovative solutions should be developed based on the principles of optimality. For this purpose, it is possible to eliminate the effects of the dynamic defects mentioned above, it meets the minimum mass and size conditions by ensuring the minimum value of the center distance, and ensures the shortening and equality of the force arm. its distribution between supports simplifies repair processes, reduces cost, and also reduces the number of structural elements. an innovative three-speed reduction gearbox is proposed, which increases reliability and reduces the mass of rotating parts due to double sliding pads, saves electricity by increasing the useful

work coefficient, thereby improving the technical level of railway vehicles [16]. The proposed transfer has been approved at the Eurasian patent level for scientific innovation and merit. In the following articles, research works on the structural characteristics of the transmission, advantages, parameters of adaptation to railway vehicles and other indicators will be given.

Conclusions.

1. Conducting experimental studies on traction transmission and its working conditions the main influencing factors are identified and their oscillograms are given.

2. Causes of factors that negatively affect the dynamic characteristics of traction transmission defects can be found by means of a defectoscopy device and the results are given.

3. On two shafts, which provides the superiority of the technical level of the mechanical system It is proposed to carry out theoretical and simulation studies in order to check the suitability of the transmission with an innovative drag reducer symmetrically placed according to the supports, consisting of a three-stage cylindrical gear transmission [16].

REFERENCES

- [1]. Huseynov, I.D., Abdullaeva, M.R. *The role and tasks of railway transport in the sustainable development of the country*. “The role of azerbaijan's transit potential in economic development” Conference, Sumgayit, October 22-23, 2020, Volume 6, 330-332. Link: <https://www.elibrary.ru/item.asp?id=45636980>
- [2]. Elyazov, I.Sh., Huseynov, I.D. *Determination of technical features of the new generation electric carriers of the Azerbaijani railway*. Collection of scientific works of UkrDUZT, Kharkiv issue 198, 2021, pp. 151-158.
- [3]. Biryukov, I.V., Belyayev, A.I., Ribnikov, E.K. *Traction transmissions of electric rolling stock of railways*. Transport, 1986, p. 256.
- [4]. Khalilov, I.A. *Investigation of the influence of clearance in couplings on the dynamic properties of machine drives*. Russian Engineering Research, 2010, № 3, pp. 10-13.
- [5]. Khalilov, I.A. *Investigation of the dynamic properties of machine drives, taking into account the damping and design features of the couplings*. Russian Engineering Research, 2013, № 4, pp. 22-25.
- [6]. Khalilov, I.A. *Investigation of temperature change of elastic elements of couplings as a result of damping*. Russian Engineering Research, 2012, № 4, pp. 26-29
- [7]. Xiaohong, H., Qinyu, L., Qunzhan, Li, Sida T., Ke Sun. *Power management in co-phase traction power supply system with super capacitor energy storage for electrified railways*. Railway Engineering Science, 2020, №28 (1), pp. 85–96.
- [8]. Esteban, B., Maksym, S., Edwin, V., Qing, W., Yan S. and others. *Prediction of rail surface damage in locomotive traction operations using laboratory-field measured and calibrated data*. Engineering Failure Analysis, Volume 135, May 2022.
- [9]. Sheng Liu, Ye Tian, W.J.T. (Bill) Daniel, Paul A. M. *Modelling of track wear damage due to changes in friction conditions: A comparison between AC and DC electric drive locomotives*. Wear, Volumes 366–367, 2016, pp. 338-345.
- [10]. <https://www.tsa.at/products/traction-drives/>
- [11]. Sergii, P., Glib, V., Alyona, L., Vasyi, R., Elyazov, I.Sh., Huseynov, I.D. *Influence of structural solutions of an improved brake cylinder of a freight car of railway transport on its load in operation*. Eureka: Physics and engineering, 2022, Volume 6 (43), pp. 45-55.
- [12]. Elyazov, I.Sh., Guseynov, I.D., Gasratova, L.M. *Determination of defects in wagon parts using mathematical methods*. AzTU Proceedings, 2018 №3, pp.45-46.
- [13]. Ahmadov, H.M. *Effect of defects in wheels and rails during operation on dynamic characteristics of trains*. Baku, 2005. 146 p.

- [14]. Abdullaev, A. I. Rasulov, G.R., Huseynov, I.D. *Innovative reducer for railroad switch drives and evaluation friction work on double sliding bearings*. SOCAR Proceeding, 2022, Special Issue No. 1, pp. 001-006.
- [15]. Abdullaev, A.I., Najafov, A.M., Huseynov I.D., Celebi I.G., Rasulov G.N., Adgezalova S.A. *Traction drive of rolling stock*, Eurasian Patent Organization (EAPO), 2023, patent № 4043160.
- [16]. Abdullaev, A., Huseynov, I., Elyazov, I., Abdullaev, R. *The technical assessment of the level of innovative traction transmission of railway vehicle*. EUREKA: Physics and Engineering, 2023, 3, pp. 40–51.

Received: 06.11.2022

Accepted: 15.02.2023



SUBMISSION GUIDELINES

General requirements.

Article should not be earlier published in any edition, stated in the short form and edited. The scientific article maintenance should correspond to one of the following scientific directions: Designing of machines; Materials technology; Mechanics; Manufacturing engineering; Economy and management; Automatics and ICT; Technical information.

The documents applied to article.

The conclusion of the corresponding organization (chair, etc.); The expert opinion on expediency of the publication of the article; The covering letter; The Information on the authors (name, patronymic, surname, the exact address, place of work and position, scientific degree, area of scientific activity, contact phones, e-mail address, etc.).

Preparation rules.

Format - A4; *Margins from each party* - 20 mm; *Program* - Microsoft Office Word; *Font* - Times New Roman, a font size - 12, an interval - 1.

The scientific article can be written only in English language, and it is represented in duplicate.

Article volume - 5 ... 8 pages.

Sequence of compilation:

1. Article name - on the center;
2. Names and surnames of the authors - on the center;
3. Full addresses of a place of work of authors - on the center;
4. Co-ordinates of authors: e-mail address, phone numbers.
5. The abstract: not less than two-three offers, and no more than 100 words. In the summary: article summary, problem statement, and the information on the received results should be reflected.
6. Keywords: often used 3 ÷ 5 terms under the article.
7. The basic text.
8. The references.

The main text of article should be divided as follows:

For example: "*Introduction*", "*Problem statement*", "*Decision or test methods*", "*Results of the decision or tests and their estimation*".

In introduction: the description of the problem statement, the work purpose and etc.;

In the main part: formation of problem statements; research and methods of the decision, their advantage and difference from existing methods; examples confirming efficiency of the offered method of the decision and the results received.

In the conclusion: evaluation of the results.

Drawings. *Formats* - DOC, JPEG, TIFF and PDF (600 dpi). *The size* – min. 5 × 5, max. 10 × 15. *Arrangement* - ("In the text", in the center). Images of drawings should be accurately visible, and all symbols well are read.

Drawings, paintings, schedules and algorithms should correspond to standard requirements.

Tables are located in the text and are numbered, and the name of each table should be specified in the right top corner.

Formulas should be written down in format *Equation* in the separate line. It is not recommended to use special symbols in the text written on the same line in format *Equation*. Formulas should be written down in certain sequence and are numbered on the right.

The references should correspond to the text and sequence of article. It is recommended to refer to sources published in last 10 years.

The additional information. Edition has the right to spend necessary updating and reductions. Authors bear a scientific article maintenance responsibility. To the publication those articles which have received a positive response are represented only. If article is not published, the edition decision is possible to data of authors, the manuscript and disks do not come back.

MACHINE SCIENCE № 1, 2023

Editorial address:

AZ1073, Azerbaijan, Baku, H.Javid av., 25.
Telephone: (+994 12) 538 94 12

E-mail: msj@aztu.edu.az

Web site: <http://msj.aztu.edu.az/>

Format: 60×84 1/8.

Number of copies printed: 100.

Publisher: AzTU Publisher

